Title	Development of radar polarimetry techniques for forest biomass retrieval and disturbance detection
Author(s)	Rajat
Degree Grantor	北海道大学
Degree Name	博士(環境科学)
Dissertation Number	甲第16215号
Issue Date	2025-03-25
DOI	https://doi.org/10.14943/doctoral.k16215
Doc URL	https://hdl.handle.net/2115/95062
Type	doctoral thesis
File Information	RAJAT.pdf

Development of radar polarimetry techniques for forest biomass retrieval and disturbance detection

森林バイオマス推定と撹乱検知のためのレーダーポラリメトリ技術の開発

Ph.D. Thesis Submitted by

Rajat
（ラジャット）

Ph.D. Supervisor

Assoc. Prof. Ram Avtar

Division of Environmental Science Development,
Graduate School of Environmental Science,
Hokkaido University, Sapporo, Japan

March 2025

Development of radar polarimetry techniques for forest biomass retrieval and disturbance detection

森林バイオマス推定と撹乱検知のためのレーダーポラリメトリ技術の開発

by

Rajat
M.Tech. degree in Remote Sensing, Birla Institute of Technology, Mesra, India

APPROVED BY SUPERVISORY COMMITTEE:

Chairperson:	Associate Professor Ram AVTAR
Member:	Professor Shiro TSUZAKI
Member:	Professor Teiji WATANABE
Member:	Professor Junjiro Negishi
Member:	Associate Professor Mamoru Ishikawa

March - 2025

Development of radar polarimetry techniques for forest biomass retrieval and disturbance detection

森林バイオマス推定と撹乱検知のためのレーダーポラリメトリ技術の開発

by

Rajat

A dissertation submitted in partial fulfillment
of the requirement for the degree of

DOCTOR OF PHILOSOPHY

in

Graduate School of Environmental Science

of the

Hokkaido University

March - 2025

Abstract

Forests occupy approximately 31% of Earth's land surface and provide a wide range of essential ecosystem services. They play crucial roles in regulating climate, supporting nutrient cycling, hosting diverse flora and fauna, and providing aesthetic and cultural benefits. However, the unsustainable exploitation of natural resources driven by anthropogenic demand has led to the conversion of millions of hectares of forestland into other land-use categories. In addition to deforestation, the quality of the remaining forest cover has been compromised by degradation driven by factors such as overgrazing, logging, and pollution. Deforestation and forest degradation account for approximately 17% of global carbon emissions, underscoring the critical need for effective mitigation strategies. In response, various international initiatives have been established to promote the conservation and sustainable management of forest resources. One such initiative is the Reducing Emissions from Deforestation and Forest Degradation (REDD+) program launched by the United Nations Framework Convention on Climate Change. This program encourages the development of robust methodologies for monitoring, reporting, and verifying forest cover and carbon stocks, as well as the establishment of reference levels for tracking changes over time. The availability of open-access remote sensing data from instruments such as the Moderate Resolution Imaging Spectroradiometer, Landsat, and Sentinel has facilitated the creation of operational products for the monitoring of deforestation. However, existing monitoring systems often struggle to detect small areas of forest disturbance and rely heavily on cloud-free imagery. Forest degradation assessment remains a significant challenge due to the dynamic and complex nature of forest ecosystems. Synthetic aperture radar (SAR) has emerged as a complementary tool for forest monitoring to address the limitations of optical sensors. The ability of SAR to penetrate cloud cover and its sensitivity to the structural, geometric, and dielectric properties of vegetation enable tracking of forest changes under varying environmental conditions.

This work introduces an L-band fully polarimetric SAR (PolSAR) algorithm for forest biomass retrieval using seven-component scattering power decomposition (7SD) and random forest regression (RFR) for forest above-ground biomass (AGB) estimation. As part of this research, L-band PolSAR data were used to develop a model for forest biomass estimation. Biomass was estimated using the fully polarimetric ALOS-2/PALSAR-2 datasets and field measurements of AGB. Using the 7SD model, seven scattering powers were extracted from

ALOS-2/PALSAR-2 data for AGB estimation. Field data were used to validate the biomass estimates obtained from this model. AGB estimated at the Shivamogga forest site using the model was consistent with field measurements. The root mean squared error (RMSE) and relative RMSE with respect to mean AGB were 21.94 Mg/ha and 19.46%, respectively, which are within acceptable ranges. The model was applied to the Tundi forest area for cross-validation, where relative RMSE with respect to mean AGB was 22.9%. A novel approach for estimation AGB in tropical forests has been proposed using scattering powers generated from L-band fully polarimetric data.

To further improve the accuracy of biomass estimation using SAR data, this study explored the potential use of multi-frequency SAR data from ALOS-2/PALSAR-2 (L-band) and RADARSAT-2 (C-band) with canopy height from the Global Ecosystem Dynamics Investigation (GEDI) to enhance the accuracy of AGB estimates for tropical forests. The integration of L- and C-band SAR data improved the precision of biomass estimates by leveraging the complementary characteristics of each frequency. This research focused on the Shivamogga forest, employing full PolSAR data from both L- and C-band sensors alongside canopy height data from GEDI. A random forest algorithm was used for biomass estimation that incorporated scattering powers derived from 7SD and forest height measurements from GEDI as input variables. Model performance was validated against field measurements, yielding RMSE of 16.06 Mg/ha and relative RMSE of 14.24%, which indicate improved estimation accuracy. These findings demonstrate the value of integrating scattering power and canopy height information for AGB estimation. The synergy between structural information from SAR scattering and vertical insights obtained from forest height data supports more comprehensive and reliable biomass assessment.

Full PolSAR data has limitations in temporal resolution and spatial coverage. To extend the scattering power decomposition to dual-PolSAR data, this study introduces a novel four-component scattering power decomposition (DP-4SD) method for dual-PolSAR data. The increasing availability of dual-PolSAR data has led to a significant increase in its application in recent decades. Model-based decomposition in combination with polarimetric information extraction from PolSAR data can play a crucial role in target identification and classification. In this context, a covariance matrix [C] composed of four independent parameters was used as the input for dual- polarimetric DP-4SD. A novel 4SD model was tested using dual-PolSAR data from space-borne ALOS-2/PALSAR-2, and its performance was evaluated against existing scattering power decomposition methods. The performance of the proposed 4SD model was assessed using dual-polarization data from the Haldwani forest area and San Francisco to evaluate its classification capabilities within a single class (forest) and across various land-use and land-cover classes in San Francisco. Overall classification accuracy of 85.69% for Haldwani and 93.66% for San Francisco was achieved, with fewer unclassified samples compared to the existing model. The 4SD model demonstrated superior classification accuracy and improved the interpretation of polarimetric information, indicating its potential to significantly improve land-use and land-cover mapping based on dual-PolSAR data.

This research work further extended the 4SD-DP to forest monitoring by developing a novel Forest Disturbance Index (FDI). FDI was validated against observed biomass changes in highly disturbed forest areas to ensure reliability. The validation results demonstrated RMSE of 21.844 Mg/ha and relative RMSE of 21.84%, indicating efficacy of the model in capturing biomass dynamics in areas undergoing significant forest disturbance. These results underscore the potential of FDI as a tool for monitoring forest health and tracking degradation trends in vulnerable regions.

The concluding chapter synthesizes the key findings of this work, emphasizing their practical implications for forest management, conservation policies, and environmental monitoring. These results offer valuable insights for addressing deforestation, forest degradation, and land encroachment, which are critical ecological issues in many countries. Furthermore, this study highlights the importance of leveraging remote sensing technologies for sustainable forest management and climate change mitigation.

Acknowledgments

I would like to express my deepest and sincere gratitude to my supervisor, **Dr. Ram Avtar**, from the Environmental Earth Science Department at Hokkaido University for his unwavering support and invaluable guidance throughout my Ph.D. journey. His patience, selflessness, and profound expertise have been instrumental in helping me navigate the challenges encountered over the past three years. Dr. Avtar has been a constant source of inspiration, encouragement, and knowledge, always available to address any difficulties I have faced, whether related to experimental work or conceptual understanding. Importantly, he nurtures his students' scientific instincts, offering not only precise guidance, but also the freedom to explore new ideas independently. His mentorship has shaped me into a more competent researcher. Moreover, by observing his exemplary work ethic and time management, I have gained essential insights that will undoubtedly serve me well in my future career, both as a dedicated professional and thoughtful individual.

I am profoundly grateful to my family for their unwavering beliefs in me and for their patience and understanding throughout this journey. Despite being far from them, their constant support provided me with immense joy, strength, and motivation. I am especially indebted to my father, **Mr. Rajendra Singh**, and my mother, **Mrs. Usha Devi**, for encouraging me to aim high and guide me to live a life grounded in morality and discipline. I am also deeply thankful to my friends and lab mates for their invaluable time and their insightful feedback. Their contribution has been an essential part of my academic journey. I extend my gratitude to **Dr. Ram Avtar's laboratory**, the Graduate School of Environmental Science, and the administrative staff of Hokkaido University for their support and assistance throughout my studies. Their cooperation and kindness have made my research experience smooth and complete.

Finally, I sincerely thank the DX Doctoral fellowship (JPMJSP2119) for the financial support provided over the past three years, which was crucial for the successful completion of my research.

Rajat

Table of Contents

List of Figures

List of Tables

List of Symbols

A Amplitude

t Instant of time

r Position vector

R or r Range distance to target

$\mathbf{E}(\mathbf{r})$ Wave electric field

$\mathbf{E}(\mathbf{r}, \boldsymbol{t})$ Time vary ing electric field

$\mathbf{B}(\mathbf{r}, \boldsymbol{t})$ Magnetic induction

$\mathbf{H}(\mathbf{r}, \boldsymbol{t})$ Magnetic field

$\mathbf{D}(\mathbf{r}, \boldsymbol{t})$ Electric induction

$\mathbf{J}(\mathbf{r}, \boldsymbol{t})$ Conduction current density

$\boldsymbol{\rho}(\mathbf{r}, \boldsymbol{t})$ Volume density of free charges

ς Conductivity of propagation medium

$\mathbf{M}(\mathbf{r}, \boldsymbol{t})$ Magnetization vector

$\mathbf{P}(\mathbf{r}, \boldsymbol{t})$ Polarization vector

v Permeability of medium

e Permitivity of medium

ω_f Angular frequency

ζ Absolute phase term of electric field

k Wavenumber

θ Orientation angle about line of sight

k Wave vector

E^i Incident electric field

$\mathrm{E}\ ^x$ Scattered electric field

S Sinclair or Scattering matrix

HH Represent horizontal transmit and horizontal receive polarization

HV Represents horizontal transmit and vertical receive polarization

VH Represent vertical transmit and horizontal receive polarization

VV Represents vertical transmit and vertical receive polarization

τ Ellipticity

λ Wavelength

θ_0 Incidence or local incidence angle

k_p Pauli basis target vector

[T] 3×3 Coherency matrix

[C] 2×2 Covariance matrix

λ_i Unit orthogonal eigenvalue

P_s Surface scattering power

P_v Volume scattering power

P_d Dihedral or double bounce scattering power

P_h Helix scattering power

P_{od} Oriented dipole power

P_{cd} Compound dipole power

P_{md} Mixed dipole scattering power

P_g Ground scattering power

P_ε Helix scattering power

ϕ Interferometric phase

(...) Spatial or temporal ensemble average

List of Abbreviations

AGB Above Ground Biomass

ALOS Advanced Land Observing Satellite

BGB Below Ground Biomass

CBH Circumference at Breast Height

COP Conference of the Parties

CTD Coherent Target Decomposition

DBH Diameter at Breast Height

DEM Digital Elevation Model

DN Digital Number

DP Dual PolSAR

EM Electro Magnetic

FAO Food and Agriculture Organization

FCC False Colour Composite

FDD Freeman Durden Decomposition

GEDI Global Ecosystem Dynamics Investigation

G4U General Four-Component Scatering Power Decomposition With Unitary Transformation of Coberency Matrix

GHG Green House Gases

GPS Global Positioning System

GLAS Geoscience Laser Altimeter System

HDF Hierarchical Data Format

ISS International Space Station

IWCM Interferometric Water Cloud Model

JAXA Japan Aerospace Exploration Agency

JERS Japanese Earth Resources Satellite

JPL Jet Propulsion Laboratory

LAI Leaf Area Index

LiDAR Light Detection and Ranging

MIMICS Michigan Microwave Canopy Scattering Model

MRV	Measurement, Reporting and Verification
Mg/ha	Megagrams Per Hectare
NDVI	Normalized Difference Vegetation Index
NF	Non-Forest
NTFP	Non-Timber Forest Produce
PALSAR	Phased Array type L-band Synthetic Aperture Radar
PD	Penetration Depth
PDOP	Position Dilution of Precision
Pol-InSAR	Polarimetric SAR Interferometric
PolSAR	Polarimetric SAR
PWC	Plant Water Content
RADAR	Radar Radio Detection and Ranging
RCS	Radar Cross Section
REDD	Reduced Emission from Deforestation and Degradation
RFR	Random Forest Regression
RH	Relative Height
RMSE	Root mean squared error
RSR	Root to Shoot ratio
RTC	Radiometric Terrain Correction
RVoG	Random Volume Over Ground
SLC	Single Look Complex
SAR	Synthetic Aperture Radar
SIR-B	Shuttle Imaging Radar- B
SMC	Soil Moisture Content
SNR	Signal to Noise Ratio
SRTM	Shuttle Radar Topography Mission
SVR	Support Vector Regression
UNFCCC	United Nations Framework Convention on Climate Change
WCM	Water Cloud Model
4SD-DP	Four component scattering power decomposition for dual PolSAR
7SD	Seven component scattering power decomposition

Chapter 1 : Introduction

1.1 Background

Forests are among the most vital components of terrestrial ecosystems, covering approximately 30.6% of the Earth's land surface or just under 4 billion hectares (UNFCCC, 2015). Over the past 25 years, global forest area has decreased by 3.1%, and forest biomass has diminished by 11 gigatons (Gt), equating to an annual loss of approximately 443 million tons. The overall rate of forest area loss has slowed in the past decade, and the most substantial decline has been observed in tropical regions. Between 2010 and 2015, tropical forests were depleted by around 5 million hectares annually (UNFCCC, 2015). Given the ecological and environmental importance of these forests, monitoring their health and accurately mapping their extent is essential for effective conservation and resource management.

Forest biomass and carbon stocks are key indicators of a forest's health, as well as its productive capacity, energy potential, and ability to sequester carbon. Forest biomass is distributed in two primary components: above-ground biomass (AGB) and below-ground biomass (BGB), both of which are commonly measured in megagrams per hectare (Mg/ha) or tons per hectare. Additional indicators of forest health include stand height and forest structure, which provide secondary data on forest growth and biodiversity. Driven by successful conservation efforts, the annual rate of global deforestation has decreased from 16 million hectares between 1990 and 2015 to 10 million hectares between 2015 and 2020 (FAO, 2020). This shift underscores the effectiveness of conservation measures worldwide.

In response to the increasing emphasis on reducing carbon emissions associated with forest loss, the United Nations Framework Convention on Climate Change (UNFCCC) introduced the REDD+ (Reduced Emissions from Deforestation and Degradation) initiative (Sinha et al., 2015). REDD+ was designed to preserve biodiversity and simultaneously deliver multiple co-benefits through the provisioning of ecosystem services. As an incentive-based initiative, REDD+ requires the development of robust measurement, reporting, and verification (MRV) systems to track carbon emissions from forests(Gibbs et al., 2007a; Goetz et al., 2015). These MRV systems are benchmarked against reference levels (RLs) to provide a basis for comparison. The development of scientific methods to accurately estimate carbon emissions and sequestration, along with the definition of RLs at both small and large scales, have become urgent research priorities. Consequently, comprehensive assessment of forest biophysical parameters, especially biomass, is crucial for quantifying the impacts of deforestation and afforestation as well as to monitor forest health.

However, significant uncertainties in biomass estimation persist due to the diversity of forest types, which vary greatly in terms of structure and ecological functions. This variability contributes to challenges in accurately assessing forest biomass at both the local and global scales. Forest degradation and deforestation together account for 17% of global greenhouse gas emissions and also cause biodiversity loss and the degradation of ecosystem services (FAO, 2016). Traditionally, forest monitoring has relied on statistical methods employed by national and international organizations. Although such methods yield accurate data at the local scale, they often introduce high levels of uncertainty when extrapolated to regional or global domains. Tropical forests, which hold the largest pool of above-ground carbon, present the greatest challenge for field surveys due to inaccessibility and are thus understudied. Ground-based forest inventory data are typically limited to small regions, introducing potential biases into global biomass assessments (Peregon & Yamagata, 2013; Sassan Saatchi, 2019). Remote sensing technology has emerged as a pivotal tool for monitoring environmental changes, including forest cover and bio-geophysical parameters (Beaudoin et al., 1994; Ji et al., 2024; Lausch et al., 2017; Rignot et al., 1997; Soja et al., 2013; Treuhaft et al., 2015; Treuhaft et al., 1996; Yadav et al., 2021). The integration of satellite-based remote sensing data with ground-based inventory data has enabled biomass and carbon stocks to be measured with greater precision and lower cost. This technology is gradually replacing traditional forest monitoring methods (Patenaude et al., 2005; Sinha et al., 2015). The implementation of open data policies has facilitated access to various remote sensing datasets, including multi-spectral, synthetic aperture radar (SAR), and light detection and ranging (LiDAR) data, which are now available to a wide range of users.

The availability of the Landsat data series, beginning in 1972 for selected areas and expanding to the global scale in1999, enabled the production of the first global map of intact forest (Potapov et al., 2008). This foundational map was developed into a comprehensive operational forest cover monitoring system (Hansen et al., 2013). While this system is highly effective at detecting deforestation, it remains less sensitive to forest degradation, particularly disturbance caused by selective logging, fuelwood collection, lopping, and other human activities. Furthermore, optical remote sensing, which is commonly used for forest monitoring, is limited in its ability to penetrate the upper canopy layers and is affected by weather conditions (Santi et al., 2017). These limitations are particularly problematic in tropical regions with persistent cloud cover.

SAR offers distinct advantages for forest monitoring. SAR is an active microwave imaging technique that transmits electromagnetic (EM) waves and measures backscattered signals from the surface of the Earth. Compared to real-aperture radar, SAR achieves higher resolution through exploitation of Doppler shifts in the returned signals (Boerner et al., 1992). SAR's ability to penetrate clouds and vegetation layers makes it particularly suitable for monitoring forests in tropical regions. In addition, SAR data are sensitive to the structure, geometry, and dielectric properties of the forest canopy, further enhancing their utility for biomass retrieval and forest change detection. SAR remote sensing has been widely applied across diverse fields, including forestry, agriculture, hydrology, geology, elevation mapping, oceanography, and disaster monitoring (Henderson, 1998; Lavalle & Khun, 2014; Le Toan et al., 1992, 2011). Moreover, the combination of complementary remote sensing techniques has led to significant improvements in forest biomass estimation, particularly the integration of SAR and LiDAR data. LiDAR provides precise measurements of forest stand height, which are critical for the allometric models used to estimate biomass (Lefsky, Cohen, Harding, et al., 2002). Combining LiDAR height data with SAR structural information improves the accuracy of biomass estimation models. However, the limited availability of space-borne LiDAR data has constrained its use for global biomass estimation. Recently launched space-borne LiDAR missions, which cover billions of footprints across forests worldwide, have opened new opportunities for mapping forest changes, stand height, and biomass.

SAR systems can transmit and receive EM waves in multiple polarization combinations, including HH (horizontal–horizontal), HV (horizontal–vertical), VH (vertical–horizontal), and VV (vertical–vertical). These polarization combinations provide valuable information about forest canopy structure and scattering mechanisms. Polarimetric SAR (PolSAR) decomposition techniques (Cloude & Pottier, 1996; Freeman & Durden, 1998a; Yamaguchi et al., 2005, 2011) allow researchers to break down complex scattering signals into their basic components, facilitating target detection, classification, and segmentation in forest environments. In forestry, PolSAR techniques can be effectively applied for the detection of forest degradation, deforestation, and phenological changes such as leaf fall (Shugart et al., 2010). The sensitivity of cross-polarized backscatter (HV) to forest disturbance has been demonstrated in several studies (Joshi et al., 2015), while co-polarized backscatter (HH) shows sensitivity to forest regrowth (Sun et al., 2002). However, recent research suggests that changes in backscatter do not always correlate directly with forest characteristics, underscoring the complexity of SAR backscatter interpretation. The capacity of PolSAR to distinguish among different target properties and scattering mechanisms offers significant advantages for forest monitoring, as it can support more detailed assessment of forest change dynamics.

Despite these advantages, the use of PolSAR data for forest disturbance and growth mapping remains limited, particularly in natural forests with diverse species compositions and complex structural characteristics. Most previous studies have focused on managed forests with homogeneous species compositions (Kobayashi et al., 2012, 2015; Watanabe et al., 2018). This research explores the potential of PolSAR data for mapping forest disturbance and regrowth, as well as the integration of SAR and LiDAR data for retrieval of AGB. The scattering behavior of natural forests, which often exhibit wide variations in species composition and forest structure, has not been thoroughly investigated. Elucidating this behavior is crucial to develop models capable of accurate monitoring and measurement in natural forests. This thesis addresses these research gaps through the development of a novel forest biomass estimation method for mapping forest dynamics, with a focus on forests in India. Using advanced PolSAR and LiDAR techniques, this study aimed to provide new insights into forest monitoring and biomass estimation.

1.2 Objectives

The main objective of this thesis is to develop models for forest monitoring and for forest biomass estimation using multi-sensor remote sensing data.

The key objectives of this research are as follows:

- **Forest AGB retrieval based on the L-band PolSAR decomposition technique**

- ❖ **Forest AGB retrieval based on multi-sensor remote sensing techniques**
- ❖ **Development of four-component scattering power decomposition (DP-4SD) for dual-PolSAR data**
- ❖ **Development of a Forest Disturbance Index (FDI) using dual-PolSAR data**

1.3 Outline of the Thesis

This Ph.D. research work leverages SAR and LiDAR technologies to address key gaps in forest disturbance monitoring and AGB retrieval. This work describes the development and application of novel remote-sensing techniques for effective forest management and monitoring. This thesis is divided into seven chapters, each systematically addressing specific aspects of research. The structure of the thesis is outlined below:

Chapter 1: Introduction

The introductory chapter sets the foundation for this research, outlining the background, objectives, and motivation for the study. This chapter emphasizes the ecological and environmental significance of forests, highlighting the challenges associated with monitoring forest disturbance and biomass. The chapter provides an overview of the roles of remote sensing technologies, such as SAR and LiDAR, in addressing these challenges. It also introduces the research questions, key objectives, and hypotheses of the study, followed by a brief outline of each chapter's contributions to the field of forest monitoring.

Chapter 2: Polarimetric Synthetic Aperture Radar

This chapter presents a comprehensive review of existing literature relevant to forest monitoring using remote sensing techniques. It begins with the fundamental principles of SAR remote sensing, focusing on radar polarimetry and decomposition techniques. The chapter explores how SAR polarimetric data can be used to distinguish between various scattering mechanisms.

Chapter 3: Forest Above-ground Biomass Retrieval Based on the PolSAR Decomposition Technique Using L-Band SAR Data

This chapter focuses on the development of a novel algorithm for estimating forest AGB based on 7SD technique and random forest regression machine learning by utilizing L band SAR data and field inventory data. It provides a detailed explanation of the PolSAR decomposition method employed in this study, which decomposes the backscattered signal into multiple scattering components. The performance of the algorithm is evaluated using validation datasets based on field measurements, and discussion of the accuracy, limitations, and improvements over existing approaches is included.

Chapter 4: Forest Biomass Estimation Using Multi-sensor Remote Sensing Data

This chapter explores the synergistic use of multi-frequency SAR data from ALOS-2/PALSAR-2 and LiDAR data from GEDI to improve the precision of forest biophysical parameter retrieval. This chapter integrates SAR and LiDAR datasets to address the limitations of single-sensor approaches, providing a more comprehensive understanding of forest biophysical parameters. By synergizing structural information from PolSAR data with height metrics from LiDAR, this multi-sensor approach improved the precision of biomass estimation, particularly in dense and heterogeneous forest landscapes.9

Chapter 5: Development of the Four-component Scattering Power Decomposition Model for Dual-polarization SAR Data

This chapter introduces a novel four-component scattering power decomposition model developed for dual-polarization SAR data. This newly developed model addresses the limitations of existing dual-pol decomposition techniques by providing improved sensitivity for complex forest structures, including mixed-species forests. Experimental results from multiple study sites were presented to validate the performance of the model, followed by a comparative analysis with conventional decomposition models.

Chapter 6: Development of the Forest Disturbance Index Using Dual-polarization SAR Data

This chapter illustrates the development and validation of the Forest Disturbance Index (FDI) using dual-polarization SAR data. FDI is designed to quantify forest disturbance through detection of subtle changes in forest structure caused by selective logging, forest fire and other human activities. FDI was validated through comparison with biomass change estimates in highly disturbed areas.

Chapter 7: Conclusion and Future Directions:

The final chapter highlights the key findings of this research and contributions to the fields of forest disturbance monitoring and biomass retrieval. This chapter provides a synthesis of the research outcomes and demonstrates how the models and methodologies developed here address the identified research gaps. This chapter describes the practical implications of this study for forest management, conservation efforts, and climate change mitigation. The limitations of this research are acknowledged, including data availability constraints and challenges in scaling the models to larger areas. The chapter concludes with recommendations for future research, including the potential integration of emerging technologies, such as machine learning and artificial intelligence, with SAR and LiDAR data. Suggestions for policy applications, such as enhancing REDD+ implementation and improving forest monitoring frameworks, are also provided.

Chapter 2 : Polarimetric Synthetic Aperture Radar

2.1 Introduction

This chapter presents a comprehensive review of the fundamental principles of synthetic aperture radar (SAR) remote sensing, and polarimetric SAR (PolSAR), providing essential background information about the methodologies employed in this research. Key concepts, such as SAR backscatter, polarization, and decomposition techniques, are discussed to establish a foundation for the subsequent sections.

2.2 Fundamentals of Electromagnetic Waves

Radar, an acronym for radio detection and ranging, is an active remote sensing technology that transmits electromagnetic (EM) signals and records reflected or backscattered signals from a target. The backscattered signal contains critical information about the target's scattering properties, such as its structure, geometry, and surface characteristics. Additionally, the time delay between the transmission and reception of the signal allows for precise calculation of the distance between the sensor and the target. This dual capability makes radar a powerful tool for remotely detecting objects and characterizing their properties.

Maxwell's equations (defined in 1873) govern the propagation of EM waves in a medium.

An EM wave at an instant of time t with its position given by the vector $\mathbf{r}$ can be defined as (J. Lee & Pottier, 2017):

$$\nabla \times \mathbf{E}(\mathbf{r},t) = -\frac{\delta}{\delta t}\mathbf{B}(\mathbf{r},t)\ \nabla \times \mathbf{H}(\mathbf{r},t) = \frac{\delta}{\delta t}\mathbf{D}(\mathbf{r},t) + \mathbf{J}(\mathbf{r},t) \tag{2.1}$$

$$\nabla \cdot \mathbf{D}(\mathbf{r},t) = \rho(\mathbf{r},t)\ \nabla \cdot \mathbf{B}(\mathbf{r},t) = 0 \tag{2.2}$$

Where, $\mathbf{E}(\mathbf{r},t), \mathbf{H}(\mathbf{r},t), \mathbf{D}(\mathbf{r},t)$ and $\mathbf{B}(\mathbf{r},t)$ represent the electric field, magnetic field, electric displacement field, and magnetic induction field, respectively (Henderson & Lewis, 1998). $\mathbf{J}(\mathbf{r},t)$ is the conduction current density, which is directly related to the electrical conductivity of the propagation medium through the relation $\mathbf{J}(\mathbf{r},t) = \varsigma\mathbf{E}(\mathbf{r},t)$. The volume density of free charges is expressed as $\rho(\mathbf{r}, t)$. The fundamental equations governing the relationships between these fields are as follows:

$$\mathbf{B} = v[\mathbf{H}(\mathbf{r}, t) + \mathbf{M}(\mathbf{r}, t)] \tag{2.3}$$

$$\mathbf{D} = \varepsilon\mathbf{E}(\mathbf{r}, t) + \mathbf{P}(\mathbf{r}, t) \tag{2.4}$$

where $\mathbf{M}(\mathbf{r}, t)$ and $\mathbf{P}(\mathbf{r}, t)$ represent the magnetization vector and polarization vector, respectively, and v and ε denote the permeability and permittivity of the medium.

For the specific case of a monochromatic wave of constant amplitude propagating through a medium free from mobile charges (i.e., without saturation or hysteresis effects), the following conditions apply:

$$\mathbf{M}(\mathbf{r}, t) = \mathbf{P}(\mathbf{r}, t) = 0.$$

In this scenario, the time-varying electric field vector $\mathbf{E}(\mathbf{r}, t)$ of the monochromatic plane wave, which has a constant complex amplitude $\mathbf{E}_0$ and a propagation direction defined by the wave vector $\mathbf{k}$, can be expressed as (J. Lee & Pottier, 2017):

$$\mathbf{E}(\mathbf{r}, t) = \mathrm{Re}\left[\mathbf{E}(r)e^{j\omega_f t}\right] = \mathrm{Re}\left[\mathbf{E}_0 e^{j(\omega_f t - \mathbf{k}\cdot\mathbf{r})}\right] = \mathrm{Re}\left[\mathbf{E}_0 e^{j\omega_f t - j(k_x x + k_y y + k_z z)}\right] \tag{2.5}$$

with,

$$\mathbf{E}(\mathbf{r}) \cdot \mathbf{k} = 0 \tag{2.6}$$

The general polarization form of Equation (2.5), representing an EM wave propagating along the positive z axis in a loss-free medium, can be expressed in vector form as:

$$\mathbf{E}(z, t) = \begin{bmatrix} E_{0_x}\cos\left(\omega_f t - kz + \delta_x\right) \\ E_{0_y}\cos\left(\omega_f t - kz + \delta_y\right) \\ 0 \end{bmatrix} \tag{2.7}$$

where ω_f is the angular frequency, and k is the wavenumber. At time $t = t_0$, the electric field consists of two sinusoidal components, each with distinct amplitude and phase characteristics. For example, for a linearly polarized wave with $\delta_y = \delta_x$, the electric field vector describes a sine wave lying in a plane oriented at angle θ with respect to the x axis. In this case, the electric field is represented by:

$$\mathbf{E}(z_0, t) = \sqrt{E_{0x}^2 + E_{0y}^2}\begin{bmatrix}\cos\ \theta \\ \sin\ \theta \\ 0\end{bmatrix}\cos\left(\omega_f t_0 - kz + \delta_x\right) \tag{2.8}$$

The following subsection describes polarized EM waves in detail.

2.2.1 Polarized Electromagnetic Waves

The polarization of an EM wave is defined by the equation of its electric field vector $\mathbf{E}(z, t)$. The plane perpendicular to the propagation direction determines the wave's polarization. In the general case, the electric field traces an ellipse that describes the wave's polarization. This polarization ellipse is expressed in the following equation:

$$\left[\frac{E_x(z_0, t)}{E_{0_x}}\right]^2 - 2\frac{E_x(z_0, t)E_y(z_0, t)}{E_{0_x}E_{0_y}}\cos\left(\delta_y - \delta_x\right) + \left[\frac{E_y(z_0, t)}{E_{0_y}}\right]^2 = \sin\left(\delta_y - \delta_x\right) \tag{2.9}$$

The polarization ellipse can be characterized by three primary parameters: amplitude (A), orientation angle (θ), and ellipticity (τ). These parameters are defined as:

$$A = \sqrt{E_{0_x}^2 + E_{0_y}^2} \tag{2.10}$$

$$\tan\ 2\theta = 2\frac{E_{0_x}E_{0_y}}{E_{0_x}^2 - E_{0_y}^2}\cos\ \delta \tag{2.11}$$

$$\delta = \delta_y - \delta_x\ \text{ and }\ \theta \in [-\pi/2, \pi/2] \tag{2.11}$$

$$|\sin\ 2\tau| = 2\frac{E_{0_x}E_{0_y}}{E_{0_x}^2 + E_{0_y}^2}|\sin\ \delta| \tag{2.12}$$

2.2.1.1 Jones Vector Representation

The electric field vector of a polarized EM wave can be expressed using the Jones vector (Hurwitz & Jones, 1941; J. Lee & Pottier, 2017). This formalism captures the state of polarization in a compact matrix–vector form:

$$\mathbf{E} = Ae^{j\zeta}\begin{bmatrix}\cos\,\theta & -\sin\,\theta\\ \sin\,\theta & \cos\,\theta\end{bmatrix}\begin{bmatrix}\cos\,\tau\\ j\sin\,\tau\end{bmatrix} \tag{2.13}$$

where ζ is an absolute phase term. This representation is particularly useful for describing and analyzing multiple polarization states. The parameters of the polarization ellipse, such as amplitude, orientation, and ellipticity, can be directly derived from the Jones vector. Table 2.1 provides an overview of Jones vectors and their corresponding parameters for common polarization states.

Table 2.1 Electric field vector characteristics for various polarizations

Polarization state	Orientation (θ)	Ellipticity (τ)	Unit Jones Vector $\hat{\boldsymbol{u}}_{(x,y)}$
Horizontal (H)	0	0	$\hat{\boldsymbol{u}}_H = \begin{bmatrix}1\\0\end{bmatrix}$
Vertical (V)	$\pi/2$	0	$\hat{\boldsymbol{u}}_V = \begin{bmatrix}0\\1\end{bmatrix}$
Linear +45°	$\pi/4$	0	$\hat{\boldsymbol{u}}_{+45} = \frac{1}{\sqrt{2}}\begin{bmatrix}1\\1\end{bmatrix}$
Linear - 45	$-\pi/4$	0	$\hat{\boldsymbol{u}}_{-45} = \frac{1}{\sqrt{2}}\begin{bmatrix}1\\-1\end{bmatrix}$
Left circular	$\in\left[-\frac{\pi}{2},\frac{\pi}{2}\right]$	$\pi/4$	$\hat{\boldsymbol{u}}_L = \frac{1}{\sqrt{2}}\begin{bmatrix}1\\j\end{bmatrix}$
Right circular	$\in\left[-\frac{\pi}{2},\frac{\pi}{2}\right]$	$-\pi/4$	$\hat{\boldsymbol{u}}_R = \frac{1}{\sqrt{2}}\begin{bmatrix}1\\-j\end{bmatrix}$

2.2.2 Scattering Matrix

Consider $\boldsymbol{E}^i$ to denote the EM signal incident on a target and $\boldsymbol{E}^s$ to represent the backscattered signal. Based on far-field approximation, the scattered electric field $\boldsymbol{E}^s$ can be expressed as:

$$\boldsymbol{E}^s = E_h^s\hat{\boldsymbol{h}} + E_v^S\hat{\boldsymbol{v}} \tag{2.14}$$

where $\hat{\boldsymbol{h}}$ and $\hat{\boldsymbol{v}}$ are unit vectors corresponding to the horizontal and vertical polarizations, respectively. The incident and scattered electric fields are related through the Sinclair matrix, a complex 2×2 scattering matrix designated S (Kennaugh, 1951; Sinclair, 1950):

$$\begin{pmatrix} E_h^s \\ E_v^s \end{pmatrix} = \frac{e^{-jkr}}{r}\begin{pmatrix} S_{hh} & S_{hv} \\ S_{vh} & S_{vv} \end{pmatrix}\begin{pmatrix} E_h^i \\ E_v^i \end{pmatrix} = \frac{e^{-jkr}}{r}\boldsymbol{S}E^i \tag{2.15}$$

with the scattering matrix $\boldsymbol{S}$ expressed as:

$$S = \begin{pmatrix} S_{hh} & S_{hv} \\ S_{vh} & S_{vv} \end{pmatrix} \tag{2.16}$$

Here, k is the wavenumber of the incident wave, r is the distance between the target and the receiving sensor, and S_{pq} terms with $p, q = h, v$ represent complex scattering amplitudes. These amplitudes depend on the radar system's characteristics, scattering geometry, and target properties. The term $\frac{e^{-jkr}}{r}$ accounts for propagation effects in both amplitude and phase (Lee & Pottier, 2017). In the scattering matrix S, the components S_{hh} and S_{vv} are the co-polarized (co-pol or co-polar) components, while S_{hv} and S_{vh} are the cross-polarized (cross-pol or cross-polar) components. In a fully polarimetric system, all elements of the scattering matrix are measured, providing a complete polarization signature of the target. In partially polarimetric systems, only a subset of the matrix elements is measured, such as in single-pol or dual-pol systems (Woodhouse, 2017). The elements of the scattering matrix are critical to identifying scattering mechanisms in natural media and are widely used for classification and parameter estimation. The scattering coefficient for any scattering matrix element is defined as (J. Lee & Pottier, 2017):

$$\sigma_{pq} = 4\pi\left|S_{pq}\right|^2 \tag{2.17}$$

This coefficient represents the radar cross-section (RCS) of the target and depends on various factors, including wave frequency, polarization, imaging configuration directions represented by θ_o and ψ_o, object and target geometric structures, and dielectric properties(J. Lee & Pottier, 2017). A forward model F_{pq} can be formulated to relate the radar output to observation parameters and target characteristics, which is described by a set of n variables (Ulaby & El-Rayes, 1987):

$$S_{pq} = F_{pq}(k, \theta_o, \psi_o, a_1, a_2, a_3, \dots, a_n)\ p, q = h, v \tag{2.18}$$

Here, k, θ_o, and ψ are radar parameters (wave parameters), while $a_1, a_2, \dots, a_n$ are target parameters such as the vegetation and soil properties of forests. Forests are complex targets, with radar signals interacting with various layers including the canopy, sub-canopy, trunks, and ground. Key forest parameters relevant to this research include the following:

- **Geometric and structural properties** such as forest stand height, vertical three-dimensional structure, leaf presence, size, orientation, trunk thickness, and distribution.
- **Vegetation indices** including above-ground biomass (AGB), leaf area index (LAI), and plant water content (PWC).
- **Soil dielectric properties** including soil moisture content (SMC), texture, density, temperature, and composition.

For robust inversion models, radar outputs can include complex scattering matrix parameters, scattering coefficients, or higher-order radar measurements. For example, SAR backscatter may be used for single- or dual-pol imagery, decomposition parameters for PolSAR data, and complex correlation coefficients for polarized interferometric SAR (PolInSAR) data to characterize a target in terms of forest biomass and structural properties (2.18).

2.3 Polarimetric Radar Remote Sensing

2.3.1 Brief Background

Polarimetric radar systems are designed to transmit and receive microwave signals that are either horizontally (H) or vertically (V) polarized. These systems measure both H- and V-polarized backscatter signals, providing rich information about target properties. The concept of the scattering matrix was introduced by Sinclair (1950), and its application to radar remote sensing was pioneered by Kennaugh (1951).

The development of fully polarimetric radar systems has been a gradual process, primarily due to the technological complexities involved. However, significant milestones have been achieved, such as the acquisition by the United States National Aeronautics and Space Administration (NASA) of the first fully PolSAR imagery over San Francisco using the Airborne Synthetic Aperture Radar (AIRSAR) sensor in 1985, and the launch of NASA's Spaceborne Imaging Radar-C (SIR-C) in 1994, which was the first fully polarimetric space-borne SAR system. This was followed by the Japan Aerospace Exploration Agency (JAXA) sensor, designated as Phased Array type L-band Synthetic Aperture Radar (ALOS/PALSAR) in 2006, the German Aerospace Center (DLR) X-band satellite TerraSAR-X and TerraSAR-X add-on for Digital Elevation Measurement (TanDEM-X; both 2010), and the JAXA ALOS-2/PALSAR-2 (2014).

2.3.2 Coherence Matrix

The scattering matrix S contains critical information about the target's scattering behavior and can be decomposed into fundamental scattering mechanisms associated with simpler objects. Meaningful information was extracted from the scattering matrix using vector representations. In the case of monostatic backscattering, in which the internal state of the target remains unchanged by the polarization of the transmitted signal, the reciprocity theorem holds. This theorem asserts that the two cross-polarized components are identical, i.e., $S_{hv} = S_{vh}$. For natural targets, such as forests, reciprocity is generally applicable, indicating that the cross-polarized elements in the scattering matrix are equal. To further assess scattering behavior, the elements of the scattering matrix S are projected onto the Pauli matrix basis to form the scattering (or target) vector in Pauli representation, facilitating decomposition and interpretation of the target's scattering mechanisms.

$$\boldsymbol{k}_p = \frac{1}{\sqrt{2}}[S_{hh} + S_{vv} \quad S_{hh} - S_{vv} \quad S_{hv} + S_{vh} \quad j(S_{hv} - S_{vh})]^T \tag{2.19}$$

Assuming reciprocity, the Pauli-basis target vector becomes:

$$\boldsymbol{k}_p = \frac{1}{\sqrt{2}}[S_{hh} + S_{vv} \quad S_{hh} - S_{vv} \quad 2S_{hv}]^T \tag{2.20}$$

where ^{T} is the transpose operator. The scattering matrix S and the target vector $\boldsymbol{k}_p$ are considered first-order polarimetric parameters that provide scattering information for individual pixels. However, in real-world scenarios, a single SAR pixel typically contains contributions from multiple scatterers. The resulting pixel-level scattering response is thus an average of the responses received from individual targets. Additionally, a single target may exhibit multiple scattering mechanisms. To statistically measure scattering behavior over a region, second-order polarimetric parameters such as the coherence matrix are employed. The coherence matrix is defined as follows:

$$\boldsymbol{T} = \langle \boldsymbol{k}_p \boldsymbol{k}_p{}^{*T} \rangle \tag{2.21}$$

$$\boldsymbol{T} = \begin{bmatrix} T_{11} & T_{12} & T_{13} \\ T_{21} & T_{22} & T_{23} \\ T_{31} & T_{32} & T_{33} \end{bmatrix} = \begin{bmatrix} T_{11} & T_{12} & T_{13} \\ T_{12}^* & T_{22} & T_{23} \\ T_{13}^* & T_{23}^* & T_{33} \end{bmatrix} \tag{2.22}$$

where $\langle \cdot \rangle$ denotes the expectation operator, which corresponds to spatial averaging in the context of SAR data, and the conjugation operator is indicated by *.

2.3.3 Target Decomposition

Polarimetric decomposition techniques aim to break down the backscattered signal into the sum of multiple scattering contributions. These techniques provide deep insights into scattering mechanisms, aiding in target classification and biophysical parameter estimation (Freeman & Durden, 1998). Decomposition methods are generally divided into two main categories: coherent and incoherent decomposition techniques. A brief overview of each method is provided below.

2.3.3.1 Coherent Decomposition

Coherence decomposition expresses the measured scattering matrix of a target as a combination of scattering responses from multiple simple or canonical scatterers (S. R. Cloude & Pottier, 1996; Munro, 2011).

$$S = \sum_{i=1}^{k} c_i S_i \tag{2.23}$$

In this equation, S_i represents the scattering response of each canonical scatterer, and c_i is its corresponding weight. A common example is Pauli decomposition, in which the scattering matrix is expressed as the sum of three or four canonical scattering responses, depending on whether reciprocity is assumed. Pioneering work in coherent decomposition was carried out by Krogager (1990), who proposed a model for decomposing the scattering matrix into the scattering contributions of a sphere, diplane, and helix. However, a key challenge in coherent decomposition lies in the interference among scattered fields, which causes speckle noise (J. Lee & Pottier, 2017). Moreover, in practical applications, the scattering matrix rarely corresponds perfectly to a single canonical scatterer, as most real-world targets exhibit complex scattering behaviors (J. Lee & Pottier, 2017).

2.3.3.2 Incoherent Decomposition

Although coherent decomposition is suitable for characterizing pure scatterers, it is insufficient for distributed targets. For such targets, second-order polarimetric parameters, such as the coherence matrix (T), are required. Incoherent decomposition techniques utilize statistical descriptors to extract scattering information and reduce speckle noise through averaging. These techniques are further divided into two sub-categories: eigenvector-based decomposition and model-based decomposition.

Eigenvector-based decomposition involves decomposing the coherence matrix $\boldsymbol{T}$ into the weighted contributions of three independent scattering mechanisms:

$$\boldsymbol{T} = \sum_{i=1}^{3} \lambda_i \cdot \mu_i \cdot \mu_i^{*T} = \boldsymbol{T}_{01} + \boldsymbol{T}_{02} + \boldsymbol{T}_{03} \tag{2.24}$$

where μ_i and λ_i (with $i = 1\text{–}3$) are the three-unit orthogonal eigenvectors and eigenvalues, respectively. This decomposition process identifies the dominant scattering mechanism based on the largest eigenvalue (R. Cloude & Pottier, 1996). The resulting scattering components are typically classified into surface, dihedral, and volume scattering mechanisms (Cloude, 1992). In 1997, Cloude and Pottier introduced the H-A-alpha decomposition, which characterizes scattering behavior using the parameters entropy (H), anisotropy (A), and alpha angle (α). This decomposition method has been widely applied across remote sensing applications (Ainsworth et al., 2002; J. Lee & Pottier, 2017).

Lavalle and Khun (Lavalle and Khun, 2014) extended the H-A-alpha decomposition to dual-polarization SAR data, using only the H and alpha parameters. This method has proven effective in distinguishing among scattering mechanisms in vegetation and forest studies, with parameters such as backscatter intensity and H-alpha values employed to identify clear-cut areas (Santoro et al., 2009).

Model-based decomposition: One limitation of eigenvector-based decomposition is the difficulty of assigning physical interpretations to decomposed components. In contrast, model-based decomposition techniques represent the coherence matrix as a linear combination of scattering contributions, each of which is associated with a specific physical attribute. The Freeman–Durden decomposition (FDD) method (Freeman and Durden, 1998) divides the coherence matrix into three fundamental scattering components: surface scattering, dihedral (double-bounce) scattering, and volume scattering (Lee et al., 2011). The coherence matrix for FDD is expressed as follows:

$$\boldsymbol{T} = P_s \begin{bmatrix} 1 & \beta^* & 0 \\ \beta & |\beta|^2 & 0 \\ 0 & 0 & 0 \end{bmatrix} + P_d \begin{bmatrix} |\alpha|^2 & \alpha & 0 \\ \alpha^* & 1 & 0 \\ 0 & 0 & 0 \end{bmatrix} + P_v \begin{bmatrix} 2 & 0 & 0 \\ 0 & 1 & 0 \\ 0 & 0 & 1 \end{bmatrix}$$

where α and β are complex observables for dihedral and surface scattering, respectively. The terms P_s, P_d, and P_v are the surface, double-bounce, and volume scattering powers, respectively. The Yamaguchi decomposition technique (Yamaguchi et al., 2005) extended the FDD by adding a fourth term for helix scattering to account for asymmetric terrain reflections. Yamaguchi decomposition was later modified (Yamaguchi et al., 2011). Further modification (Touzi, 2016) incorporated compensation for polarization orientation shifts, further refining the model. However, both the FDD and Yamaguchi decomposition methods have challenges, including the occurrence of negative scattering powers and incomplete utilization of coherence matrix information. To address these limitations, the general four-component scattering power decomposition with unitary transformation (G4U) technique was introduced (Singh et al., 2013), which fully exploits the information content of the coherence matrix. Although G4U resolves some challenges, issues related to negative scattering powers persist. Recent advances include six-component and seven-component models (Singh et al., 2019; Singh & Yamaguchi, 2018), which incorporate additional scattering terms such as compound and oriented dihedral scattering.

Chapter 3 : Forest Above-ground Biomass Retrieval Based on the PolSAR Decomposition Technique Using L-Band SAR Data

3.1. Introduction

Forests, which cover more than one third of Earth's surface, have a marked impact on the global climate due to their essential role in the carbon cycle. The definition of forests varies across countries and organizations. According to the Food and Agriculture Organization (FAO), a forest is characterized as "land covering more than 0.5 hectares with trees that exceed 5 meters in height and maintain a canopy cover of at least 10 percent, or with trees capable of achieving these thresholds in their natural environment." This definition explicitly excludes areas primarily used for agricultural or urban purposes (FAO, 2018). These vast ecosystems not only provide enormous biodiversity but are also important for mitigating climate change (Makhado et al., 2011; Wei et al., 2022). Biophysical indicators are data sources for understanding and monitoring forest health and include height, structure, density, and biomass, each of which provides insight into the state of a forest ecosystem(Chere et al., 2023; Jennings, 1999; Pretzsch, 2009; Wang et al., 2019; Xu et al., 2019). Aboveground biomass (AGB) is among the most important of these indicators (Metz et al., 2007; Saatchi et al., 2007). AGB reflects the total mass of all aboveground vegetation in a forest and is comprised of about 50% carbon. This carbon concentration is critical to the ability of forests to act as carbon sinks, effectively sequestering carbon from the atmosphere.

AGB is comprised of plant structures including stems, branches, bark, seeds, flowers, and leaves. These structures store the carbon that plants receive via photosynthesis (Pan et al., 2011). Quantifying AGB not only provides insight into the health of the forest but also enables assessment of its capacity to store carbon dioxide, a greenhouse gas critical to global climate dynamics (Ellison et al., 2017; Rajashekar et al., 2018) . In the face of anthropogenic climate change, research and monitoring of AGB is important for informed environmental management and conservation initiatives(Brown, 2002; Clark & Clark, 2000; Slik et al., 2010). The pressure on forests is mounting as a result of rapid industrialization and the conversion of forest lands into agricultural areas (Abugre & Sackey, 2022; Goers et al., 2012; Worku & Ayalew, 2024), especially in densely populated countries like India (Khati et al., 2017). Accurate assessment of AGB at a global level is important for mitigating emissions arising from deforestation and forest degradation, which is the goal of the Reducing Emissions from Deforestation and Degradation (REDD+) program (Campbell, 2009; Canadell et al., 2004; Peregon & Yamagata, 2013b).

AGB is typically expressed in metric tons of carbon per hectare or metric tons of dry matter per hectare. Manual approaches for calculating forest biomass are accurate but time-consuming, labor-intensive, and have limited spatial coverage. Remote-sensing technology has emerged as an important tool for forest health evaluation and monitoring (Gibbs et al., 2007; Rodríguez-Veiga et al., 2017). The synthetic aperture radar (SAR) approach has high sensitivity for forest biophysical variables, including canopy height, stand volume, AGB, leaf area index and plant area index(Avtar et al., 2017; Priyanka et al., 2023; Suab et al., 2024). Furthermore, SAR can monitor forest disturbances due to high penetration through the canopy (Avtar et al., 2012, 2013; Behera et al., 2016; Hong et al., 2019; Mitchard et al., 2009a; Thapa et al., 2015). The penetration depth of SAR signals interacting with the forest canopy is influenced by moisture (dielectric constant representing the quantity of water within and atop vegetation), the density of the canopy, and the radar wavelength (Khati et al., 2018). Fully polarimetric SAR data, which involves measuring quad-polarization combinations of transmitted and received electromagnetic signals, enables extraction of information on various features in a single SAR resolution cell (Singh et al., 2019).

L-band polarimetric SAR (PolSAR) enables observation of multiple layers of the forest canopy and sub-canopy. Research on this topic, which is nascent, has the potential to estimate the mass of carbon stored in Earth’s forests. The majority of studies used single- or dual-polarimetric SAR data to develop models for estimating forest AGB (Mutanga, 2016; Rodríguez-Veiga et al., 2017a); SAR backscatter was typically employed. However, the accuracy of biomass retrieval is affected by the type and structure of the forest, the terrain slope, and the frequency with which SAR data are used.

In most of the studies which are conducted to estimate AGB using SAR, backscattering and forest height have been employed as the predictor variables (Ji et al., 2020; Khati & Singh, 2022; Mermoz et al., 2015; Mitchard et al., 2009b; Sileshi, 2014; Verma & Ghosh, 2022; Yadav

& Nandy, 2015). To accurately estimate forest height, it is necessary to utilize multiple satellite data sets with a minimum temporal gap between them. Existing methods are site-specific, necessitating the development of a technique that can estimate pan-India biomass using a single-stage SAR dataset with reduced error. By decomposing the SAR data into different scattering mechanisms, we can analyze specific contributions due to different forest structures(Y. Wang & Davis, 1997). In this study, a novel method to estimate forest biomass has been developed. A combination of a machine-learning random forest regression and scattering ability derived from a seven-component decomposition (7SD) was used to predict AGB in a biodiverse region of India. This marks the first use of scattering powers to map forest AGB in a tropical Indian forest. The 7SD is an advanced technique in polarimetric Synthetic Aperture Radar (PolSAR) for analyzing complex scattering mechanisms in forested areas. This method extends traditional three-component decompositions (surface, double-bounce, and volume scattering) by incorporating additional scattering types to better characterize diverse and intricate forest structures. In situations with anisotropic media, particularly in heterogeneous forests, all PolSAR relative phase information and parameters may be important (Yamaguchi, 2020). Consequently, the conventional reflection-symmetric polarimetric scattering decomposition model might not be suitable. Instead, PolSAR (non-reflection symmetric) 7SD algorithm (Singh et al., 2019) has been implemented for the forest region in this study. The aim was to examine the potential of Full PolSAR 7SD for analyzing forest biomass using a random forest machine-learning method. Initially, I identified the optimal scattering-power combination, which was strongly correlated with biomass; the combination was subsequently used to train and validate the 7SD-RFR-AGB model.

3.2 Study Area and Datasets

3.2.1. Test Sites

Based on the availability of the field and satellite data, two forest sites have been selected in this study for the development and validation of the model.

3.2.1.1. Shivamogga

Shivamogga Forest is located in Karnataka, India, from 13° 35' to 14° 10' N latitude to 75° 5' to 75° 45' E longitude (Figure 3.1). It has a varied topography, with elevations ranging from 534 to 1464 meters above mean sea level and supports a diverse range of ecosystems and habitats. The Shivamogga forest is in the Western Ghats, a mountainous region with high biodiversity that is home to several endangered species. The height gradient from 534 to 1464 m leads to the establishment of several ecological niches and adds to the diverse forest types in the region. With an average annual temperature of 24.2°C, the climate in the study region is tropical. Rainfall is an important influence on the ecosystem, and the study region receives 1042 mm of precipitation annually. The southwest monsoon between June and September accounts for the majority of the rainfall and alters the vegetation patterns and the overall ecology of the region.

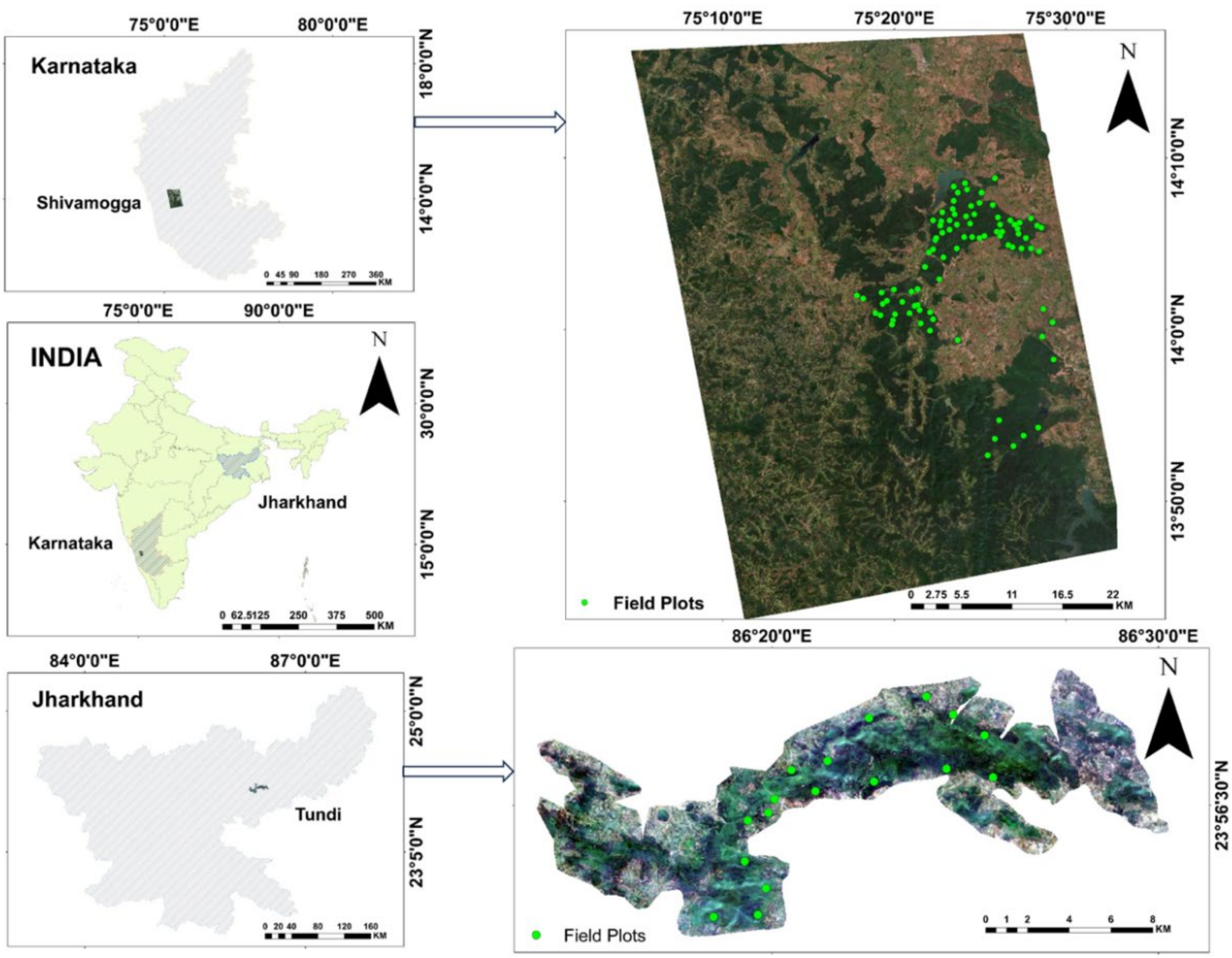

Figure 3.1 Test sites: The Shivamogga (Karnataka) and Tundi (Jharkhand) forest ranges images acquired by Sentinel- 2.

This forest division contains five southern tropical (ST) forest types: ST wet evergreen forests, ST semi-evergreen forests, ST moist deciduous forests, ST dry deciduous forests, and ST scrub forests. This study focused on a portion of the study region that contains ST moist deciduous forest, ST mixed dry-deciduous/scrub forest, and ST semi-evergreen forest. These indicate zones of medium, low, and high biomass, respectively.

3.2.1.2. Tundi

The study area is located in the Tundi Reserved Forest, part of Dhanbad District, Jharkhand, India (Champion & Seth, 1968). Forests in Jharkhand are classified as tropical-zone dry and tropical-zone wet forests (Forest Survey of India, 2019). It is located between latitudes 23° 53' 0'' N–24° 0 0' 0'' N and longitudes 86° 11' 0'' E–86° 30' 00'' E (Figure 1). The Tundi Reserved Forest is classified as a northern tropical dry deciduous forest by the Dhanbad Forest Division (Champion & Seth, 1968). The upper story of the Tundi forest cover is entirely composed of *Shorea robusta*, sometimes called 'Sal', and has an average height of 12 m. This forest range was used for cross-validation of the PolSAR AGB retrieval algorithm.

3.2.2. Dataset

3.2.2.1. Field data

To collect field data for the test sites, conducted field campaigns have been conducted in 2019 and 2020 during the dry season and obtained in situ measurements. A total of 88 observation plots for Shivamogga forest and 17 plots for Tundi forest, each of 31.6 × 31.6 m, were used for measurement of forest parameters (Table 3.1). For each sample plot, tree height and tree circumference at breast height (CBH) were measured. The forest height and biomass of trees with a CBH greater than 10 cm were considered. This is a natural forest, and it has many tree species. Dominant tree species in field plots are Teak (*Tectona grandis*), Jambe (*xylio xylocarpa*), Eucalyptus (Eucalyptus grandis), Dindega (*Anogeissus latifolia*), Acacia (*Acacia auriculiformis*), Mathi (*Terminalia tomentosa*), Mitli (*streblus asper*), Nandi *(Lagerstroemia lanceolata*), Honalu (*Terminalia paniculata*). The trees species-specific volumetric equations developed by the Forest Survey of India (1996) were used to calculate field biomass.

Table 3.1 Details of field data collection

Forest Site	Max AGB (Mg/ha)	Min AGB (Mg/ha)	Mean AGB (Mg/ha)	Mean Stand Height (m)
Shivamogga	319.58	15.24	117.97	15.32
Tundi	165.01	72.67	110.45	13.49

3.2.2.2. Satellite data

The Advanced Land Observing Satellite-2 (ALOS-2) dataset is characterized by the Phased Array type L-band Synthetic Aperture Radar-2 (PALSAR2), which offers enhanced capabilities over its predecessor(Arikawa et al., 2010; Okada et al., 2013; Shimada, 2013; Suzuki et al., 2012). The Advanced Land Observing Satellite-2 (ALOS-2) data set has been utilized extensively for the application of forest Aboveground Biomass (AGB) estimation(Hayashi et al., 2019; Tadono et al., 2019; Zhang et al., 2023). ALOS-2/PALSAR-2 datasets were acquired for both test sites. The fully polarimetric L-band POLSAR acquisitions from ALOS-2/PALSAR-2 were used in single-look complex format, enabling precise polarimetric model-based decomposition (Table 3.2).

Table 3.2 Acquisition of the PolSAR datasets

Forest Site	Satellite/Sensor	Date of Acquisition	Polarization	Off-Nadir Angle
Shivamogga	ALOS-2/PALSAR-2	2016-05-07	Quad-Polarization	28.4^0
Tundi	ALOS-2/PALSAR-2	2016-05-28	Quad-Polarization	35.3^0

3.3 Methodology

3.3.1. Radar-scattering matrix

The calibrated [*S*] data matrix was generated using ALOS-2/PALSAR-2 measurements (Equation 1):

$$[S] = k \begin{bmatrix} S_{HH} & S_{HV} \\ S_{VH} & S_{VV} \end{bmatrix}, \tag{3.1}$$

where k is the calibration factor.

The second-order coherency matrix was produced using [S] and Pauli basis matrices by considering spatial ensemble averaging, $\langle \ldots \rangle$, *i.e.*, multi-looking in the azimuth and range directions. Spatial ensemble averaging was performed by implementing a multi-look factor window of 3 × 7 (range × azimuth direction) to mitigate the impact of speckle. The spatial ensemble averaged coherency matrix is expressed as:

$$\langle [T] \rangle = \langle k k^{\dagger} \rangle = \begin{bmatrix} \langle |k_1|^2 \rangle & \langle k_1 k_2^{*} \rangle & \langle k_1 k_3^{*} \rangle \\ \langle k_2 k_1^{*} \rangle & \langle |k_2|^2 \rangle & \langle k_2 k_3^{*} \rangle \\ \langle k_3 k_1^{*} \rangle & \langle k_3 k_2^{*} \rangle & \langle |k_3|^2 \rangle \end{bmatrix} = \begin{bmatrix} T_{11} & T_{12} & T_{13} \\ T_{21} & T_{22} & T_{23} \\ T_{31} & T_{32} & T_{33} \end{bmatrix} \tag{3.2}$$

where * represents the complex conjugation, † denotes the complex conjugation and transposition, and

$$k = \frac{1}{\sqrt{2}} \begin{bmatrix} S_{HH} + S_{VV} \\ S_{HH} - S_{VV} \\ 2S_{HV} \end{bmatrix} = \begin{bmatrix} k_1 \\ k_2 \\ k_3 \end{bmatrix}, \tag{3.3}$$

Additionally, $\langle [T] \rangle$ produced a more realistic representation of the synthetic aperture radar (SAR) data that correspond to the ground, thereby revealing finer details. The use of 3 × 3 $\langle [T] \rangle$ enabled measurement of naturally occurring distributed targets. All incoherent decompositions were performed on the aforementioned $\langle [T] \rangle$ because of its strong correlation with the properties of the target. To achieve a more accurate representation of the real world, terrain correction was performed on the $\langle [T] \rangle$ using a 30 m posting Shuttle Topography Radar Mission Digital Elevation Model (SRTM-DEM)(L. Yang et al., 2011), which managed to correct foreshortening effect in hilly or mountainous areas and improved accuracy through slope adjustments and geometric correction. This ensured that each pixel represented accurate AGB calculations.

3.3.2. The 7SD Model

In heterogeneous forests, all PolSAR relative phase information/parameters could be important, and so the reflection symmetric based polarimetric scattering decomposition model may not be appropriate. Several model-based scattering power decomposition approaches have been reported (Freeman et al., 1998; Singh & Yamaguchi, 2018; Van Zyl et al., 2011; Yamaguchi et al., 2005b).

However, the most recent 7SD is better suited for cases with scattering from compound structures created by the combination of several dipoles in forest vegetation because 7SD expresses the maximum compound scattering components (Singh et al., 2019). It is important to create PolSAR (non-reflection symmetric) decomposition algorithms across the forest region using model-based 7SD representation (Singh et al., 2019). The 7SD elucidates the physical scattering mechanisms governing the seven elements of [T]. The decomposition of the overall scattering power into separate scattering submatrices is conducted as follows:

$$[\boldsymbol{T}] = P_s\,[T]_{\mathrm{s}} + P_d\,[T]_{\mathrm{d}} + \begin{cases} P_v[T]_{vol}^{dipole} \\ P_v[T]_{vol}^{dihedral} \end{cases} + P_h[T]_{\mathrm{h}} + P_{od}[T]_{od} + P_{cd-oqw}[T]_{cd-oqw} + P_{md}[T]_{md} \quad (3.4)$$

$$= \frac{P_s}{1+|\beta|^2}\begin{bmatrix} 1 & \beta^* & 0 \\ \beta & |\beta|^2 & 0 \\ 0 & 0 & 0 \end{bmatrix} + \frac{P_d}{1+|\alpha|^2}\begin{bmatrix} |\alpha|^2 & \alpha & 0 \\ \alpha^* & 1 & 0 \\ 0 & 0 & 0 \end{bmatrix}$$
$$+ P_v \left\{ \begin{array}{l} \frac{1}{4}\begin{bmatrix} 2 & 0 & 0 \\ 0 & 1 & 0 \\ 0 & 0 & 1 \end{bmatrix}; uniform\ distribution \\ \frac{1}{30}\begin{bmatrix} 15 & -5 & 0 \\ -5 & 7 & 0 \\ 0 & 0 & 8 \end{bmatrix}; cosine\ distribution \\ \frac{1}{30}\begin{bmatrix} 15 & 5 & 0 \\ 5 & 7 & 0 \\ 0 & 0 & 8 \end{bmatrix}; sine\ distribution \\ \frac{1}{15}\begin{bmatrix} 0 & 0 & 0 \\ 0 & 7 & 0 \\ 0 & 0 & 8 \end{bmatrix}; oriented\ dihedral \end{array} \right\} + \frac{P_h}{2}\begin{bmatrix} 0 & 0 & 0 \\ 0 & 1 & \pm j \\ 0 & \mp j & -1 \end{bmatrix} \quad (3.5)$$
$$+ \frac{P_{od}}{2}\begin{bmatrix} 1 & 0 & \pm 1 \\ 0 & 0 & 0 \\ \pm 1 & 0 & 1 \end{bmatrix} + \frac{P_{cd-oqw}}{2}\begin{bmatrix} 1 & 0 & \pm j \\ 0 & 0 & 0 \\ \mp j & 0 & 1 \end{bmatrix} + \frac{P_{md}}{2}\begin{bmatrix} 0 & 0 & 0 \\ 0 & 1 & \pm 1 \\ 0 & \pm 1 & 1 \end{bmatrix}$$

Four volume-scattering models (Sato et al., 2012) (Singh et al., 2013a) were added to Equation (4) using the depolarization process found in vegetated regions (marked by a cloud of dipoles) and structured areas with oriented dihedrals (such as urban zones). Three of these four volume-scattering models account for the HV component produced by plants with uniform, cosine, or sine distributions (Yamaguchi et al., 2005b, 2006). When there is a phase difference between

HH and VV, the volume-scattering model for oriented dihedrals is used in the decomposition framework (Singh & Yamaguchi, 2018). The surface-scattering power P_s, double-bounce scattering power P_d, volume-scattering power P_v, helix-scattering power P_h, oriented dipole-scattering power P_{od}, compound dipole (oriented quarter-wave reflector)-scattering power P_{cd-oqw} (P_{cd} hereafter), and mixed dipole-scattering power P_{md} are the scattering power components of 7SD (Singh et al., 2019).The research methodology is shown in Figure 3.2, and the methods are described below. The scattering power is extracted related to the field survey data for the model formation to estimate biomass. It is assumed that the forests where the field observation had been collected were in a mature state and not disturbed by human activities during the approximately 4-year gap between SAR data capture and field data collection. After the analysis combination of P_v, P_d, P_h, P_{cd}, and P_{md} showed the good trend with the forest biomass.

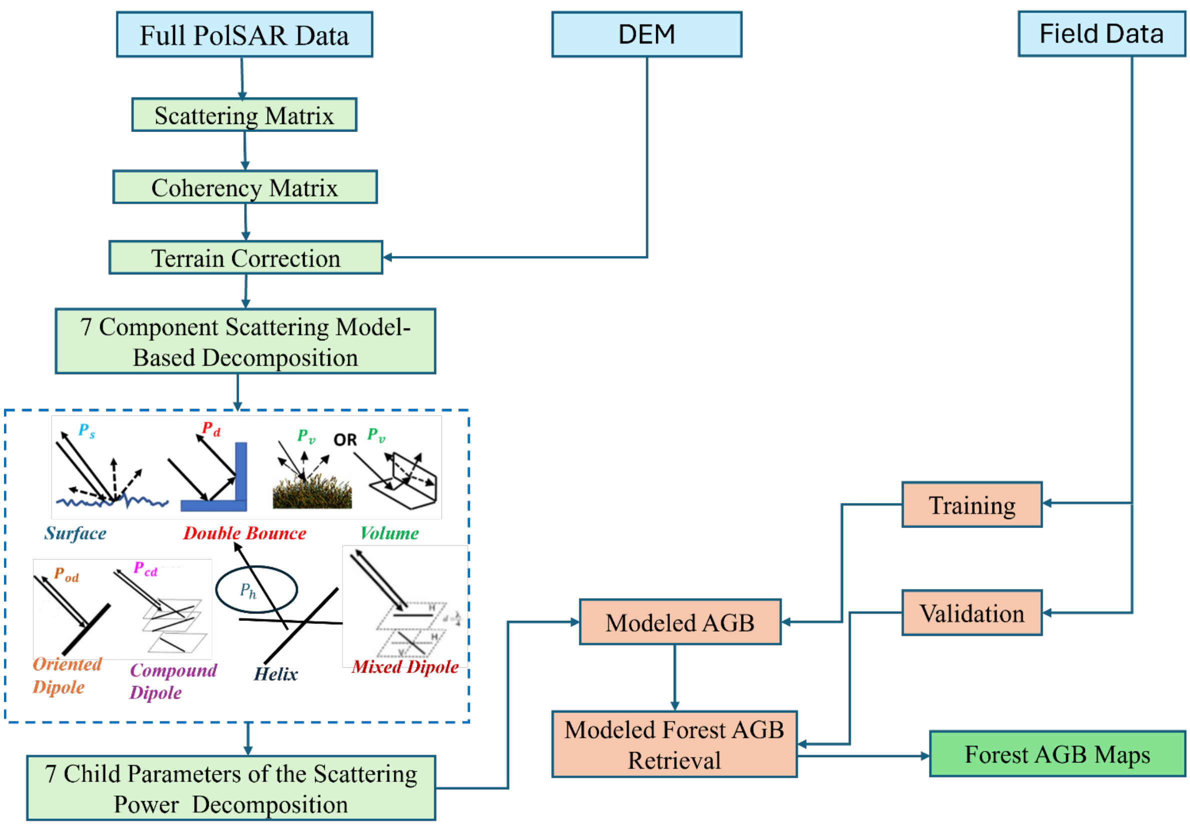

Figure 3.2 Flow chart of the research methodology

3.3.3. Sensitivity Analysis of 7SD

Sensitivity analysis using logarithmic correlation in the context of seven-component scattering power decomposition (7SD) in Synthetic Aperture Radar (SAR) data involves evaluating how variations in logarithmically transformed scattering components impact forest biomass estimation. Each component is logarithmically transformed to stabilize variance and normalize the data. Sensitivity is assessed by creating perturbations in each transformed component and observing the changes in biomass estimates. Regression analysis is performed using the transformed components as predictors and biomass as the response variable. The correlation coefficients help to identify the most sensitive and influential components. It provides a structured approach to understanding the impact of different scattering components on biomass estimation, enhancing the accuracy and reliability of SAR-based biomass models.

3.4. Modeling of Forest AGB Based on Decomposition

To model forest AGB, I used the machine learning technique of random forest regression. The random forest regression (RFR) algorithm is useful for forest biomass modeling and uses ensemble learning to precisely estimate and predict biomass. RFR, a machine learning technique, is favored for its ability to handle complex, non-linear relationships between predictor variables and forest AGB (Gleason & Im, 2012; Wu et al., 2016, 2024). The use of RFR with SAR data and vegetation indices has yielded favourable results for estimating AGB in tropical forests(Ghosh & Behera, 2018). A complete dataset comprising both remotely sensed data and ground-based observations is required. This approach trains individual decision trees to capture complicated correlations between input factors and forest biomass, with each tree examining a random subset of features. Hyperparameters are fine-tuned to ensure optimal model performance. Cross-validation approaches are used to validate the model's ability to infer biomass for both known and unknown regions. The assignation of relevance scores to each variable allows identification of critical factors that influence biomass.

To predict forest biomass, various combinations of scattering powers were used as predictor variables. In this study, 75% of ground samples were assigned to training and 25% for validation. Model performance was assessed by calculating root mean square error (RMSE) values.

3.4 Results and Discussion

The utility of ALOS-2/PALSAR2 L-band data-based 7SD and a random forest regression algorithm has been evaluated to estimate AGB in a tropical forest region in India.

3.4.1. Interpretation and Sensitivity Analysis of the 7SD components

Model-based decomposition indicates the relative contributions of several components to total forest biomass. The identification of key drivers such as dominant tree species, soil nutrient levels, and topographical features provides insight into biomass distribution. Understanding the ecological consequences of biomass components improves our ability to forecast how people will react to environmental changes. The identification of keystone species and ecological processes facilitate the formulation of conservation plans. The insights gained from this analysis will contribute to the development of sustainable forest management strategies. Adaptive management practices can be formulated for particular regions based on the key factors influencing biomass distribution. The 7SD was applied to the ALOS-2/PALSAR-2 datasets, and decomposition RGB image was created by implementing a standard color code for the 7SD (red for P_d, green for P_v, and blue for P_s) (Figure 3.3). The color-coded graphic shows that volume scattering dominates the forest areas. Over a few sites, such as those of sparse vegetation, dominant double-bounce scattering is detected. When an L-band radar signal penetrates vegetation, it interacts with the ground–trunk interface, resulting in dihedral-type scattering.

It is a result of large volume contributions and double bounce scattering powers in the woodland region. Forest is often regarded as volume overground and is thick enough to provide large volume returns at the L-band. A dense forest with high canopy density and biomass, by contrast, has higher volume dispersion as a result of fewer canopy gaps through which signals can penetrate the ground and ground–trunk interface. Compound scattering results from the copy branch interaction with the L-band signal. However, there was spatial variance in surface, volume, and double bounce scattering from the Shivamogga forest range compared to the other forest range (Figure 3).

Figure 3.3 shows maps of individual scattering powers (P_v , P_d , P_h , $P_{cd,}$ and P_{md}) across Shivamogga, to visualize their spatial variation. The compound scattering power variation (helix, mixed dipole, orientated dipole, and compound dipoles) showed the heterogeneity of the forest and was related to the spatial variation in volume over ground, canopy density, and canopy gap. The variation of normalized powers is shown in Figure 3. I investigated the relationships of, and variations in, scattering powers to evaluate their interactions with AGB (Figure 3) over Shivamogga. The small-scale random changes in P_h , P_{od} , and P_{cd} are the compound scattering components of the 7SD model decomposition, which reflect the heterogeneity of the medium. The medium is homogenous if the values of these components are zero. The behaviors of scattering powers, derived from 7SD with AGB, assist selection of an appropriate component and/or combination of components for AGB inversion. The feature variables showed strong relationships between the scattering power values and AGB. The seven scattering power feature parameters were strongly correlated with the values of P_d, P_v, P_h, P_{cd}, and P_{md}. Values of seven scattering power features with highly significant correlations has been used to create an AGB model . Figure 3.4 shows the relationship between forest AGB and the scattering power features. The correlation coefficients ranged from low to moderate accuracy, and the strongest associations were with P_{md}, P_{cd}, $P_{h,}$ and P_v.

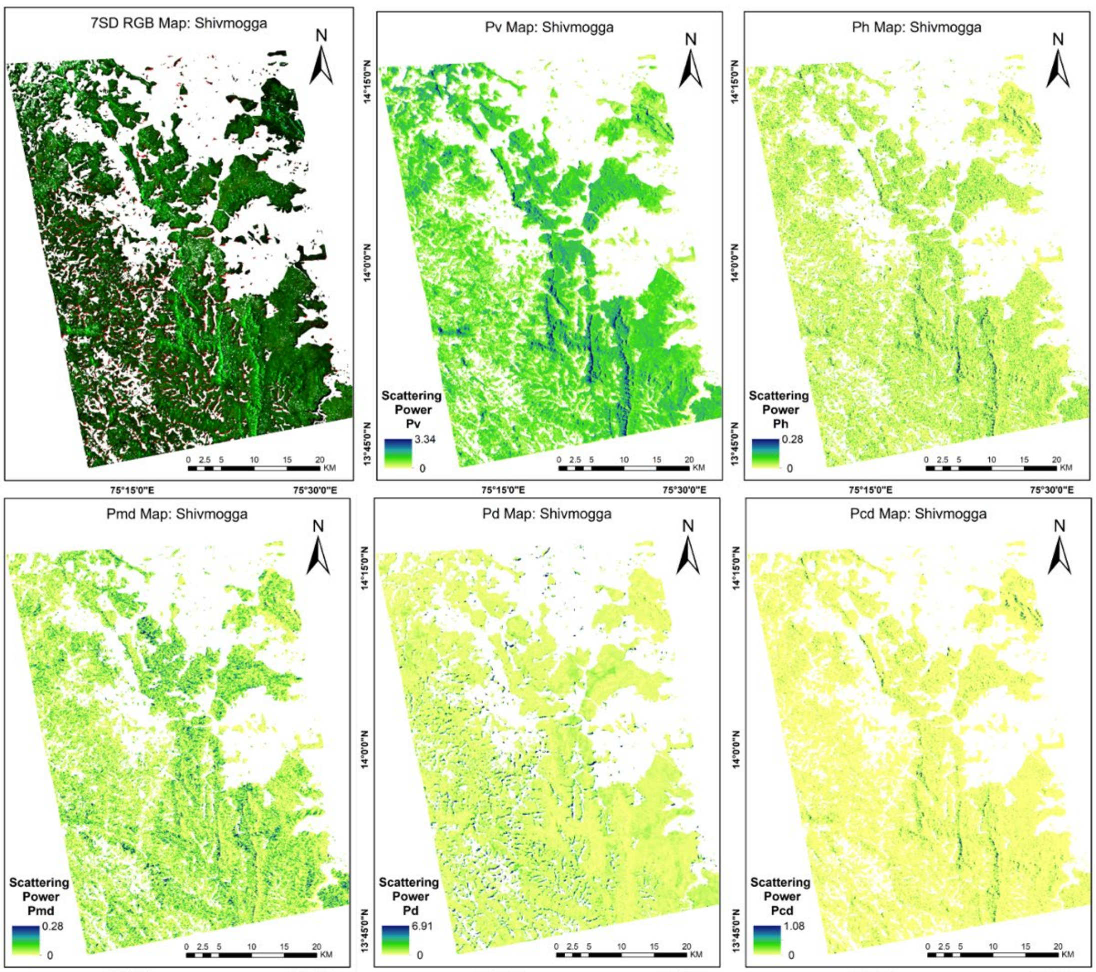

Figure 3.3 7SD RGB composite over a forest in western Ghat, India, and individual 7SD scattering powers (P_d, P_v, P_h, P_{cd}, and P_{md}) images showing the spatial variability of the scattering mechanisms.

Due to the high penetration power of the L band, the SAR signal interacted with different layers of the forest. Changes in scattering powers in a forest can be linked to changes in AGB, canopy density, and gaps (which increase with age and/or degradation). Because the tree has a vertical structure, it has a high anisotropy impact on radar interaction. Surface scattering varies little but tends to decrease as AGB increases. A very minor change in helix scattering (P_h) was noted. The trend line indicates that P_{od} and P_{cd} were high nearer to branches.

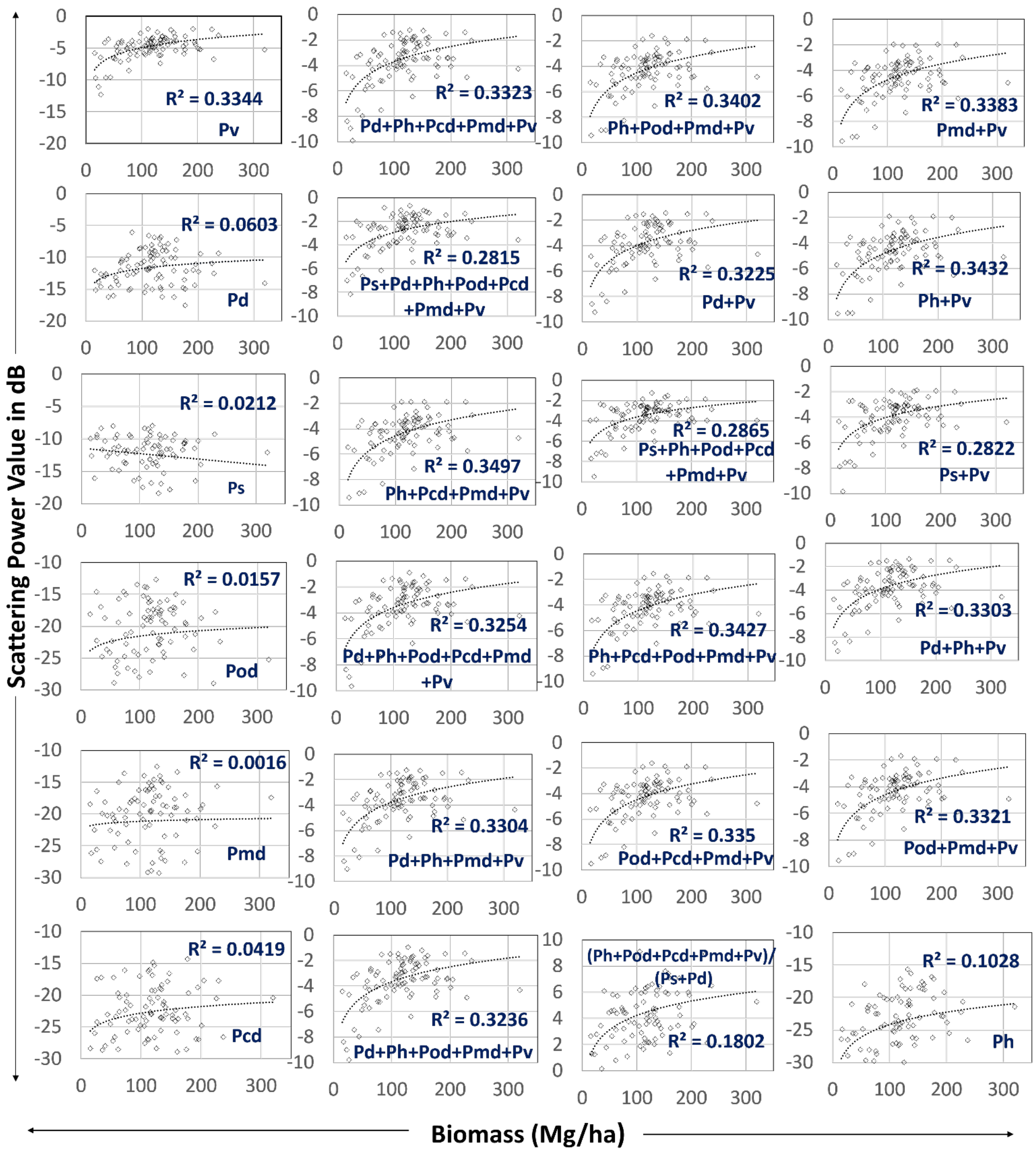

Figure 3.4 Relationships of 7SD scattering powers (P_s, P_d, P_v, P_h, P_{cd}, $P_{md,}$ and P_{od} and their combination) with AGB.

The forest region also exhibits considerable changes in P_{od} and P_{cd} because of an inhomogeneous AGB and the anisotropy effect. The dipole-type formations have horizontal and vertical orientations due to the inhomogeneous forest and branches. As a result, compound returns such as oriented dipole, mixed dipole, helix, and compound-orientated dipole scattering are detected. A few 7SD power combinations demonstrated a strong relationship with field-measured AGB. As a result, RFR was used to find relevant powers for creating more non-linear relations with AGB (Figure 3.5).

In the context of Random Forest models, %IncMSE and IncNodePurity are important metrics used to assess the importance of features (variables) in the model. These metrics help interpret the contribution of each feature to the predictive power of the model(Louppe et al., 2013).

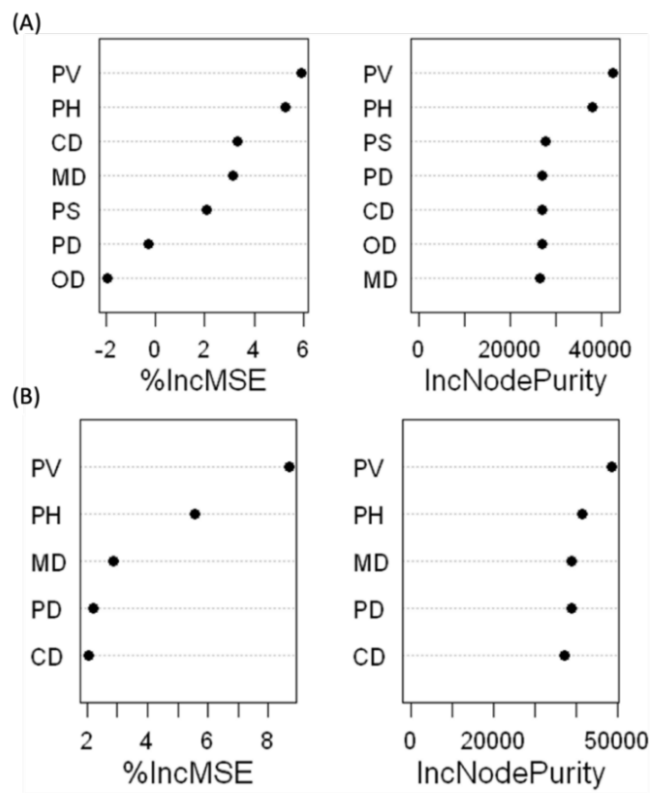

Figure 3.5 Variable importance chart. (A) All scattering powers and (B) ideal model

%IncMSE measures the increase in the mean squared error (MSE) of the model's predictions when a particular feature is permuted (shuffled) while all other features are kept constant. It essentially quantifies how much the accuracy of the model decreases if the information provided by that feature is no longer available. IncNodePurity is based on the Gini impurity (for classification tasks) or variance (for regression tasks) and measures the total decrease in node impurity (increase in node purity) that results from splits over that feature, averaged over all trees in the forest (Breiman, 2001). Using a random forest technique and variable importance analysis, several combinations of scattering powers generated from ALOS-2 data were analyzed to assess their influence on AGB dynamics. The results showed the importance of scattering power features for AGB estimation. Several combinations of scattering power features derived from ALOS-2 data were evaluated to assess their relationship with AGB. The findings suggest that knowledge of such relationships can improve the accuracy of biomass monitoring. Our findings provide insights into the ability of ALOS-2 scattering power to capture AGB dynamics, enhancing our understanding of vegetation structure and function.

3.4.2. Biomass Estimation

An initial random forest regression model with 500 decision trees was created to assess the feasibility of a seven-component model-based scattering power decomposition for estimating biomass in tropical forest environments, using 75% of the data for training and 25% for validation. The best performance was obtained after fine-tuning 500 decision trees. The accuracy of the model outperformed prior studies, particularly those using SAR backscatter as a predictive variable.

Biomass estimation was evaluated based on scattering, including that caused by interactions with tree trunks and branches as well as with leaves. An initial estimate using the 7SD scattering powers yielded a RMSE of 21.16%. The several scattering power combinations had been investigated; the ideal model included volume scattering, double bounce scattering, helix scattering, compound dipole, and mixed dipole. The concentration of biomass ranged from 44.15 Mg/ha to 219.94 Mg/ha, with an RMSE of 21.94 Mg/ha (%RMSE 19.46) (Figure 3.6). The biomass map in Figure 7 demonstrated lower biomass on the east side and at the margins, most likely for cultural reasons, and the despite being the protected forest area boundary of the forest showed signs of degradation and intact zone with the maximum biomass.

The scattering powers were utilized for estimation of AGB in tropical forests, considering single-stage and spatial variation effects. Full PolSAR 7SD enabled the retrieval of forest biomass using a random forest machine learning algorithm. The model had better accuracy than the studies which estimated biomass using SAR backscatter as a predictor variable. This model outperformed the other studies (Khati & Singh, 2022)estimated the forest biomass using L band backscatter and forest height derived from X band PolInSAR with RMSE 22%, (Kumar et al., 2012) estimated the forest biomass using C band backscatter and coherence with 35.92 Mg/ha RMSE, (Tomar et al., 2019) used the hybrid polarimetric decomposition techniques with rmse of around 25%, (Sinha et al., 2018)predicted biomass using C band with RMSE of 24.6 Mg/ha, (Nandy et al., 2017; B. K. Yadav & Nandy, 2015)estimate the forest biomass using the optical remote sensing with RMSE of 42.25 Mg/ha and 85.32 Mg/ha respectively.

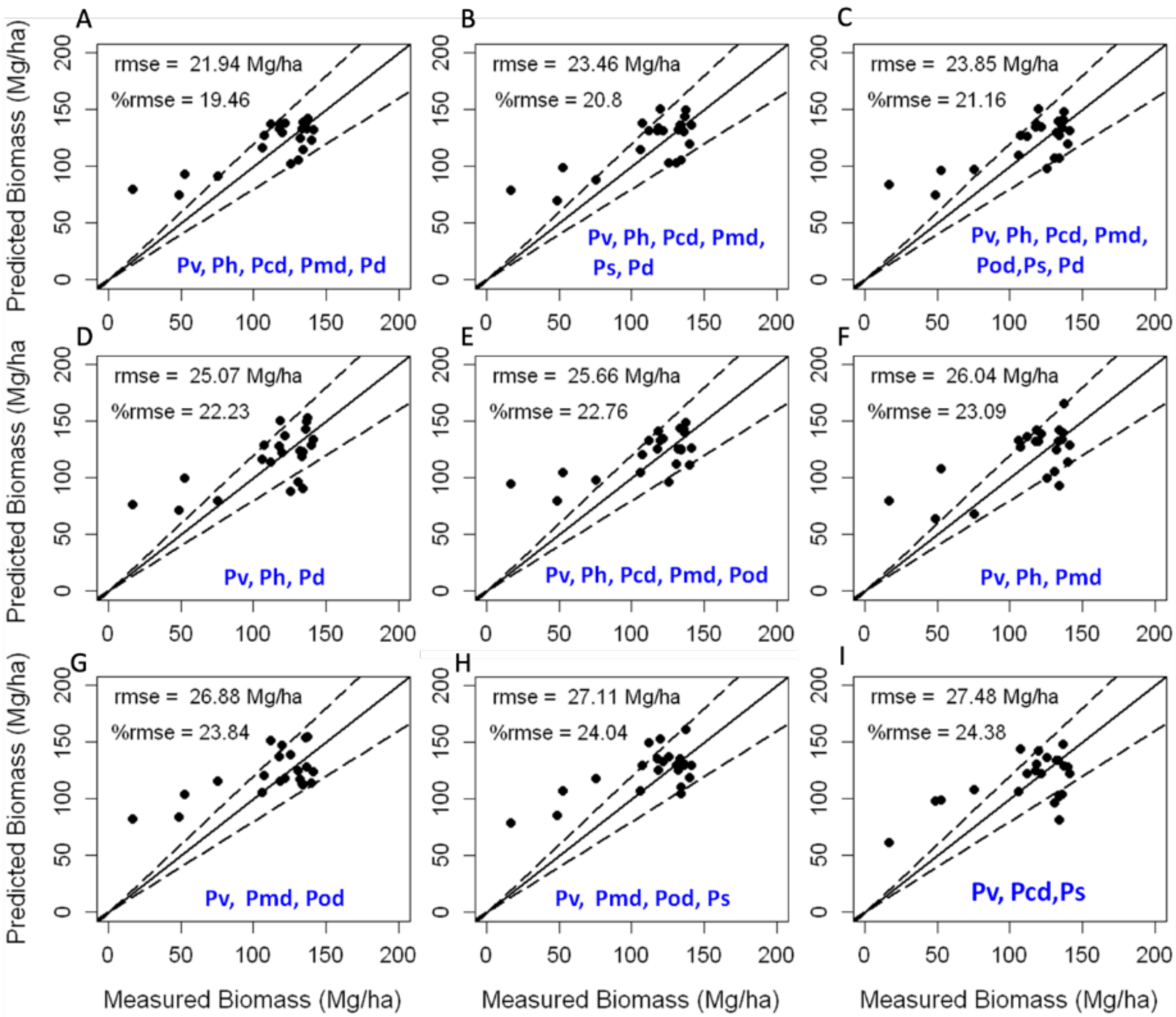

Figure 3.6 Validation of the modeled forest AGB derived from RFR models on combinations of scattering powers. (A) Best model for biomass estimation and (C) model using all scattering powers

Importantly, this study is the first to estimate biomass based on scattering powers, representing not only scattering from leaves but also interactions with tree trunks and branches. AGB variability was analyzed at the pixel level, fitting well with regional ground conditions, with estimates ranging from 44.15 to 219.94 Mg/ha. Spatial variability is shown in Figure 3.7.

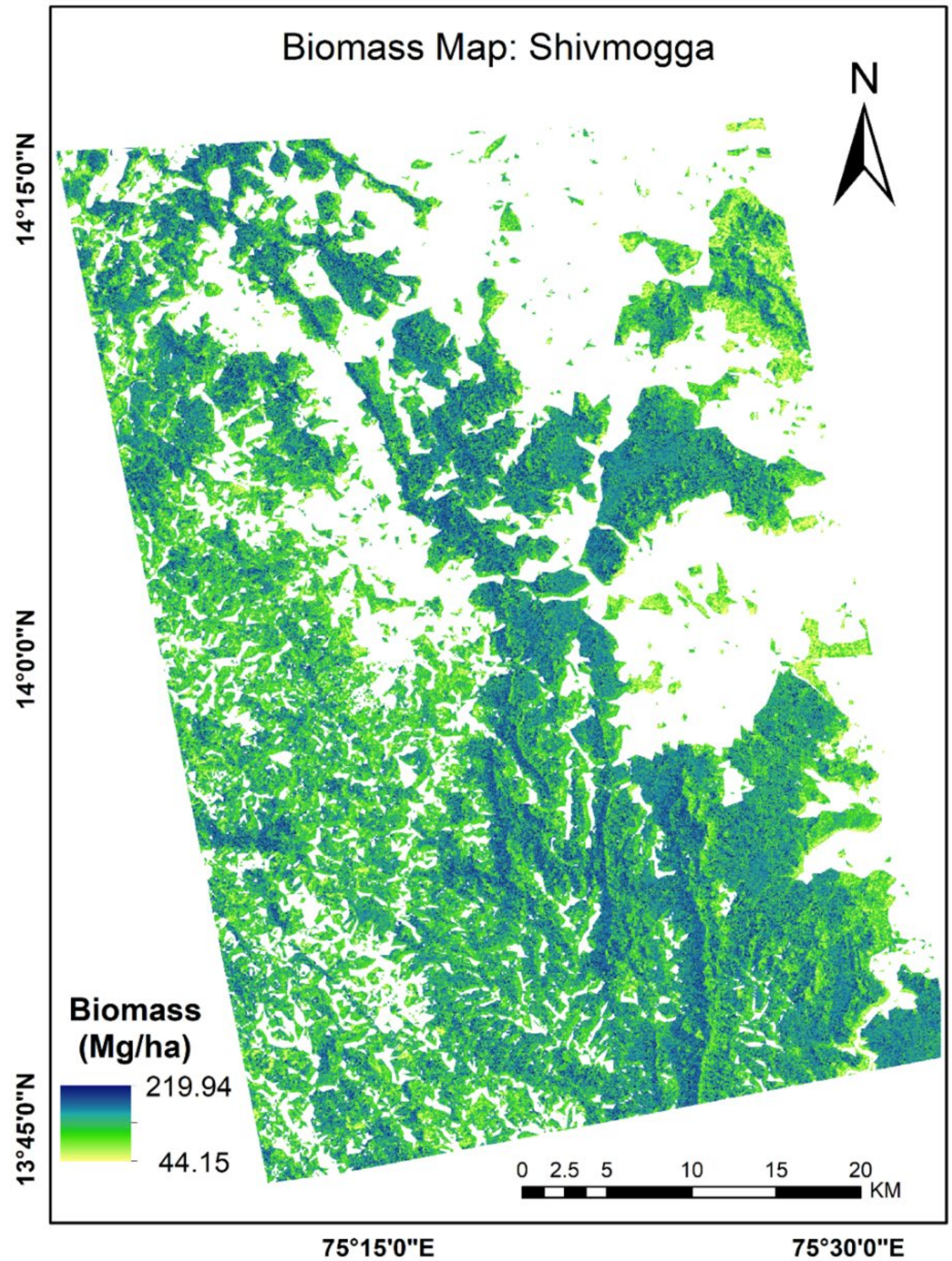

Figure 3.7 Spatial distribution of biomass in the Shivamogga Forest

3.4.3 Cross-validation of AGB Retrieval Model in Tundi Forest Range

7SD-RFR-AGB model was validated for model cross-validation. The AGB model was trained and validated using 7SD scattering powers from the same test site and acquisitions or data products in co-validation. By contrast, for model transferability and cross-validation, the developed AGB model was implemented at another test site and using another ALOS 2 acquisition-based 7SD, and validated (Figure 3.10). The AGB model was stable and suitable for transferability. An AGB map of Tundi was generated (Figure 3. 9). The accuracy of the model was qualitatively and quantitatively improved (Figure 3.10). The RMSE showed that the model's performance was good and stable. Overall, the model trained with the Shivamogga data performed well for inversion of the Tundi data.

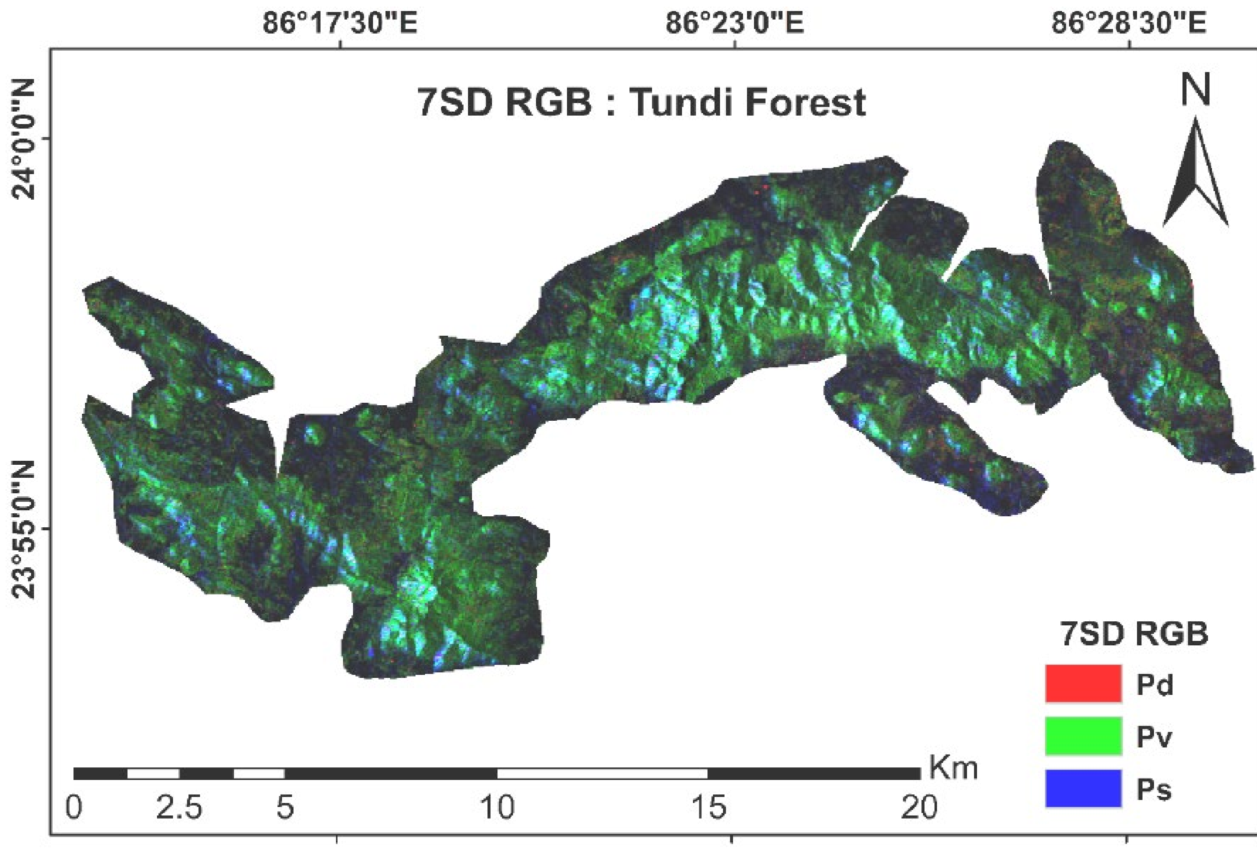

Figure 3.8 7SD RGB of the Tundi Forest

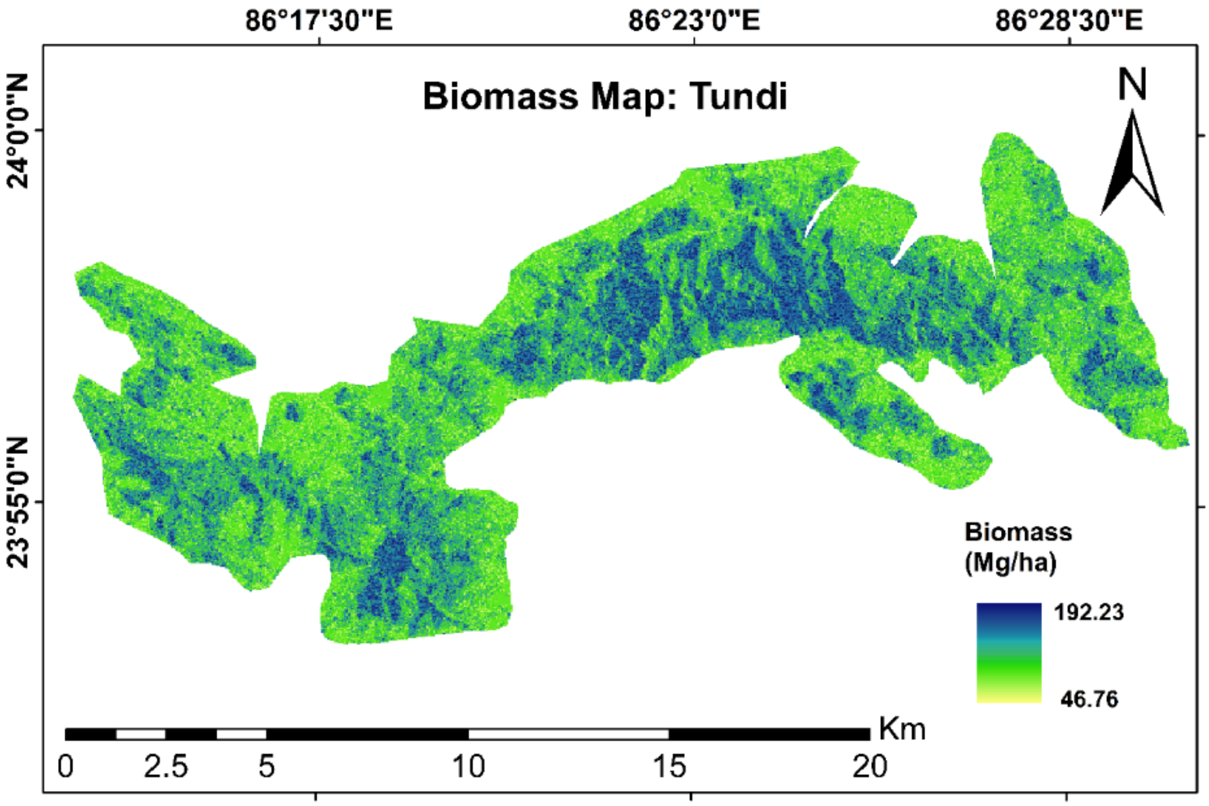

Figure 3.9 AGB map of the Tundi Forest

3.4.4 Cross-validation Performance of the Algorithm

The performance of the model was assessed using the RMSE and mean absolute error (MAE). The RMSE, MAE, and %RMSE were 25.3 Mg/ha, 21.23 Mg/ha, and 22.9%, respectively. Comparison of the estimated AGB values to those measured in the field (Figure 3.10) suggests that the model is useful for AGB estimation.

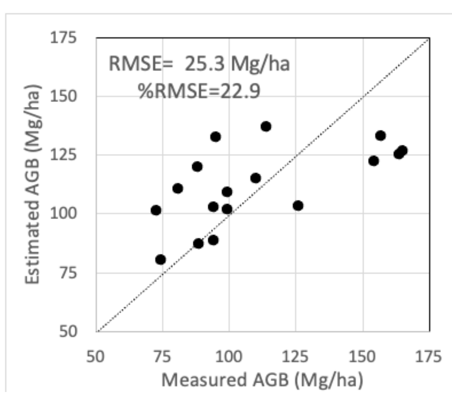

Figure 3.10 Validation of the estimated AGB in the Tundi Forest

The suggested inversion algorithm outperformed the AGB approach used previously with L-band dual-pol backscattering data (Avtar et al., 2014; Chang et al., 2018; Torre-Tojal et al., 2022). The RFR technique for AGB retrieval developed using 7SD enables monitoring of spatiotemporal AGB variations across forest ranges. To estimate the AGB, the model employs L-band fully polarimetric SAR measurements and accounts for seven scattering powers; forest height data are not needed. The AGB model facilitates the determination of AGB with reasonable error boundaries.

3.4.5. Effect of AGB on Estimation Performance

The effect of AGB on estimation performance was investigated using ALOS-2/PALSAR datasets over the Tundi Forest, to investigate the relationship between estimated AGB and absolute AGB error. For each field biomass plot, the absolute AGB error (|AGB measured−AGB estimated|) was calculated. A graph was created of the absolute AGB error for each biomass plot and the estimated biomass (Figure 3.11).

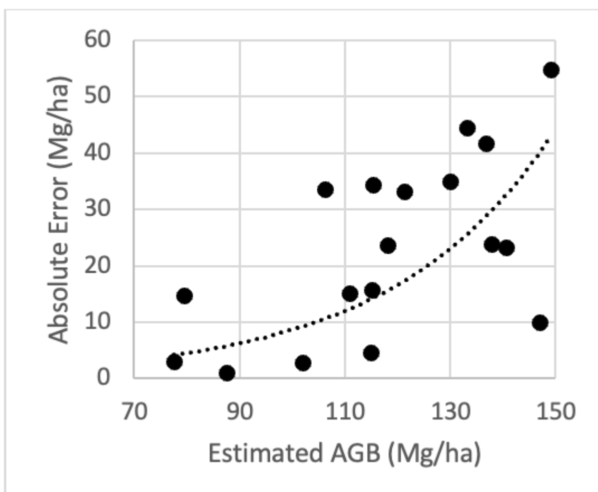

Figure 3.11 AGB error plot showing the relationship between estimated AGB and absolute AGB estimation error over the Tundi Forest.

The error for each biomass plot was related to the estimated biomass, demonstrating that the inversion performance error increases as AGB increases. In high AGB regions using the L-band, performance error is likely to be considerable. As the biomass rises, so will the attenuation and/or extinction coefficients, which are related to the phase velocity of an electromagnetic wave. When an electromagnetic wave passes through the forest, its wavelength is shortened. Therefore, the L-band is useful for retrieval of AGB up to 150 Mg/ha (Cartus et al., 2012; Dobson et al., 1992; Imhoff et al., 1986; Imhoff, 1995; Lucas et al., 2010; Lucas et al., 2006; Luckman, 1997; Mitchard et al., 2009a; Ranson et al., 1995; Saatchi et al., 2011; Saatchi et al., 2007b; Sandberg et al., 2011). Because of the enormous optical depth and dense canopy cover, the scatterers deep in the vegetation layer cannot interact with the incident wave. As a result, as saturation approaches in the L-band, the radar signal will attenuate significantly.

3.4.6 Discussion

This study evaluated the utility of a seven-component scattering power decomposition (7SD) model derived from ALOS-2/PALSAR-2 L-band SAR data and a Random Forest Regression (RFR) algorithm to estimate above-ground biomass (AGB) in tropical forests. The findings demonstrated the model's robust performance, emphasizing its potential to enhance biomass estimation accuracy while addressing spatial variability in biomass distribution.

The 7SD decomposition model used for the analysis of the interaction between radar signals and forest structure. By decomposing scattering powers into components such as volume scattering, double bounce scattering, helix scattering, compound dipole and mixed dipole, the study provided insights into the complex scattering mechanisms in tropical forests. The findings indicated strong correlations between scattering powers and AGB, reinforcing the importance of these parameters for biomass estimation. Volume scattering dominated in regions with dense forest canopies, while double-bounce scattering was more pronounced in areas with sparse vegetation, reflecting interactions at the ground-trunk interface. Compound scattering components highlighted forest heterogeneity, capturing variations in canopy density and gaps. The AGB estimation using the 7SD-RFR model is not available for any forest area worldwide. The results indicated that the 7SD-RFR model demonstrated superior performance compared to previous studies in terms of %RMSE and RMSE. Previous studies (Le Toan et al., 1992; Mitchard et al., 2009b, 2009a, 2009c; Peregon & Yamagata, 2013a, 2013b) and models mainly use single- and dual-polarimetric radar backscattering approaches. In the investigated test site, the estimation of AGB based on the proposed 7SD-RFR model is comparable to a recent study by (Musthafa et.al, 2022). The performance of the 7SD-RFR model at another test site indicates the model's effectiveness in estimating AGB using the proposed approach. In contrast, the proposed 7SD-RFR model can be replicated to estimate AGB in similar biomass forest ranges using fully polarimetric radar measurements without the inclusion of LiDAR data. However, for regional or global AGB estimation, the 7SD-RFR model needs to be tuned to cover a wider range of AGB across various forest covers globally.

While the model performed well, certain limitations were observed. The saturation effect of the L-band SAR in regions with high AGB (>150 Mg/ha) limits its accuracy in dense tropical forests. As biomass increases, the attenuation of radar signals due to the dense canopy reduces the ability to retrieve accurate AGB estimates. This issue could potentially be addressed by integrating multi-frequency SAR data (e.g., combining L-band with P- or X-band) or optical and LiDAR data to overcome saturation and improve accuracy. Temporal analysis of AGB dynamics using time-series SAR data could also provide insights into forest growth and degradation patterns. The ability to estimate AGB with high accuracy has significant implications for sustainable forest management. By identifying areas with low biomass (e.g., forest margins and degraded zones), targeted conservation efforts can be implemented. The insights into spatial variability in biomass also enable adaptive management strategies tailored to specific forest regions, ensuring better allocation of resources for restoration and conservation. The model's capability to work without additional forest height data simplifies its application, making it cost-effective and accessible for large-scale forest monitoring. The integration of such models into existing remote sensing frameworks can enhance the accuracy of biomass assessments, aiding in carbon stock estimation and climate change mitigation efforts.

3.5 Conclusion

Our findings suggest that scattering power combinations can be used for accurate biomass estimation. The 7SD decomposition approach and random forest regression machine-learning were used to develop the L-band PolSAR forest AGB retrieval model. Due to high penetration power of L band 7SD captured the heterogeneity of the forest. The 7SD volume-scattering parameter showed a strong correlation with AGB and, together with the compound scattering and double-bounce scattering powers, was used to model AGB. The AGB model was developed using fully polarimetric ALOS-2/PALSAR-2 datasets. The results of the AGB retrieval model were evaluated by comparison with field AGB measurements. The AGB estimated using full L-band POLSAR data correlated with the measured AGB with acceptable error (%RMSE 19.46%). The L-band full POLSAR data enabled analysis of AGB (up to 150 Mg/ha) in forest regions of India. Therefore, fully polarimetric ALOS-2/PALSAR-2 datasets enable accurate estimation of AGB at intermediate range. In future multi-frequency PolSAR inversion algorithm for AGB estimation using L-/C-band POLSAR data sets can be used to improve the accuracy of the model for evaluating forest dynamics.

Chapter 4 : Forest Biomass Estimation Using Multi-sensor Remote Sensing Data

4.1 Introduction

Forests are essential to the health of our planet and the well-being of all living organisms, providing numerous ecological, economic, and social benefits. The definition of forests varies among nations and organizations. According to the Food and Agriculture Organization (FAO), a forest is characterized as "land covering more than 0.5 hectares with trees that exceed 5 meters in height and maintain a canopy cover of at least 10 percent, or with trees capable of achieving these thresholds in their natural environment." This definition explicitly excludes areas primarily used for agricultural or urban purposes (FAO, 2018). Ecologically, forests are among the most diverse ecosystems, hosting over 80% of terrestrial species including animals, plants, and microorganisms (FAO, 2020; FAO (Ed.), 2016; Global Biodiversity Outlook 5.). Forests play a vital role in the global water cycle by influencing precipitation patterns and functioning as natural water filters, making them crucial for maintaining freshwater availability and quality (Ellison et al., 2017). Forests also prevent soil erosion, maintain soil fertility, support agriculture, and prevent natural disasters such as landslides. Moreover, forests play a pivotal role in climate regulation through carbon sequestration, the absorption of carbon dioxide, and storage of biomass. These functions mitigate the impacts of climate change, while deforestation and forest degradation significantly contribute to greenhouse gas emissions, highlighting the need for effective forest management (Houghton et al., 2009; Pan et al., 2011).

Forest biomass monitoring is critical for elucidating and managing the health and sustainability of forest ecosystems. Biomass, which includes all organic material in trees and other vegetation, plays a significant role in the global carbon cycle, as it sequesters carbon dioxide from the atmosphere (Pan et al., 2011). Accurate monitoring of forest biomass is essential for assessing carbon stocks, helping to combat climate change by informing carbon credit systems and climate policy decisions (Gibbs et al., 2007). Moreover, such monitoring supports forest management practices aimed at biodiversity conservation, sustainable resource use, and disaster risk reduction, such as fire management and pest control (Chave et al., 2005). Advances in remote sensing technologies and ground-based measurements have significantly enhanced the precision and reliability of biomass estimation, making it a vital tool for both environmental scientists and policymakers (Asner et al., 2010; Veiga et al., 2017b; Valbuena et al., 2017; X. Zhang & Nimeister, 2014). However, optical remote sensing has several limitations for forest biomass estimation. Cloud cover and atmospheric conditions can obstruct explicit imagery, affecting data quality (Foody et al., 2003; Kushwaha et al., 2016). This technique also struggles with canopy saturation, wherein dense forest canopies mask the understory, leading to underestimation of biomass (Lu, 2006). In addition, optical sensors are sensitive to variations in lighting and seasonal changes, which can introduce errors into biomass estimates. These limitations necessitate the integration of optical data with other remote sensing technologies, such as LiDAR and radar, to improve accuracy and reliability (Guerra-Hernández & Pascual, 2021; Mutanga & Skidmore, 2004; Silva et al., 2021; Tsui et al., 2013). Synthetic aperture radar (SAR) is a valuable tool for forest biomass estimation due to its ability to penetrate cloud cover and sensitivity to forest structure. SAR operates in the microwave region of the electromagnetic spectrum, providing data on the forest canopy and subcanopy layers. This method measures the backscattered signal, which correlates with biomass density, allowing for estimation of forest structure and volume (Ghasemi et al., 2011; Santoro et al., 2002). SAR data, particularly from sensors operating at L-band and P-band frequencies, are effective for estimating above-ground biomass (AGB) in dense tropical forests (Saatchi et al., 2011).

The use of multi-frequency SAR data encompassing the L-band and C-band frequencies enhances the precision of forest biomass estimation by leveraging the unique penetration and scattering properties of each band (Naidoo et al., 2015). L-band SAR, with its longer wavelength, penetrates deeper into the forest canopy, providing critical information about tree trunks and large branches, which are indicative of high biomass (Neumann et al., 2012; Sandberg et al., 2011; Schlund & Davidson, 2018; Thiel & Schmullius, 2016; Yu & Saatchi, 2016). C-band SAR, with intermediate penetration, captures details of the upper canopy layers, and thus is useful for assessing biomass in moderate-density forests (Bouvet et al., 2018). Combining multi-frequency data provides a more comprehensive picture of the forest structure and biomass to be obtained. Additionally, multi-frequency SAR data integration mitigates the limitations associated with using a single frequency, such as saturation issues in dense forests or insufficient penetration in sparse forests, thereby providing a robust tool for forest monitoring and management (Rignot et al., 2001).

Seven-component scattering power decomposition (7SD) is an advanced polarimetric SAR (PolSAR) technique developed for the analysis of complex scattering mechanisms in forested areas. This method extends the traditional three-component decomposition (surface, double-bounce, and volume scattering) by incorporating additional scattering types to better characterize diverse and complex forest structures. Biomass estimation using scattering power is an advanced method that leverages the unique scattering properties of forest canopies observed in radar data. This technique involves the analysis of multiple types of scattering mechanisms, including surface scattering, volume scattering, and double-bounce scattering, which correspond to various forest structures and densities. Leveraging these scattering components enables researchers to obtain detailed information about the biomass distribution within forests. This method enhances the accuracy of biomass estimates, particularly in complex and dense forest environments where traditional optical methods face challenges.

Despite the promising capabilities of multi-frequency (L-band and C-band) SAR data for forest biomass estimation, several research gaps remain. One significant gap is the integration of data from different SAR bands, which requires sophisticated algorithms and models to accurately correlate and merge the penetration depths and scattering properties of each frequency (Askne et al., 1997; Askne & Santoro, 2012; Berninger et al., 2018; Chave et al., 2014; Chowdhury et al., 2014; Luo et al., 2022; Mitchell et al., 2014). More extensive calibration and validation of these models across diverse forest types and environmental conditions is also needed to ensure their generalizability and accuracy (Santoro et al., 2021). This multi-frequency approach allows for the differentiation of biomass components at various canopy levels, increasing the accuracy of biomass estimation across diverse forest types and densities. LiDAR provides accurate forest stand height, which is used in allometric models to estimate forest biomass (Lefsky, Cohen, Harding, et al., 2002; Potapov et al., 2021a). The recently launched space-borne LiDAR platform GEDI (launched 5 December 2018), located on the International Space Station (Dubayah et al., 2020), acquires billions of LiDAR measurements with very low spatial separation in the along-track direction. Despite achieving significant progress toward the direct measurement of tree height and AGB, LiDAR data obtained from space (i.e., GEDI) provide only sample areas and transects, and thus cannot achieve wall-to-wall coverage of a large area (H. Huang et al., 2019). Geospatial techniques allow variables to be predicted or interpolated using existing known values of the predictor variable. Biomass estimation algorithms developed using single sensors contain uncertainty due to the limitations of the sensors. To obtain the optimal parameters from multiple sensors that are sensitive to biomass and thereby improve the accuracy of biophysical parameter retrieval, the fusion of multi-frequency SAR with LiDAR data has been proposed. Combination of SAR data acquired at multiple frequencies has improved biomass retrieval accuracy in several forest types (Cartus et al., 2017; Dobson et al., 1995; Huang et al., 2015; Ranson & Guoqing Sun, 1994; Saatchi et al., 2007; Santi et al., 2017). Studies have shown that the inclusion of forest stand height in radar backscatter reduces the error in biomass estimation. Forest stand height can be obtained from various remote sensing sources, including InSAR (Kumar et al., 2012), optical stereo-imaging (Persson et al., 2013), and LiDAR data (Deng et al., 2014; Dhargay et al., 2022a, 2022b; Fatoyinbo et al., 2021; Fayad et al., 2021; Lefsky, 2010; Lefsky, Cohen, Parker, et al., 2002; Liu et al., 2022; Potapov et al., 2021b; Schneider et al., 2020; Wang et al., 2022; Waqar et al., 2020; Wulder et al., 2012). In this study, I have explored complementary strengths of multi-sensor remote sensing data for forest biomass estimation. While the 7SD-RFR model proved effective in utilizing L-band PolSAR data for biomass retrieval, the inclusion of LiDAR-derived stand height data offers an opportunity to further enhance estimation accuracy by capturing vertical forest structure. This chapter integrates SAR and LiDAR datasets to address the limitations of single-sensor approaches, providing a more comprehensive understanding of forest biophysical parameters. By synergizing structural information from PolSAR data with height metrics from LiDAR, this multi-sensor approach aims to improve the precision of biomass estimation, particularly in dense and heterogeneous forest landscapes.

4.2 Study Area and Datasets

4.2.1. Shivamogga

The Shivamogga forest area is located in Karnataka, India, from 13° 35' to 14° 10' N latitude and 75° 5' to 75° 45' E longitude (Figure 4.1). This forest has a varied topography, with elevations ranging from 534 to 1,464 meters above mean sea level, and supports a diverse range of ecosystems and habitats. Shivamogga is located in the Western Ghats, a mountainous region with high biodiversity that is home to several endangered species. A height gradient from 534 to 1,464 m has led to the establishment of several ecological niches and supported diverse forest types in this region. With an average annual temperature of 24.2°C, the climate in the study region is tropical.

Rainfall is an important factor influencing the ecosystem, and the study region receives 1,042 mm of precipitation annually. The southwest monsoon between June and September accounts for the majority of annual rainfall, affecting the vegetation patterns and overall ecology of the region.

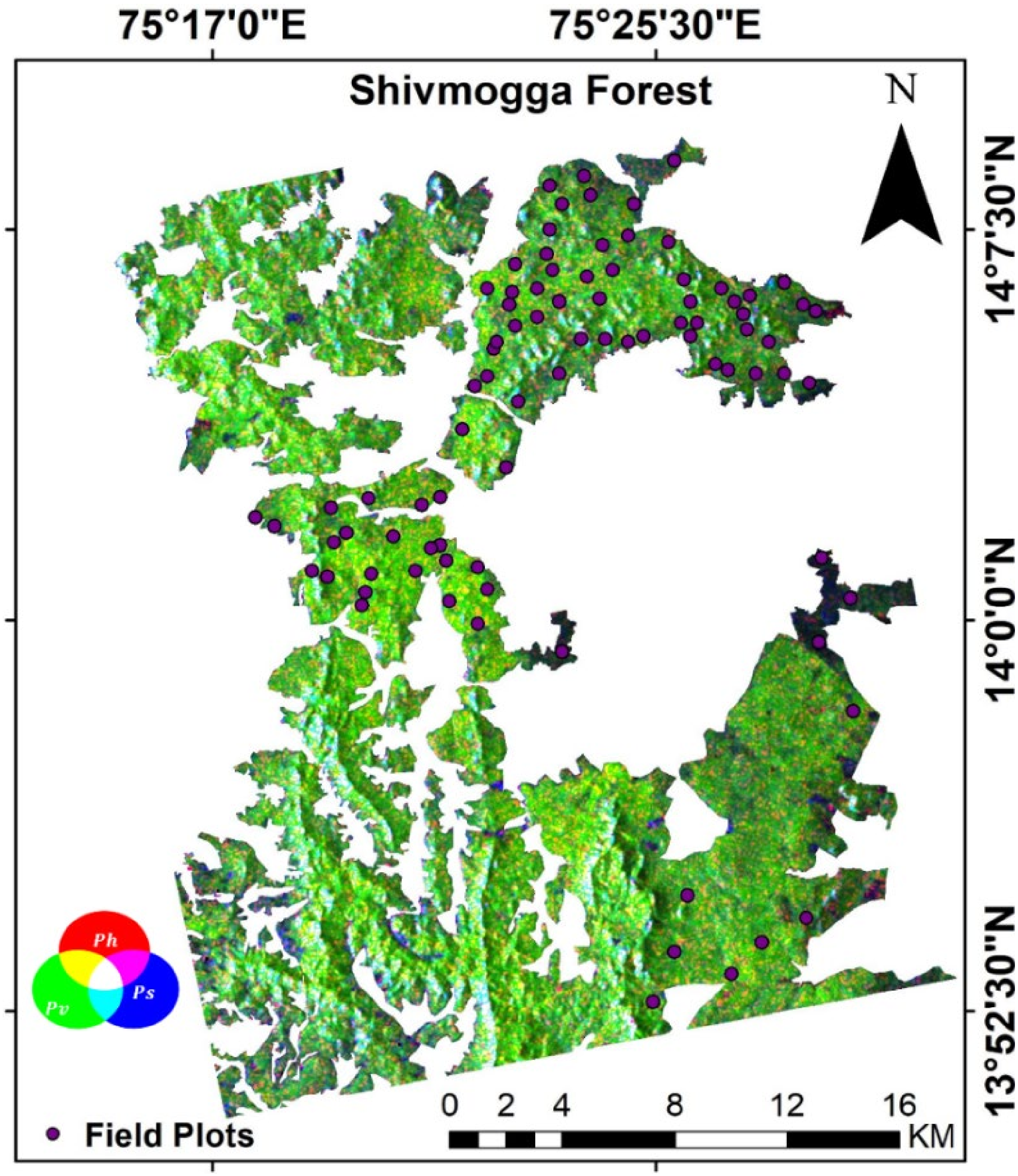

Figure 4.1 Test site: The Shivamogga (Karnataka)

4.2.2 Datasets

4.2.2.1 Field Data

To collect field data from the test site, field campaigns were conducted in 2019 and 2020 during the dry season, and in situ measurements were obtained. In total, 88 observation plots in Shivamogga forest, each 31.6 × 31.6 m in size, were used for the measurement of forest parameters (Table 4.1). In each sample plot, tree height and tree circumference at breast height (CBH) were measured. Forest height and the biomass of trees with CBH > 10 cm were considered. This field site is a natural forest containing diverse tree species. The dominant tree species in the field plots are teak (*Tectona grandis*), jambe (*Xylio xylocarpa*), eucalyptus (*Eucalyptus grandis*), dindega (*Anogeissus latifolia*), acacia (*Acacia auriculiformis*), mathi (*Terminalia tomentosa*), mitli (*Streblus asper*), nandi (*Lagerstroemia lanceolata*), and honalu (*Terminalia paniculata*). Tree species-specific volumetric equations developed by the Forest Survey of India (1996) were used to calculate field biomass (Forest Survey of India, 1996).

Table 4.1 Details of field data collection

Forest Site	**Max AGB (Mg/ha)**	**Min AGB (Mg/ha)**	**Mean AGB (Mg/ha)**	**Mean Stand Height (m)**
Shivamogga	319.58	15.24	117.97	15.32

4.2.2.2 Satellite Data

The Advanced Land Observing Satellite-2 (ALOS-2) dataset is provided by the Phased Array type L-band Synthetic Aperture Radar-2 (PALSAR-2) instrument, which offers enhanced capabilities over its predecessor (Arikawa et al., 2010). The Advanced Land Observing Satellite-2 (ALOS-2) dataset has been utilized extensively for forest AGB estimation (Hayashi et al., 2019; Tadono et al., 2019; Zhang et al., 2023). ALOS-2/PALSAR-2 datasets were acquired for both test sites. Fully polarimetric L-band PolSAR acquisitions from ALOS-2/PALSAR-2 were used in a single-look complex format, enabling precise polarimetric model-based decomposition (Table 4.2).

Table 4.2 Acquisition of the PolSAR datasets

Forest Site	Satellite/Sensor	Date of Acquisition	Polarization	Off-nadir Angle
Shivamogga	ALOS-2/PALSAR-2	2016-05-07	Quad-Polarization	28.4^0
	Radarsat-2	2019-03-08	Quad-Polarization	35.3^0

RADARSAT-2, an advanced C-band SAR satellite launched by the Canadian Space Agency in 2007, provides critical capabilities for forest monitoring, environmental management, and disaster response through its all-weather and day-and-night observation capabilities. RADARSAT-2 provides full polarimetric (quad-pol) SAR data, capturing information in four polarization channels: HH (horizontal transmit, horizontal receive), HV (horizontal transmit, vertical receive), VH (vertical transmit, horizontal receive), and VV (vertical transmit, vertical receive) (MDA, 2020). This quad-polarimetric capability allows for detailed characterization of scattering mechanisms and thus is highly effective in complex environmental applications such as forest disturbance detection, biomass estimation, wetland monitoring, and land cover classification.

4.2.2.3 GEDI Data

The Global Ecosystem Dynamics Investigation (GEDI) mission, launched by NASA in 2018, provides highly detailed, spaceborne LiDAR data aimed at assessing forest structure and biomass worldwide. Mounted on the International Space Station, GEDI collects three-dimensional measurements of forest canopy height, vertical structure, and AGB with unprecedented accuracy. This mission uses full-waveform LiDAR technology to capture the vertical distribution of plant material and canopy structure, which is invaluable for applications such as carbon stock estimation, biodiversity studies, and climate modeling (Dubayah et al., 2020).

GEDI data have proven essential to large-scale environmental research, providing insights that are complementary to those derived from traditional optical and SAR data sources. GEDI's ability to penetrate dense canopies and retrieve detailed structural information makes it particularly useful in tropical and subtropical forests, where such data have historically been sparse (Duncanson et al., 2022). Integrating GEDI data with other remote sensing datasets provides researchers with more accurate forest biomass estimates and better resolution of ecological changes across spatial and temporal scales. GEDI data were collected for the study area.

4.3 Methodology

4.3.1 Radar-scattering Matrix

The calibrated scattering matrix [*S*] for this study was generated using ALOS-2/PALSAR-2 and RADARSAT-2 data following Equation (1)

$$[S] = k \begin{bmatrix} S_{HH} & S_{HV} \\ S_{VH} & S_{VV} \end{bmatrix}, \tag{4.1}$$

where k is the calibration factor.

A second-order coherency matrix was derived by combining [*S*] with Pauli basis matrices through spatial ensemble averaging $\langle \ldots \rangle$, (i.e., multi-looking) in the azimuth and range directions of ALOS-2/PALSAR-2 and 4×6 RADARSAT-2. This averaging was performed using a 3 × 7 window (range × azimuth) to mitigate speckle noise. The resulting spatially averaged coherency matrix is expressed as:

$$\langle [T] \rangle = \langle k k^{\dagger} \rangle = \begin{bmatrix} \langle |k_1|^2 \rangle & \langle k_1 k_2{}^* \rangle & \langle k_1 k_3{}^* \rangle \\ \langle k_2 k_1{}^* \rangle & \langle |k_2|^2 \rangle & \langle k_2 k_3{}^* \rangle \\ \langle k_3 k_1{}^* \rangle & \langle k_3 k_2{}^* \rangle & \langle |k_3|^2 \rangle \end{bmatrix} = \begin{bmatrix} T_{11} & T_{12} & T_{13} \\ T_{21} & T_{22} & T_{23} \\ T_{31} & T_{32} & T_{33} \end{bmatrix} \tag{4.2}$$

where * denotes the complex conjugate and † represents the conjugate transpose. The Pauli vector k is expressed as:

$$k = \frac{1}{\sqrt{2}} \begin{bmatrix} S_{HH} + S_{VV} \\ S_{HH} - S_{VV} \\ 2S_{HV} \end{bmatrix} = \begin{bmatrix} k_1 \\ k_2 \\ k_3 \end{bmatrix}, \tag{4.3}$$

To generate more realistic SAR data, terrain correction using a 30-m Shuttle Radar Topography Mission digital elevation model was applied to address issues such as foreshortening in mountainous regions. This correction ensured accurate biomass calculation for each pixel that reflects actual field conditions. The SAR data were assumed to correspond to field surveys conducted in mature forests unaffected by human activities during the 4-year gap between data acquisition and field observation

4.3.2. The 7SD Model

In heterogeneous forests, all PolSAR relative phase information and parameters may be important; therefore, the reflection-symmetry-based polarimetric scattering decomposition model may not be appropriate. Several model-based scattering power decomposition approaches have been reported (Antropov et al., 2011; Freeman et al., 1998; Han et al., 2022; Singh & Yamaguchi, 2018; Van Zyl et al., 2011; H. Wang et al., 2019; Yamaguchi et al., 2005b). The most recent 7SD model is well suited to cases with scattering from compound structures in forest vegetation created by the combination of several dipoles, as 7SD expresses the maximum number of compound scattering components (Singh et al., 2019). 7SD was employed in this study. This technique is designed to handle complex forest structures by representing multiple scattering mechanisms (Singh et al., 2019). This model-based decomposition method is particularly effective for forests with heterogeneous vegetation, where compound scattering arises from a combination of dipoles and oriented dihedral structures (Munro, 2011).

$$[\boldsymbol{T}] = P_s\,[T]_{\mathrm{s}} + P_d\,[T]_{\mathrm{d}} + \begin{cases} P_v[T]_{vol}^{dipole} \\ P_v[T]_{vol}^{dihedral} \end{cases} + P_h[T]_{\mathrm{h}} + P_{od}[T]_{od} + P_{cd-oqw}[T]_{cd-oqw} + P_{md}[T]_{md} \tag{4.4}$$

$$= \frac{P_s}{1+|\beta|^2}\begin{bmatrix} 1 & \beta^* & 0 \\ \beta & |\beta|^2 & 0 \\ 0 & 0 & 0 \end{bmatrix} + \frac{P_d}{1+|\alpha|^2}\begin{bmatrix} |\alpha|^2 & \alpha & 0 \\ \alpha^* & 1 & 0 \\ 0 & 0 & 0 \end{bmatrix}$$

$$+ P_v \left\{ \begin{array}{l} \frac{1}{4}\begin{bmatrix} 2 & 0 & 0 \\ 0 & 1 & 0 \\ 0 & 0 & 1 \end{bmatrix};\, uniform\ distribution \\ \frac{1}{30}\begin{bmatrix} 15 & -5 & 0 \\ -5 & 7 & 0 \\ 0 & 0 & 8 \end{bmatrix};\, cosine\ distribution \\ \frac{1}{30}\begin{bmatrix} 15 & 5 & 0 \\ 5 & 7 & 0 \\ 0 & 0 & 8 \end{bmatrix};\, sine\ distribution \\ \frac{1}{15}\begin{bmatrix} 0 & 0 & 0 \\ 0 & 7 & 0 \\ 0 & 0 & 8 \end{bmatrix};\, oriented\ dihedral \end{array} \right\} + \frac{P_h}{2}\begin{bmatrix} 0 & 0 & 0 \\ 0 & 1 & \pm j \\ 0 & \mp j & -1 \end{bmatrix}$$

$$+ \frac{P_{od}}{2}\begin{bmatrix} 1 & 0 & \pm 1 \\ 0 & 0 & 0 \\ \pm 1 & 0 & 1 \end{bmatrix} + \frac{P_{cd-oqw}}{2}\begin{bmatrix} 1 & 0 & \pm j \\ 0 & 0 & 0 \\ \mp j & 0 & 1 \end{bmatrix} + \frac{P_{md}}{2}\begin{bmatrix} 0 & 0 & 0 \\ 0 & 1 & \pm 1 \\ 0 & \pm 1 & 1 \end{bmatrix}$$

The integration of these scattering components enables more nuanced reproduction of forest structure, especially in heterogeneous environments where multiple scattering processes coexist. The 7SD model, which captures compound and mixed scattering mechanisms, offers enhanced accuracy compared to traditional decomposition frameworks, making it particularly useful for forest biomass estimation. This model reflects a variety of physical characteristics, including surface roughness, canopy structure, and ground–trunk interactions, enabling detailed interpretation of forest properties.

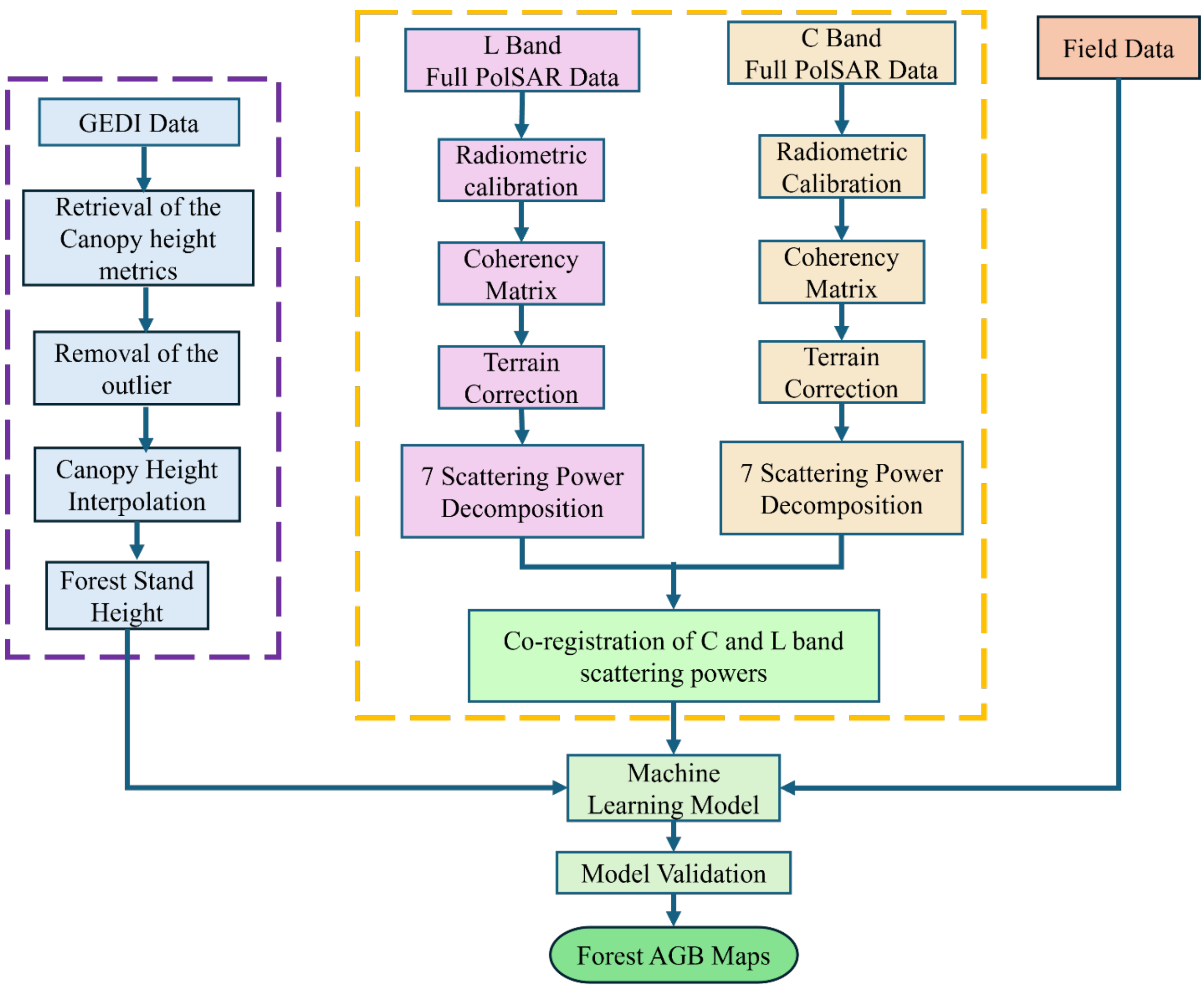

Figure 4.2 Flow chart of the research methodology

Forests surveyed were assumed to be in a mature state and unaffected by human interventions during the 4-year gap between field data collection and SAR data acquisition. This assumption ensured that the extracted scattering powers were closely aligned with ground conditions, thereby providing reliable input for biomass estimation models. The GEDI Level-2B elevation and canopy height products were processed using the rGEDI package in R. Canopy height parameters were extracted from the H5 file and converted into a vector file (ESRI shapefile format) for further analysis. Space-borne LiDAR acquisitions contain data outliers caused by many factors such as undulating topography, sunlight-induced noisy photon returns, canopy gaps due to selective logging or disturbance, and leaf-fall. A generic filtering method is employed in this study to remove outliers from both spaceborne LiDAR platforms. This filtering process is described below:

1. LiDAR footprints with a quality flag (for GEDI) of zero were filtered out.

2. Based on analysis of ground-truth samples, LiDAR footprints with canopy heights < 5 m and > 40 m were removed.

Geostatistics provides advanced interpolation techniques for the prediction of unknown values while accounting for the spatial characteristics of the study area. Given the spatially auto-correlated nature of forests (Duncanson et al., 2020), Kriging-based interpolation was employed to estimate canopy height from the LiDAR footprints. Kriging is a widely used spatial modeling technique that provides optimal and unbiased estimates at unsampled locations by assigning weights to sampled points, which are determined by the spatial dependence structure represented by a semi-variogram. This method prioritizes nearby samples, as they are more likely to have values similar to the point of interest (Curran & Atkinson, 1998). In this study, simple Kriging was implemented, considering the dense and evenly distributed LiDAR footprint across the study area. In contrast to multi-variate geostatistical models, simple Kriging assumes that the mean value m of the regionalized variable **Z** is constant across the domain D. The value of m is calculated as the average of observed data and used as prior data in the estimator. The simple Kriging estimator at an unsampled location can be mathematically expressed as shown in Equation 5 (Erdogan Erten et al., 2022):

$$z^*_{\mathrm{sk}}(\vec{u}_0) - m = \sum_{i=1}^{n} \lambda_i^{sk}(\vec{u})[z(\vec{u}_i) - m], \forall \vec{u}, \vec{u}_0, \vec{u}_i \in D \tag{4.5}$$

Where $z^*_{sk}(\vec{u}_0)$ represents the interpolated value at location $\vec{u}_0$ and $\lambda_i^{sk}(\vec{u})$denotes the weight assigned to each observation $z(\vec{u}_i)$.

GEDI canopy height data were co-registered with scattering powers derived from both L-band and C-band SAR data, enabling the development of a random forest machine learning model to predict forest biomass. Between the two SAR frequencies, the L-band scattering power exhibited a stronger correlation with field-measured biomass than the C band, highlighting the L band's enhanced sensitivity to forest structure and biomass. However, the strongest correlations were achieved when combining L-band and C-band scattering powers, indicating that multi-frequency SAR data capture complementary information about forest characteristics. Optimal results were obtained through the integration of multi-frequency SAR data with GEDI canopy height metrics, showing the potential of fused datasets to enhance the accuracy of biomass estimation. This multi-sensor approach leverages vertical information from GEDI and structural insights from SAR backscatter, providing a robust framework for precise and reliable forest biomass prediction.

4.4 Results and Discussion

4.4.1 Results

Visual interpretation of GEDI footprints revealed that several footprints collected over dense forest compartments showed unexpectedly low canopy height values (< 5 m). This anomaly is likely due to the presence of large canopy gaps caused by abscission, a natural phenological process in which leaves are seasonally shed. To address this issue, only GEDI footprints with the RH98 metric (indicating the height below which 98% of the energy return is observed) were used as reference data for further analysis. During variable selection and regression analysis, all relative height metrics (RH0 to RH100) were initially included to determine the variables contributing most significantly to accurate biomass estimation. Sensitivity analysis was conducted for the 7SD scattering powers derived from L-band and C-band SAR data (Merchant et al., 2017; Varghese et al., 2016a; X. Zhang et al., 2015) (Figure 4.3). This analysis showed that the interaction between SAR backscatter and forest structure varied significantly between the two bands. L-band scattering was dominated by volume scattering, indicating a strong response to the internal structure of the forest, including trunks, branches, and canopies. In contrast, C-band scattering exhibited more compound scattering, reflecting interactions at fine scales, such as the canopy surface and ground–trunk interfaces.

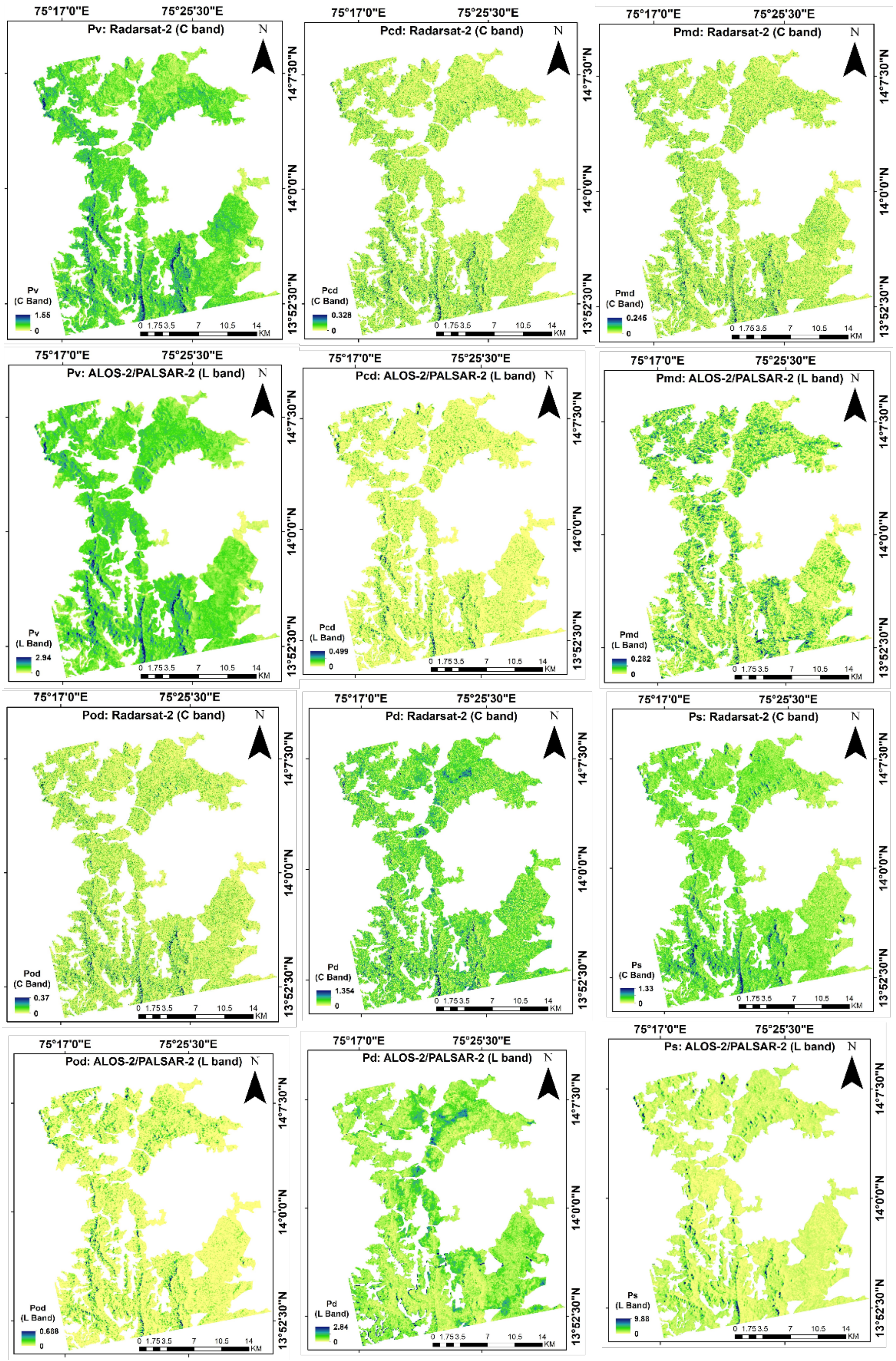

Figure 4.3 Maps of individual scattering powers from L-band and C-band observations across Shivamogga used to visualize their spatial variations.

The dominance of L-band volume scattering is attributed to the ability of longer wavelengths to penetrate dense canopies and interact with the forest interior, thereby providing robust returns from thick forest layers. Forests with high biomass and canopy density generate more volume dispersion in the L band due to the presence of few canopy gaps, which reduces signal penetration to the ground layer. In contrast, C-band signals, which are shorter in wavelength, interact more with surface-level structures and canopy elements, leading to increased compound scattering. These findings emphasize the complementary nature of L-band and C-band SAR data, with L-band data capturing deep structural features and C-band data providing insights into fine surface-level scattering processes.

Compound scattering arises from interactions of branches and other complex forest structures with the L-band signal, thus capturing the complex geometry of the forest canopy. However, spatial variability in surface, volume, and double-bounce scattering was notable in the Shivamogga forest area (Figure 4.3). This variability reflects the heterogeneous nature of forest structure across regions. The differences in compound scattering powers, including helix, mixed dipole, oriented dipole, and compound dipole components, highlighted the forest's structural complexity and spatial heterogeneity. The variation in compound scattering was closely associated with volume distribution over the ground, canopy density, and canopy gaps. Forest regions with higher canopy density and fewer gaps exhibited stronger volume scattering due to reduced signal penetration to the ground layer. In contrast, areas with larger canopy gaps or thinner canopy layers allowed for more interaction at the ground–trunk interface, influencing double-bounce and surface scattering responses. The diversity of scattering mechanisms across the forest range underscores the importance of multi-component decomposition models, such as the 7SD framework, to capturing the full spectrum of forest structures and dynamics. This spatial variability in scattering power provides valuable insights into forest health, biomass distribution, and canopy conditions, enabling more precise forest monitoring and management.

The results demonstrate that L-band SAR data provide higher estimation accuracy for forest AGB compared to C-band data, which is consistent with findings obtained in other tropical forest regions (Jha et al., 2010). This difference arises from the varying interactions between the two SAR frequencies in different parts of the forest. Due to its high frequency, the C band primarily interacts with leaves and tertiary branches, while the L band penetrates deeper into the forest canopy, interacting with secondary branches and tree trunks (Englhart et al., 2011; Le Toan et al., 1992; Ranson & Guoqing Sun, 1994). However, canopy opacity, stem density, and understory vegetation can reduce SAR sensitivity by saturating the backscattered signal (Joshi et al., 2017). Despite the high species diversity of the study area, with 66 tree species of varying canopy heights, which would typically reduce backscatter sensitivity, the abscission (leaf-fall) season during SAR acquisition in combination with dry climatic conditions resulted in low canopy density and minimal understory vegetation. This condition enhanced the accuracy of SAR data and improved the sensitivity of forest biomass estimation.

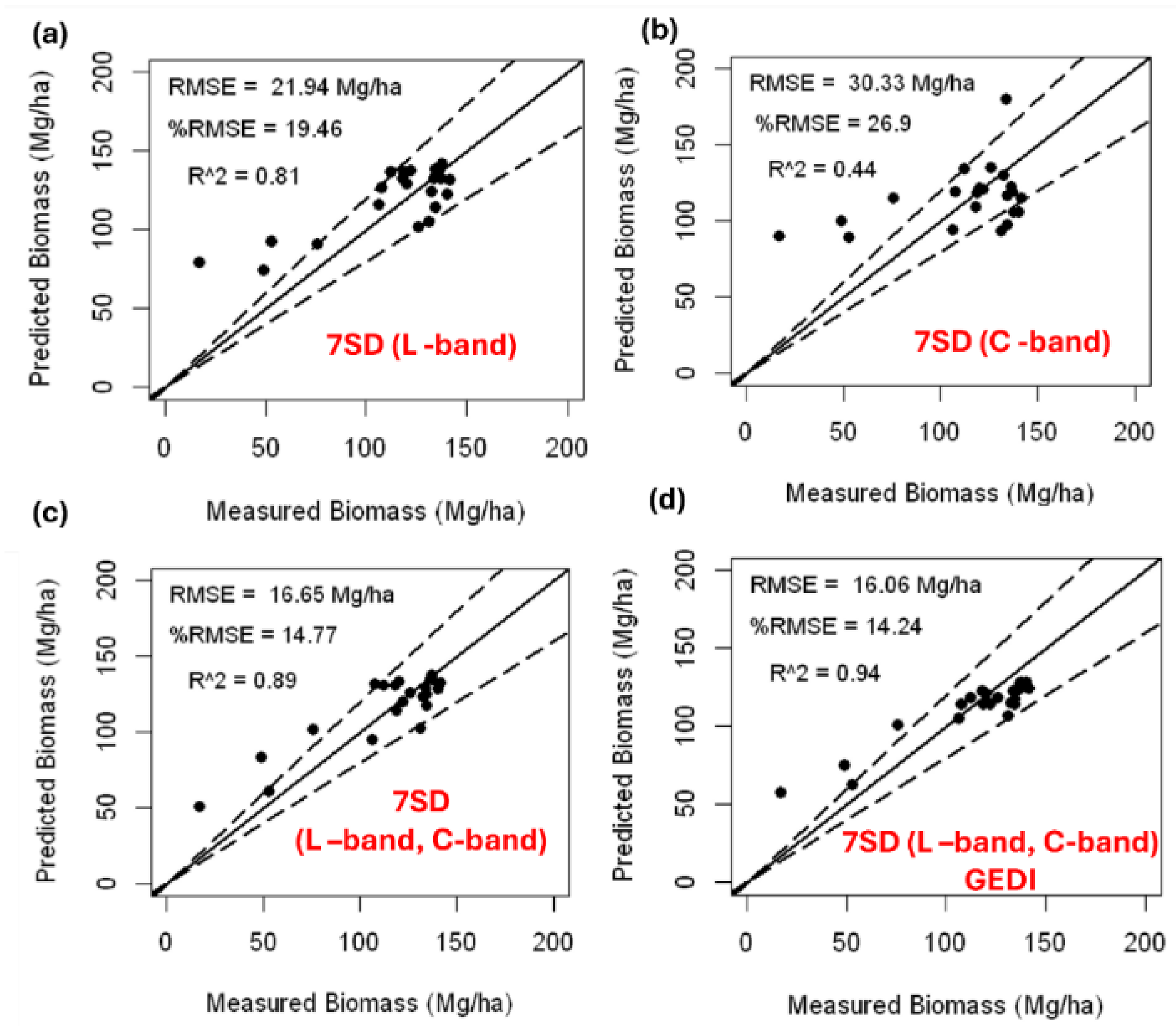

Figure 4.4 Validation of the forest AGB estimation model for the (a) L band (b) C band (c) L and C bands (d) L band, C- band, and GEDI

This study employed the scattering power derived from single-frequency SAR data in the C band (RADARSAT-2) and L band (ALOS-2/PALSAR-2) as predictor variables for biomass retrieval. A random forest regression (RFR) model was developed with 500 decision trees (nTree) and out-of-bag (OOB) error to evaluate the model performance. The OOB error stabilized after 200 trees, leading to a fine-tuned nTree value of 200. The biomass model was trained on 75% of the dataset, whereas the remaining 25% was used for validation. The L-band model exhibited better performance, yielding a relative root mean squared error (%RMSE) of 19.46%, compared with the C-band model, with %RMSE of 26.90% (Figure 4.4).

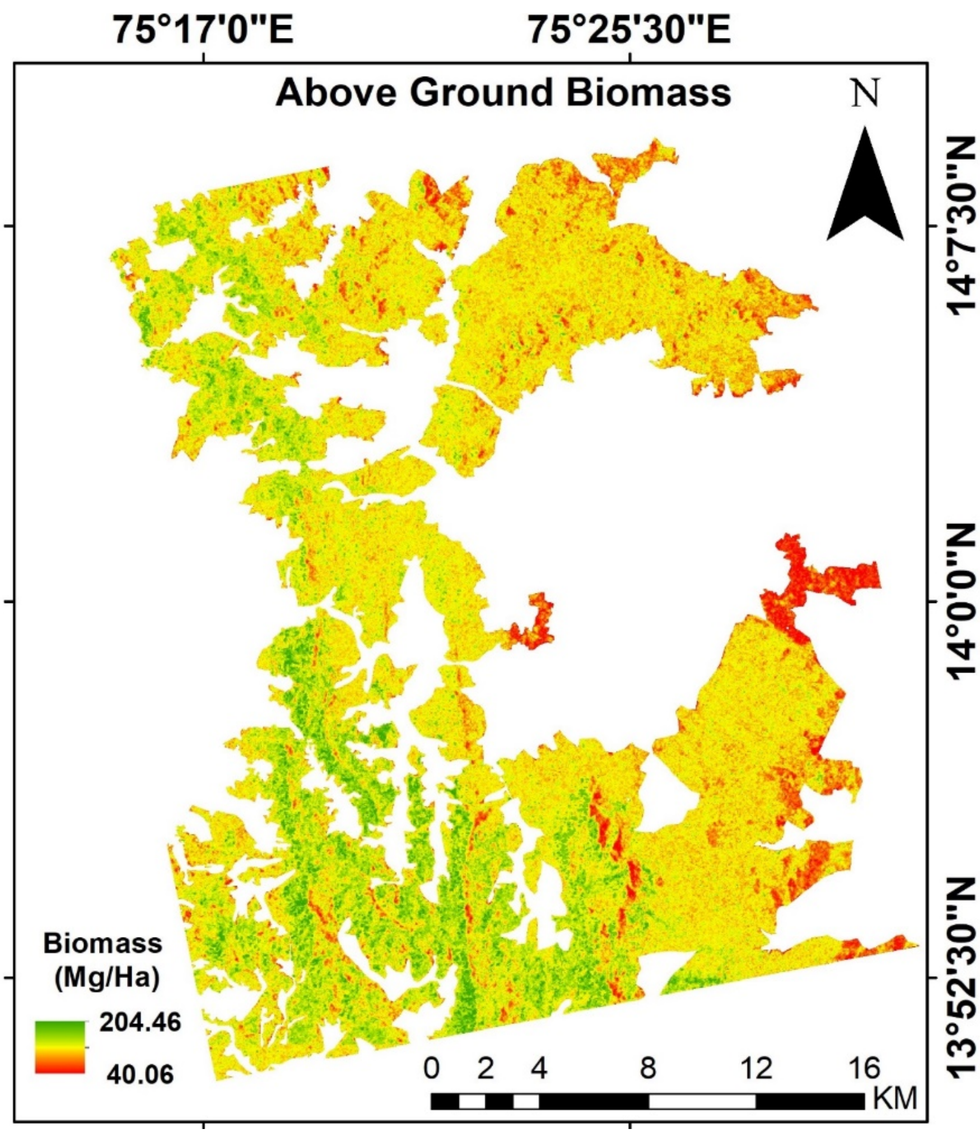

Figure 4.5 Spatial distribution of AGB estimated using the best model

Forest AGB estimated using single-frequency SAR data exhibited superior performance with L-band SAR data compared with C-band SAR data. This difference can be attributed to the greater canopy penetration capability of the L-band signal, which interacts with secondary branches and the main trunk, where the majority of the forest biomass is concentrated. In contrast, C-band SAR primarily interacts with secondary and tertiary branches. The C-band signal tends to saturate as canopy density increases, making it less effective for biomass retrieval in dense forests. Previous studies (Cartus & Santoro, 2019; Englhart et al., 2011) have shown that combining low- and high-frequency SAR data improves biomass estimation by capturing a broader range of forest components, including leaves, tertiary branches, secondary branches, and the main trunk. In this study, the integration of L-band and C-band SAR data significantly enhanced the accuracy of biomass retrieval (4.4).

To further refine the biomass estimates, the interpolated GEDI LiDAR canopy height raster was co-registered with multi-frequency SAR data, aligning the raster values with field measurements. An RFR algorithm was trained using 75% of the co-located data, while the remaining 25% was reserved for model validation. Variable importance analysis indicated that the canopy height layer was the most influential predictor, followed by the 7SD scattering power derived from L-band SAR and the 7SD power from C-band SAR. This finding emphasizes the synergy between canopy height and multi-frequency SAR backscatter, as the combination of LiDAR height data and multi-frequency SAR components enables more comprehensive representation of forest structure, improving biomass estimation accuracy.

The inclusion of canopy height data from GEDI in the random forest model significantly enhanced AGB estimation for both single-frequency and multi-frequency SAR-based methods. The modeled biomass was validated using ground-truth testing data, and %RMSE was calculated. Regarding the single-frequency SAR and LiDAR combinations, L-band data outperformed C-band data. The integration of the GEDI canopy height with multi-frequency SAR data further improved biomass estimation, resulting in %RMSE of 14.24% (Figure 4.4). However, GEDI height contributed less to improving accuracy when used with the 7SD scattering power derived from multi-frequency SAR data compared with models using multi-frequency backscattering data. Specifically, the combination of GEDI height and multi-frequency SAR produced %RMSE of 14.24%, which is only marginally better than the 14.77% achieved with the multi-frequency SAR model alone. The best-performing model, with %RMSE of 14.24%, was used to generate a forest AGB map, providing the most accurate spatial representation of biomass in the study area (Figure 4.5). This map highlights the value of integrating GEDI height and multi-frequency SAR data, demonstrating that synergistic use of LiDAR and SAR can provide reliable and detailed estimates of forest biomass, which are crucial for effective forest monitoring and management.

4.4.2 Discussion

This study demonstrated that the integration of GEDI LiDAR canopy height data with multi-frequency SAR scattering powers from L-band (ALOS-2/PALSAR-2) and C-band (RADARSAT-2) datasets captured the structural complexity of tropical forests, enhancing AGB estimation. Integrating L- and C-band SAR data improved biomass estimation accuracy, reducing %RMSE to 14.77%, compared to 19.46% for L-band SAR alone and 26.90% for C-band SAR alone. These results revealed distinct interactions of L-band and C-band SAR signals with forest components. L-band SAR, with its longer wavelength, was more responsive to internal forest structures such as trunks and primary branches, while C-band SAR captured surface-level details, including canopy surfaces and ground–trunk interfaces. These findings are consistent with previous research (Englhart et al., 2011; Le Toan et al., 1992), reaffirming the complementary nature of the two frequencies in representing different forest features. Result demonstrates that the multi-frequency SAR-based model effectively addresses the limitations of single-frequency models in heterogeneous tropical forests compared to existing methods (Cartus et al., 2017; Cartus & Santoro, 2019; W. Huang et al., 2015a; Jha et al., 2010; Musthafa & Singh, 2022b).

Moreover, the combination of GEDI LiDAR canopy height data with multi-frequency SAR measurements further enhanced accuracy, achieving a %RMSE of 14.24%. Canopy height emerged as the most influential predictor in the RFR model, followed by L- and C-band scattering powers. While LiDAR height metrics improved biomass estimation, much of the structural information was already captured by the detailed decomposition of SAR data, demonstrating its effectiveness in representing forest structure. This scalable approach enables detailed spatial representation of AGB, producing high-resolution biomass maps that offer insights into forest health, degradation, and carbon stocks.

Despite these improvements, challenges of saturation effects remain in the L-band SAR signal in high-biomass areas (>150 Mg/ha) reduce signal penetration, limiting accuracy. Future studies could incorporate data from ESA's BIOMASS mission (P-band SAR) or the upcoming L- and S-band NISAR mission to capture additional structural information. Additionally, temporal data from GEDI and SAR sensors could help monitor seasonal biomass changes, providing deeper insights into forest dynamics and phenological cycles for improved biomass estimation models.

4.5 Conclusion

This study demonstrates that the inclusion of forest canopy height with scattering powers from single- or multi-frequency SAR enhances the accuracy of forest biomass prediction. The findings indicated that GEDI canopy height had less impact on biomass estimation accuracy when combined with multi-frequency SAR scattering powers than when integrated with multi-frequency SAR backscatter data, as reported in previous studies. However, the incorporation of canopy height along with all channels of the L band and C band reduced %RMSE from 14.77% to 14.24%, demonstrating meaningful improvement in the biomass model's performance. The combination of long-wavelength L-band and C-band SAR with GEDI data yielded better results, achieving %RMSE below 15%, which is within the acceptable error range for biomass estimation efforts such as those of the NASA–Indian Space Research Organization (ISRO) SAR (NISAR) mission. This finding highlights the value of multi-sensor integration, with the structural insights obtained from L-band and C-band SAR complementing the vertical canopy information provided by GEDI, resulting in a robust and accurate forest biomass estimation framework.

Chapter 5 : Development of the Four-component Scattering Power Decomposition Model for Dual polarization SAR Data

5.1 Introduction

Synthetic Aperture Radar (SAR) has improved Earth observation by providing cloud-free and independent of sun illumination and high-resolution data. Full Polarimetry Synthetic Aperture Radar (Full-PolSAR) data can be used in different applications for detailed classification and environmental monitoring. The Full-PolSAR data contains both the co-polarized, i.e., HH and VV, as well as the cross-polarized, i.e., HV and VH backscatter information, respectively, which creates a scattering matrix that captures the complexity of target interactions with the radar signal providing detailed descriptions of scattering mechanisms. This improves the accuracy of the classification (S.-W. Chen et al., 2018; Maitra et al., 2013; Nord et al., 2009; X. Wang et al., 2019; R. Yang et al., 2021).

It is essential to decompose the scattering mechanisms from the PolSAR data to discriminate between surface, double-bounce, and volume scattering. Various model-based and eigenvalue-based scattering power decomposition techniques (An et al., 2010; Sato et al., 2012; Singh et al., 2019; Singh & Yamaguchi, 2018; Yamaguchi et al., 2005b, 2006) have been proposed to decompose the total scattering power into different components of scattering power related to different features on the Earth's surface. The scattering power derived from these decomposition techniques can be used for accurate classification and applications in deforestation detection (Avtar et al., 2012; Priyanka et al., 2023; Wiederkehr et al., 2020), biomass estimation, and change detection (Avtar et al., 2013; Hong et al., 2019; Rajat et al., 2024; Suab et al., 2024). Full-PolSAR data have complete scattering information, which leads to high accuracy in different applications, but the widespread utilization of full PolSAR data is limited due to sparse availability, technical complexities, and higher costs in data collection and processing. (Moreira et al., 2013). Such restrictions lead to limited spatial coverage and temporal resolution compared with single- or dual-polarization data (J. Deng et al., 2023; Schmullius & Evans, 1997), which limits the application of full-polarimetric SAR data in large-scale and time-sensitive monitoring applications (Schmullius & Evans, 1997).

In contrast, dual-polarization (dual-pol) SAR data, which captures only two polarization channels, either co-polarized or cross-polarized, is more widely accessible than full-polarimetric (full-pol) data from various SAR satellite missions. The increased availability and broader swath coverage of dual-pol data makes it advantageous for large-scale monitoring and time-series applications, especially in regions requiring frequent and extensive monitoring, such as tropical forests subject to rapid deforestation and degradation (Hansen et al., 2020). Recognizing the potential of dual-pol data (Sugimoto et al., 2022, 2023) has extended the scattering power decomposition algorithms to dual-pol data by developing a three-component scattering power decomposition, that is, volume scattering, ground scattering, and double-bounce scattering.

The main objective of this study was to create a new dual-pol four-component scattering power decomposition model (DP-4SD). This model uses dual-polarization SAR data to improve detection and classification, including classification of forest species and disturbance detection, ecology, and natural resource management applications. In the 4SD model, a new oriented dipole scattering component was developed to incorporate scattering from different orientations of the scattering objects, including but not limited to the forest canopy or oriented urban features that are not provided by a three-component scattering model in the dual-pol data. Including the oriented dipole scattering component provides a more nuanced representation of the scattering behavior in complex environments, mainly where volume scattering dominates, such as in forested areas, because the three scattering power decomposition models (3SD) overestimate the contribution of volume scattering, resulting in less accurate classification results. The 4SD model reduces the overestimation of volume scattering, thereby improving polarimetric information extraction accuracy and target classification. The oriented dipole (OD) scattering model was selected because it effectively represents the scattering behavior of various vegetation structures when analyzed using dual-polarization (dual-pol) data. The OD scattering power captures the predominant volume scattering mechanism in vegetation areas where the scatterers (such as tree branches and leaves) are randomly oriented. This is critical for distinguishing vegetation from other land cover types, as vegetation typically exhibits strong volume scattering due to the random orientation of dipoles within the canopy (Freeman & Durden, 1998).

While other models like compound dipole or mixed dipole scattering can also represent vegetation, but oriented dipole can be generated using dual-pol data, as it captures the dominant scattering mechanism without requiring the full complexity of full-pol data. In this study, oriented dipole provides a balance between accuracy and availability of the full PolSAR data in environments dominated by volume scattering, such as forests or agricultural areas. By developing this 4SD model, this study aims to bridge the gap between the limited availability of full-polarimetric SAR data and the need for advanced decomposition techniques to effectively analyze dual-pol data. The DP-4SD model can be applied to various applications, including forest monitoring, urban planning, and disaster management, where accurate and timely information is critical for decision making using SAR-based remote sensing technologies, contributing to improved environmental and resource management globally.

5.2 Test Sites and Data Used

5.2.1 Haldwani Forest

The Haldwani forest range is located in between $29°\ 00'$ N to $29°\ 15'$ N latitude and $79°15'$ E to $79°30'$ E longitude (Figure 5. 1) in the Uttarakhand state in the foothills of the lower Shiwaliks. The climate of the Haldwani Forest Range is typically subtropical, characterized by hot summers, mild winters, and a significant monsoon season. The elevation ranges from approximately 500 m (1,640 ft) above sea level in the lower areas to over 1,000 m (3,281 ft) in the higher regions near hills. It is a managed forest region with unique species distribution in well-delineated forest compartments.

In polarimetric synthetic aperture radar (PolSAR) analysis, creating an RGB composite image using the covariance matrix $[C_2]$elements $\langle|S_{VV}|^2\rangle$, $\langle|S_{VH}|^2\rangle$and the ratio $\langle|S_{VV}|^2\rangle/\langle|S_{VH}|^2\rangle$ is an effective way to visualize different scattering mechanisms and surface properties ($\langle . \rangle$ represents spatial ensemble avarageing) . Each of these elements captures specific backscattering characteristics in different polarization channels, providing valuable insights into land cover classification and environmental monitoring.

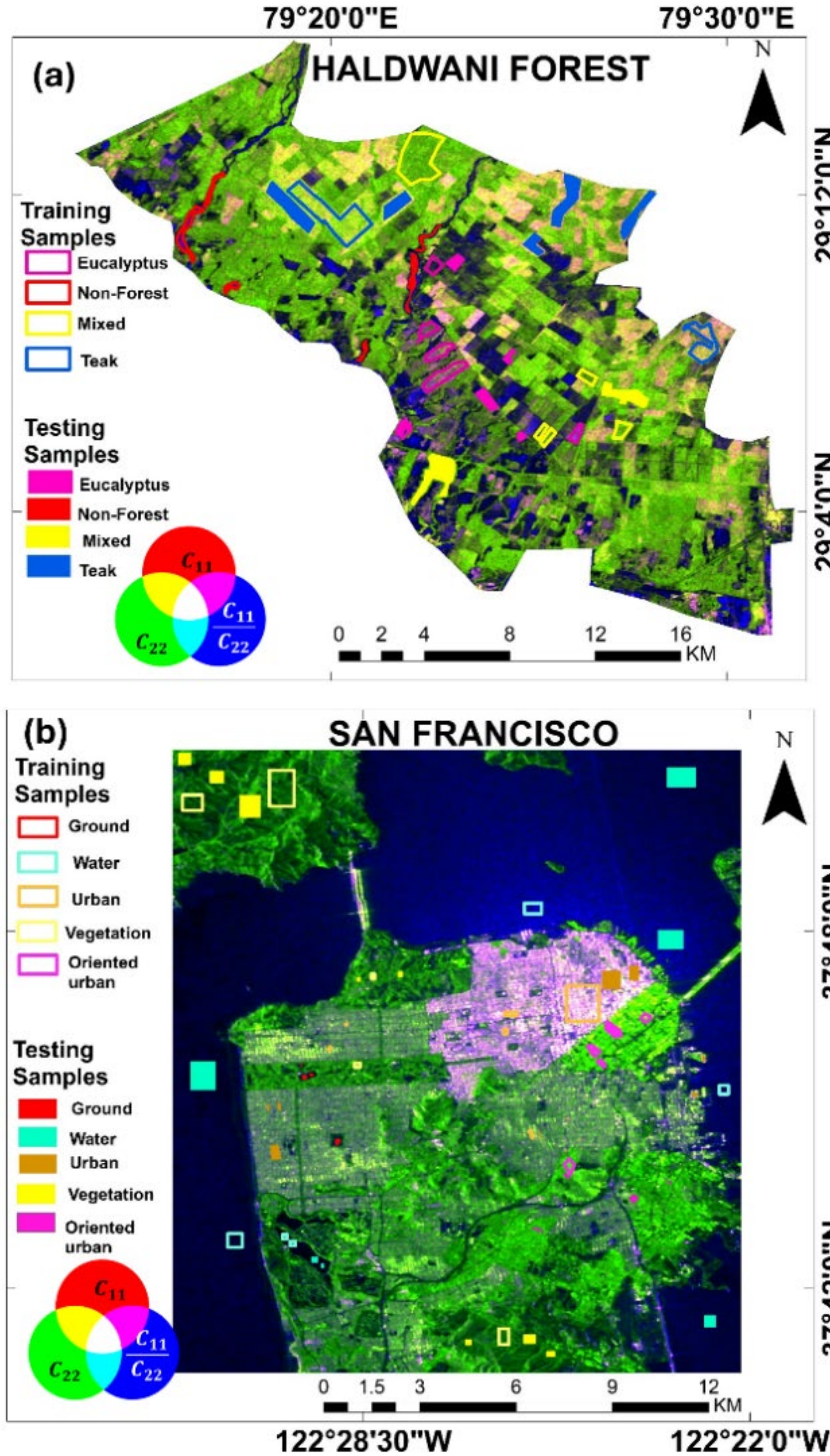

Figure 5.1 Test Sites (a) Haldwani Forest (b) San Francisco, $\langle|S_{VV}|^2\rangle$, $\langle|S_{VH}|^2\rangle$, and $\langle|S_{VV}|^2\rangle/\langle|S_{VH}|^2\rangle$ are the elements of the covariance matrix.

5.2.2 San Francisco

San Francisco, located on the western coast of the United States, is an urbanized region characterized by diverse land-use and land-cover (LULC) types, including urban areas, vegetation, water bodies, and infrastructure (Figure 5.1). As a study area, San Francisco offers a complex environment for classification analysis because of its varied topography and heterogeneous landscapes, including natural features such as hills, forests, and coastal regions, as well as dense urban structures. It has a Mediterranean-type climate, characterized by mild wet winters and warm dry summers, which supports high biological diversity.

5.2.3 Data Used

In this study, I utilized datasets from the Advanced Land Observation Satellite (ALOS), equipped with the Phased Array type L-band Synthetic Aperture Radar (PALSAR), and the Advanced Land Observing Satellite-2 (ALOS-2), which features the Phased Array type L-band Synthetic Aperture Radar-2 (PALSAR-2). PALSAR's ability to operate in multiple polarization modes enables detailed surface analysis, making it effective for applications such as deforestation monitoring and target classification (Hayashi et al., 2019; Tadono et al., 2019; H. Zhang et al., 2023). Datasets were acquired for both test sites as mentioned in Table 5.1.

Table 5.1 Details of the PolSAR datasets

Site	Satellite/Sensor	Date of Acquisition	Polarization
Haldwani	ALOS-2/PALSAR-2	2018-04-15	Dual-Polarization
San Francisco	ALOS/PALSAR	2010-05-07	Dual-Polarization

The ALOS-2/PALSAR-2 datasets were processed to generate $[C_2]$ using a multi-look window factor of 2 in the range direction and 5 in the azimuth direction. For ALOS/PALSAR, $[C_2]$ was generated with a multi-look window factor of 1 in the range direction and 5 in the azimuth direction. To enhance the accuracy of real-world representation, geometric distortions were addressed through terrain correction applied to the $[C_2]$. This process utilized a Shuttle Topography Radar Mission Digital Elevation Model (SRTM-DEM) with a 30 m posting resolution to compensate for any topographic-induced distortion.

5.3 Concept of Dual-Pol Model-based Decomposition

5.3.1. 2×2 Covariance Matrix

There are only two complex elements (S_{VV} and S_{VH} or S_{HH} and S_{HV}) in dual-polarization SAR measurements, the coherency matrix and Pauli scattering vector cannot be created using dual-polarization data. Based on the relationship between dual-polarization and full PolSAR data, we can summarize the polarimetric information of the 2×2 covariance matrix $\langle[C_2]\rangle$ ($\langle[C_H]\rangle$ or $\langle[C_V]\rangle$) by relating them to the full 3×3 scattering coherency matrix; as follows (Sugimoto et al., 2023):

$$k_V = \begin{bmatrix} S_{VV} \\ S_{VH} \end{bmatrix} = \frac{1}{\sqrt{2}} \begin{bmatrix} 1 & -1 & 0 \\ 0 & 0 & 1 \end{bmatrix} \begin{bmatrix} S_{HH} + S_{VV} \\ S_{HH} - S_{VV} \\ 2S_{HV} \end{bmatrix} \tag{5.1}$$

$$\langle[C_V]\rangle = \langle k_V k_V^{+} \rangle = \begin{bmatrix} \langle |S_{VV}|^2 \rangle & \langle S_{VV} S_{VH}^* \rangle \\ \langle S_{VV}^* S_{VH} \rangle & \langle |S_{VH}|^2 \rangle \end{bmatrix} = \begin{bmatrix} C_{11} & C_{12} \\ C_{21} & C_{22} \end{bmatrix} \tag{5.2}$$

$$k_H = \begin{bmatrix} S_{HH} \\ S_{HV} \end{bmatrix} = \frac{1}{2} \begin{bmatrix} 1 & 1 & 0 \\ 0 & 0 & 1 \end{bmatrix} \begin{bmatrix} S_{HH} + S_{VV} \\ S_{HH} - S_{VV} \\ 2S_{HV} \end{bmatrix} \tag{5.3}$$

$$\langle[C_H]\rangle = \langle k_H k_H^{+} \rangle = \begin{bmatrix} \langle |S_{HH}|^2 \rangle & \langle S_{HH} S_{HV}^* \rangle \\ \langle S_{HH}^* S_{HV} \rangle & \langle |S_{HV}|^2 \rangle \end{bmatrix} \tag{5.4}$$

Henceforth, I will denote $[C_H]$ and $[C_V]$, by the symbol $[C_2]$.

5.3.2 Dual-polarization Model-Based Scattering Power Decomposition

The established relationships were employed to extend the scattering power decomposition using dual-polarization data. Accordingly, a four-component scattering power model for dual-pol data has been developed to represent scattering in tropical forests: the volume scattering power, oriented dipole scattering power, helix scattering power, and surface scattering power as shown in Figure 2. A covariance matrix $\langle[C_2]\rangle$ obtained in dual-polarization (S_{VV} and S_{VH} or S_{HH} and S_{HV}) mode can be expanded into four scattering matrices as:

$$\langle[C_2]\rangle = P_g\langle[C_2]\rangle_g + P_v\langle[C_2]\rangle_v + P_h\langle[C_2]\rangle_h + P_{od}\langle[C_2]\rangle_{od} \tag{5.5}$$

In Equation (5), $\langle[C_2]\rangle_g$, $\langle[C_2]\rangle_v$, $\langle[C_2]\rangle_h$ and $\langle[C_2]\rangle_{od}$ are ground, volume, helix, and oriented dipole scattering power matrices, respectively. P_g, P_v, P_h and P_{od} are dual polarization-based ground, volume, helix and oriented dipole scattering powers, respectively.

The ground scattering power matrix can be expressed as

$$\langle[C_2]\rangle_g = \begin{bmatrix} 1 & 0 \\ 0 & 0 \end{bmatrix} \tag{5.6}$$

The covariance matrix for the volume scattering power is adopted by considering the uniform distribution of dipole structures in the vegetation area, as follows:

$$\langle[C_2]\rangle_v = \frac{1}{4}\begin{bmatrix} 3 & 0 \\ 0 & 1 \end{bmatrix} \tag{5.7}$$

The helix scattering model is able to account for imaginary part of the off-diagonal term in $\langle[C_V]\rangle$ or $\langle[C_H]\rangle$ (i.e., $S_{VV}S_{VH}^* \neq 0$ or $S_{HH}S_{HV}^* \neq 0$) [18]. Helix scattering can be produced by compound targets (Singh et al., 2013a), which generate circular polarization from all linear polarizations.

$$\langle[C_2]\rangle_h = \frac{1}{2}\begin{bmatrix} 1 & \pm j \\ \mp j & 1 \end{bmatrix} \tag{5.8}$$

When multiple targets exist within the same radar range, an oriented dipole matrix can be created through compound scattering phenomena. In the case of dual polarization, the oriented dipole scattering model accounts for real part of the off-diagonal term and can be depicted as

$$\langle[C_2]\rangle_{od} = \frac{1}{2}\begin{bmatrix} 1 & \pm 1 \\ \pm 1 & 1 \end{bmatrix} \tag{5.9}$$

From Equation (5) to (9), Equation (5) can be rewritten as

$$\langle[C_2]\rangle = P_g \begin{bmatrix}1 & 0\\ 0 & 0\end{bmatrix} + \frac{P_v}{4}\begin{bmatrix}3 & 0\\ 0 & 1\end{bmatrix} + \frac{P_h}{2}\begin{bmatrix}1 & \pm j\\ \mp j & 1\end{bmatrix} + \frac{P_{od}}{2}\begin{bmatrix}1 & \pm 1\\ \pm 1 & 1\end{bmatrix} \tag{5.10}$$

From (10), P_g, P_v, P_{od} and P_h can be computed as

$$\begin{aligned} \pm P_{od}^V \pm jP_h^V &= 2\,\mathrm{Re}\langle S_{VV}S_{VH}^*\rangle + \mathrm{j}\;2\mathrm{Im}\,\langle S_{VV}S_{VH}^*\rangle \\ P_{od}^V &= 2|Re\langle S_{VV}S_{VH}^*\rangle| \\ P_h^V &= 2|Im\langle S_{VV}S_{VH}^*\rangle| \end{aligned} \tag{5.11}$$

$$P_v^V = 2\langle |S_{VH}|^2\rangle - P_h^V - P_{od}^V \tag{5.12}$$

$$P_g^V = \langle |S_{VV}|^2\rangle - \frac{3}{4}P_v^V - \frac{1}{2}P_{od}^v - \frac{1}{2}P_h^V \tag{5.13}$$

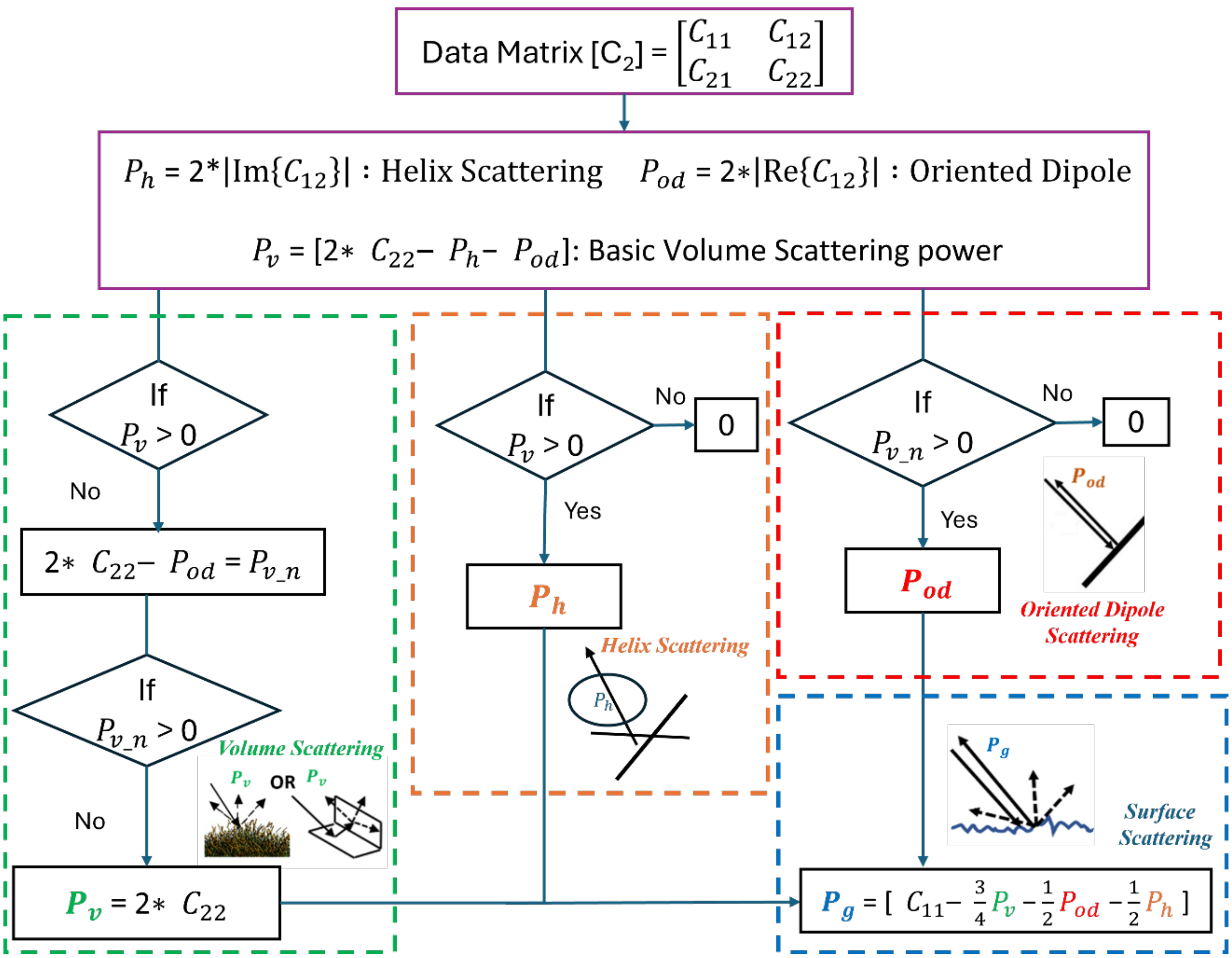

Figure 5.2 Implementation flowchart of the proposed 4SD algorithm

Based on Equations (5) to (10), the algorithm is constructed, which is applied to calculate the 4SD scattering powers namely ground (P_g), helix (P_h), volume (P_v), and oriented dipole (P_{od}). The flowchart of DP-4SD algorithm is illustrated in Figure 5.2 for implementing on dual polarimetric SAR data.

5.3.3 Classification

Various classification techniques, such as Maximum Likelihood, Support Vector Machine, and Knowledge-Based Decision Trees, have been extensively studied and applied (Maghsoudi et al., 2013; Mishra et al., 2019; Varghese et al., 2016b). However, the random forest (RF) classifier has proved efficient for classification of vegetation using SAR datasets in several studies (Du et al., 2015; Waske & Braun, 2009). Therefore, the supervised Random Forest classifier was employed on the scattering power image generated from 3SD and 4SD to evaluate the accuracy of both scattering power decomposition techniques in identifying and classifying different LULC classes. Comprehensive technical details and discussions on the use of RF in remote sensing can be found in (Breiman, 2001).

The Random Forest classifier is of ensemble machine learning, which incorporates numerous decision trees to have a more accurate and robust output. The RF classifier builds a "forest" of decision trees, training each tree on a random selection of the training data using a randomly picked set of features (Belgiu & Drăguţ, 2016). Random Forests classification Equation (14) introduced by (Breiman, 2001) is given below, which describes the process of constructing multiple decision trees and using them for classification by aggregating the outputs of all trees through majority voting.

$$\hat{y} = \text{mode}(T_1(x), T_2(x), \ldots\ldots\ldots\ldots\ldots\ldots\ldots \; Tn(x)) \tag{5.14}$$

Where:

$\hat{y}$ is the predicted class label for the input x.

$T1(x)$, $T2(x)$, …, $Tn(x)$ are the predictions from the individual decision trees in the forest.

n is the number of trees in the forest.

Mode $(\cdot)$ denotes the majority voting among the predictions of all trees

This study utilizes two reference data sets, a training set for classification purposes, and a testing set for post-classification validation for both sites. Both reference data sets were obtained using a random sampling method.

5.4 Results

This study used the dual polarimetric L-band SAR datasets acquired over the San Francisco and Haldwani Forest regions from both the Advanced Land Observation Satellite (ALOS/PALSAR) and Advanced Land Observation Satellite-2 (ALOS-2/PALSAR-2) for a comparative analysis between the proposed DP-4SD and the existing DP-3SD model. Each color represents specific scattering powers represented qualitatively: blue represents ground scattering, red represents oriented dipole scattering, orange represents helix scattering, and green represents volume scattering. These scattering powers were combined in RGB color-coded images to assist image interpretation, target classification, and identification. This visualization technique detects differences in scattering mechanisms, thereby enhancing the SAR data analysis.

5.4.1 Quantitative Analysis of the Scattering Powers of 3SD and 4SD

Four RoIs in RGB images of 4SD and 3SD, as shown in Figure 5.3 were selected based on different forest compositions in the Haldwani region: teak, eucalyptus, mixed forest, and non-forested (NF) areas. The scattering power statistics of both the existing 3-component scattering decomposition algorithm and the proposed 4-component scattering decomposition algorithm were estimated using selected area classes to observe the differences in the scattering mechanisms between the two algorithms.

While the 3SD model has only three components of scattering powers that lead to the overestimation of volume scattering, the 4SD model has a new scattering component of oriented dipole scattering to reduce this overestimation. The most important observation from the investigation in the Haldwani region is the consistent decrease in volume scattering in 4SD compared to that in 3SD in all types of forests. This decrease signifies a better decomposition of the scattering mechanisms, especially for the forested classes. Volume scattering in 4SD decreased from 23.4 to 19.7% in teak forest, from 12.3 to 8.6% in eucalyptus forest, from 53.3 to 47.8% in mixed forest, and from 11.6 to 5.4% in non-forested areas, as shown in Figure 5.4. To compensate for the reduced volume scattering, the oriented dipole scattering component contribution increased for all forest classes because the oriented dipole was generated by vegetation areas where tree branches were structured such that multiple scattering interactions of the radar signal occurred.

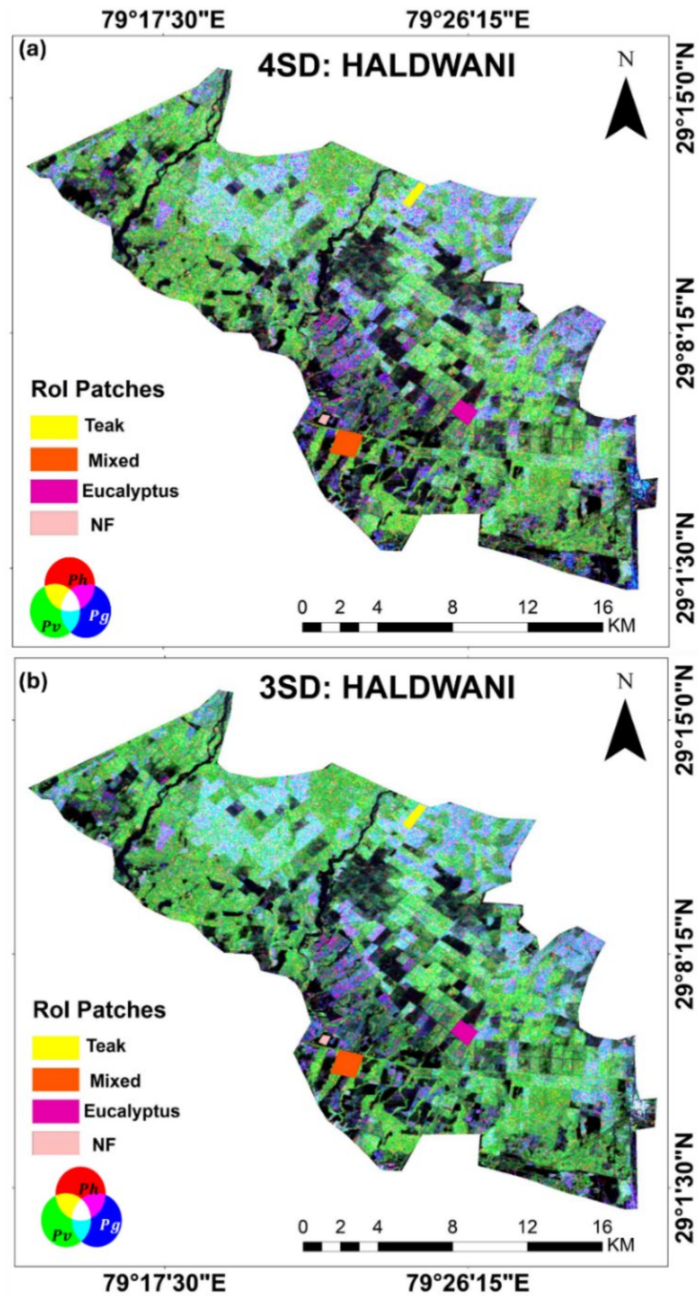

Figure 5.3 RGB images of (a) 4SD (b) 3SD for Haldwani with RoIs

Thus, it was shown that in forest types with complex canopy structures, such as radar, signals incident to objects backscattered not only from the surface but also from the branches, resulting in compound scattering. Furthermore, this result showed that the dominance of surface scattering over low and sparsely vegetated land cover areas was observed in the case of forest plantations. This implies that the 4SD model captures the variability within the scattering behavior for various forest types. This signifies that the 4SD model is better suited for land cover classification and forest monitoring because of its improved accuracy.

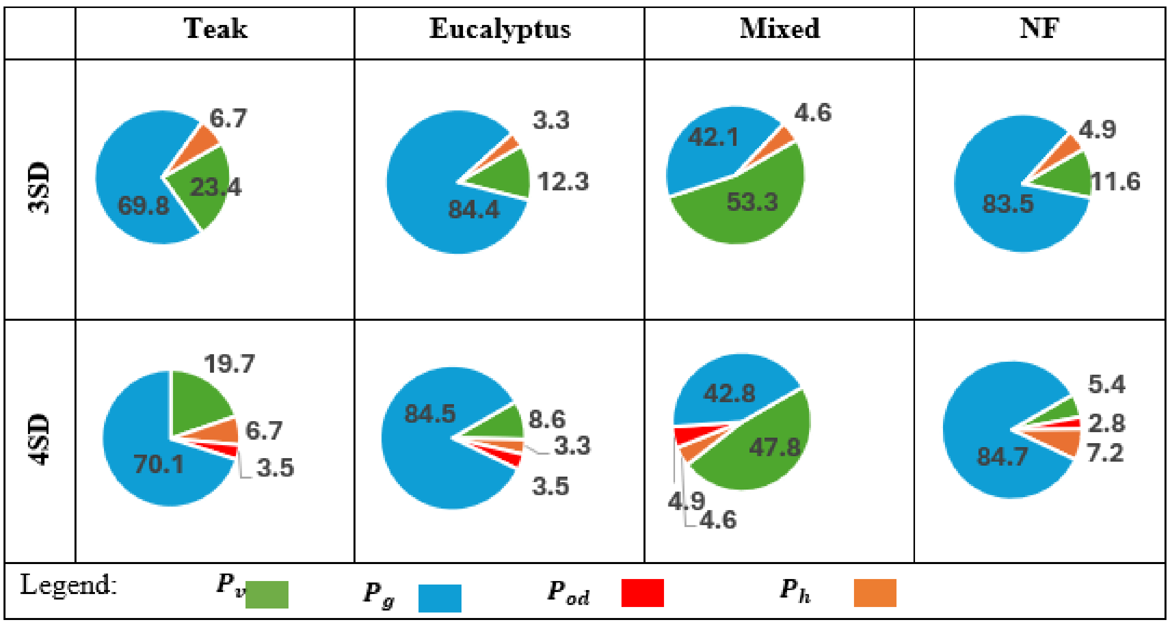

Figure 5.4 Model-based decompositions (3SD, 4SD) power statistics for Haldwani

These differences were more obvious in the case of San Francisco when comparing the 3SD and 4SD scattering decomposition models, (Figure 5.5), underlining the improvement in interpretation arising from the inclusion of an oriented dipole scattering component in the 4SD model for complex urban and natural landscapes. The 4SD model discriminated between volume scattering and oriented dipole scattering, enabling better discrimination between urban structures, water body features, and vegetation class.

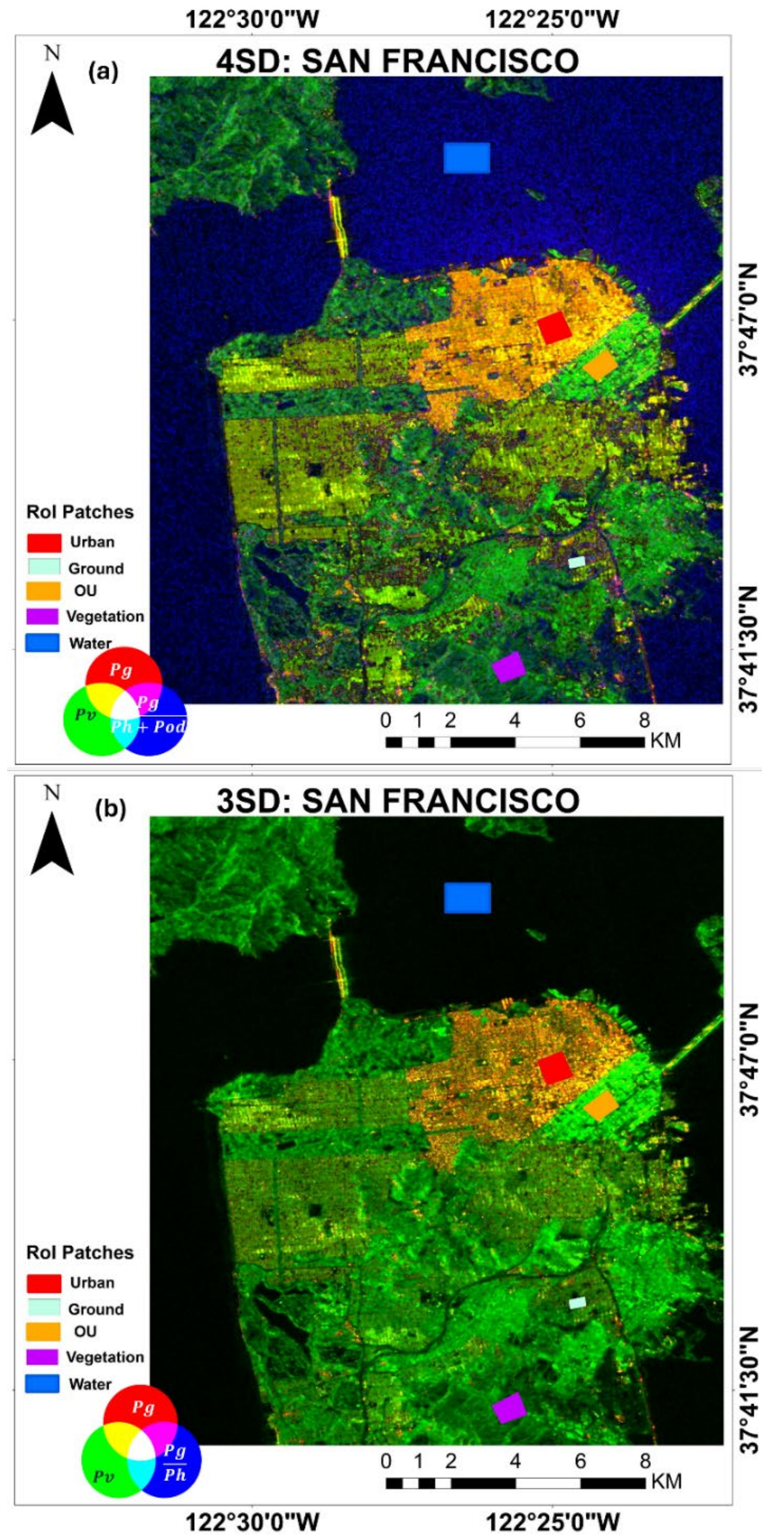

Figure 5.5 RGB images of (a) 4SD (b) 3SD for San Francisco with RoIs

It improves the LULC classification accuracy, especially for areas that depict complicated scattering mechanisms, such as the oriented urban area and vegetation in San Francisco. This was demonstrated by a consistent volume scattering reduction when using the 4SD model compared to the 3SD model. This can only be attributed to the fact that the oriented dipole scattering component captures scattering in a more effective way, especially in urban landscapes where buildings and other structures are oriented such that the radar signal interacts with several surfaces to produce compound scattering effects.

This new scattering component provided a more detailed view of how different surfaces backscatter radar signals, thereby increasing the accuracy of the LULC. For instance, there was a significant reduction in ground scattering in the ground and urban patches obtained using the 4SD model. For instance, the ground scattering in the ground patch reduced from 90.3% to 77.8%, while that in the urban patch reduced from 97.5% to 84.8% (Figure 5.6). This reduction is compensated for by the increase in the oriented dipole scattering component, which suggests that urban features, such as small structures and grid-like street layouts, are oriented in a way that contributes to compound scattering, which aligns along the radar's line of sight, giving rise to scattering that cannot be modeled by the 3SD model.

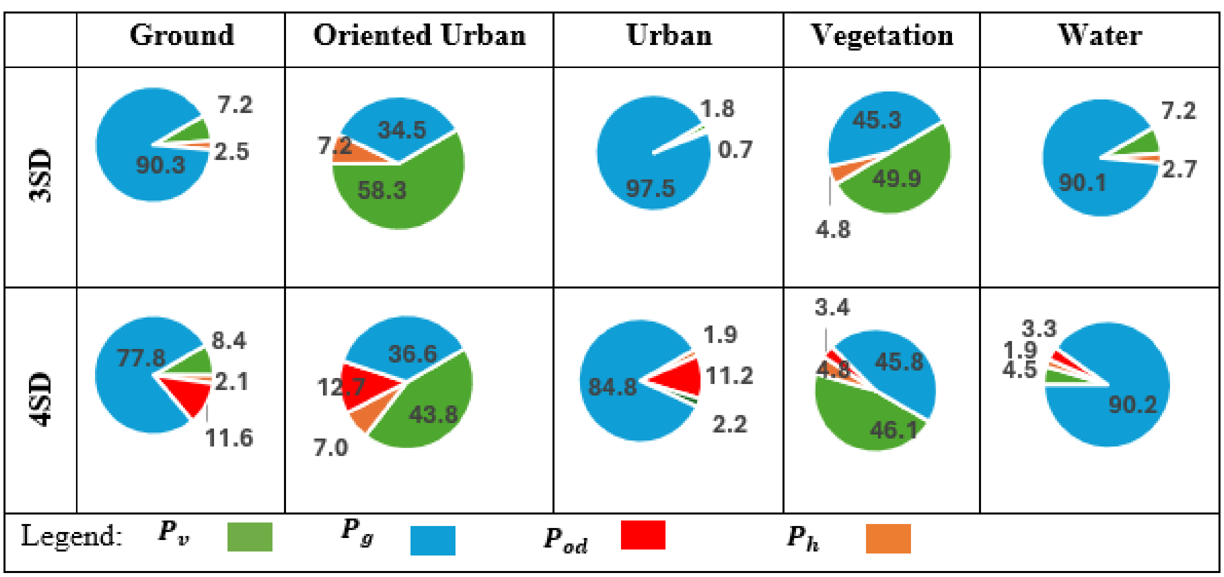

Figure 5.6 Model-based decompositions (3SD, 4SD) power statistics for San Francisco

The 4SD model has the ability to distinguish surface and small urban structures and identify the specific scattering behavior of streets and buildings, proving that this decomposition algorithm outperforms the existing algorithms. It can be analytically seen from the given that water bodies return a high percentage of ground scattering of approximately 90%, which is represented by a blue color in RGB visualizations. A strong ground-scattering signature is expected because the smooth surface of the water reflects most of the radar signal back to the sensor. Again, it is this hilly topography with slopes of varying gradients from gentle to steep, which again illustrates the 4SD model advantage. In vegetated patches, the orientation of the slopes with respect to the radar's line of sight forms an oriented surface configuration such that cross-polarization effects appear.

This slope-induced cross-polarization led to an increase in volume scattering. Slopes in low-and sparsely vegetated areas also resulted in an enhanced ground-scattering contribution due to slopes, as observed by the 4SD model. Such terrains have a better representation of the scattering power owing to their ability to account for slope effects and the orientation of surface features in the 4SD model. Oriented dipole scattering becomes rather important in vegetated areas, where the structure of trees has an oriented structure of their branches, in such a way that compound scattering of the radar signal occurs. This occurs within some species where the structure of the branches can produce multiple scattering events that are captured more accurately by the 4SD model than by its predecessor, the 3SD model. It is this complex scattering behavior that the 4SD model can represent with better accuracy when trying to differentiate surface characteristics from densely vegetated, urban, and other land-cover types.

5.4.2 Comparison of LULC Classification Based on 3SD and 4SD Scattering Powers

The full potential of this DP-4SD model was investigated by applying it to land use/land cover classification and comparing it with classification based on the existing 3SD. A supervised random forest classification algorithm was employed, and the performance of the proposed 4SD model was further evaluated using data from dual polarization from two regions: Haldwani Forest in India and San Francisco urban region in the United States. These two sites were selected to test the model performance for different geographies and land cover classes. This testing was performed for two major purposes: checking the performance of the model in classifying areas containing a homogeneous class, such as a forested region in Haldwani, and its performance in heterogeneous LULC classes that are characteristic of highly complex urban environments, such as in San Francisco.

The 4SD model performed well, with a high overall accuracy of 85.69% and a kappa coefficient of 0.81 in the Haldwani Forest (Table 5.2), reflecting strong agreement between the predicted and actual classifications. The outputs produced outperformed the existing 3SD model, achieving an overall accuracy of 84.90%. Classification maps are shown in Figure5.7.

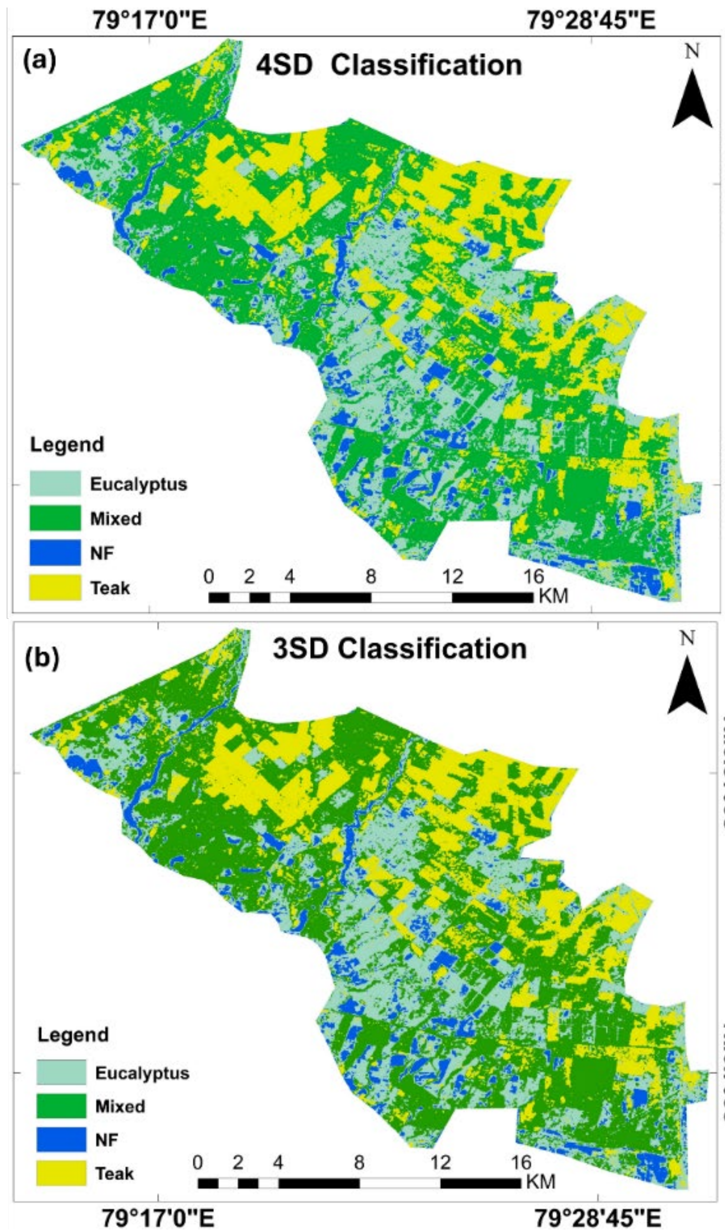

Figure 5.7 Forest species classification based on (a) 4SD (b) 3SD

The slightly improved accuracy of the 4SD model is considerably relevant, particularly in a complex ecosystem such as a forest, owing to the multiple above-mentioned scattering mechanisms present owing to the varied structure of trees, vegetation, and forest composition.

Table 5.2 Haldwani:

Confusion matrix for (a) 3SD, (b) 4SD with User Accuracy (UA), Error of Commission (EC) Producer Accuracy (PA), Error of Omission (EO), and (c) overall accuracy.

(a) 3SD							
Ground Truth	**Predicted**						
	Eucalyptus	**Mixed**	**NF**	**Teak**	**Unclassified**	**UA (%)**	**EC (%)**
Eucalyptus	7223	740	1549	252	278	**71.93**	**28.07**
Mixed	29	9610	284	91	0	**95.97**	**4.03**
NF	270	3	4435	0	0	**94.20**	**5.80**
Teak	268	1409	0	8329	91	**82.49**	**17.51**
PA (%)	**92.72**	**81.70**	**70.76**	**96.04**			
EO (%)	**7.28**	**18.30**	**29.24**	**3.96**			

(b) 4SD							
Ground Truth	**Predicted**						
	Eucalyptus	**Mixed**	**NF**	**Teak**	**Unclassified**	**UA (%)**	**EC (%)**
Eucalyptus	7281	746	1478	269	268	**72.51**	**27.49**
Mixed	21	9725	0	196	72	**97.11**	**2.89**
NF	244	1	4462	0	1	**94.77**	**5.23**
Teak	239	1327	0	8406	125	**83.25**	**16.75**
PA (%)	**93.53**	**82.42**	**75.12**	**94.76**			
EO (%)	**6.47**	**17.58**	**24.88**	**5.24**			

(c) Overall Accuracy		
	3SD	**4SD**
Overall Accuracy (%)	84.9	**85.69**
Kappa Coefficient	0.79	**0.807**
Unclassified Samples (%)	1.05	**1.03**

This is because the oriented dipole scattering component is included in the 4SD model, which significantly enhances the capability of this model to capture complex scattering behaviors depicting different forest species. Such an improvement in classification is important for forest cover mapping because it can provide more detailed differentiation between forest species, which may be important for applications in biodiversity assessments, carbon stock estimation, and forest management practices. It was also observed that the number of unclassified samples was reduced compared with the 3SD-based classification, further justifying the better performance of the 4SD model in the classification of forest types.

In the case of San Francisco, the DP-4SD model was highly effective, with an overall classification accuracy of 93.66%, in contrast to the existing 3SD-based classification model, which had an accuracy of 91.04% (Table 5.3). The high accuracy in a complex urban setting characterized by diverse built-up, vegetation, and water body classes underlines the increased ability of the 4SD model to classify different land-use classes in the urban landscape. Classification maps are shown in Figure 5.8.

Since DP-4SD relies only on HH and HV polarization channels, its ability to accurately distinguish urban areas based on double-bounce scattering is compromised. In contrast, full polarimetric data, which also includes VV and HV channels, provides more comprehensive information about the interactions between radar signals and urban surfaces, leading to better urban area classification. Urban areas exhibit more complex scattering behaviors, often requiring the inclusion of additional polarimetric channels (VV) to fully capture interactions such as the corner reflector effect, which happens when radar waves bounce between two perpendicular surfaces (e.g., buildings and streets). In dual-pol data (HH and HV), some of these intricate scattering patterns may not be fully resolved, and the DP-4SD model may overestimate surface scattering in urban areas or misclassify urban structures as natural features. For accurate urban area separation, other scattering decomposition techniques designed for full-pol data, such as the Freeman-Durden decomposition (Freeman & Durden, 1998) or Yamaguchi decomposition (Yamaguchi et al., 2005), are typically used. These techniques provide better differentiation of urban features by leveraging the full polarimetric channels to capture double-bounce scattering. In the absence of quad-pol data, dual-pol approaches like DP-4SD can be applied for urban classification.

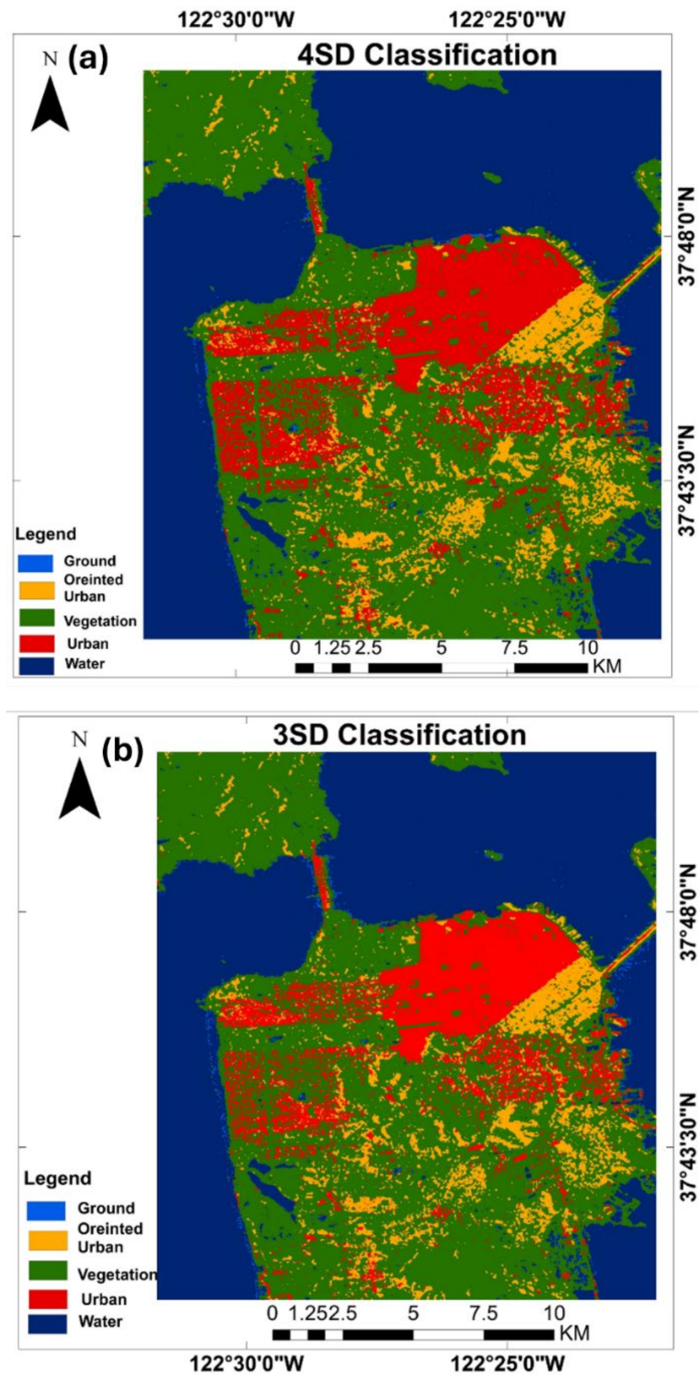

Figure 5.8 LULC classification based on (a) 4SD (b) 3SD

Changes in the area covered by forest plantation species, according to 3SD and 4SD, are evident in Figure 5.9. The model developed based on 4SD was finer in demarcation of forest species, hence more accurate classification and representation of actual forest cover, which may have implications for the improved monitoring of deforestation and forest health.

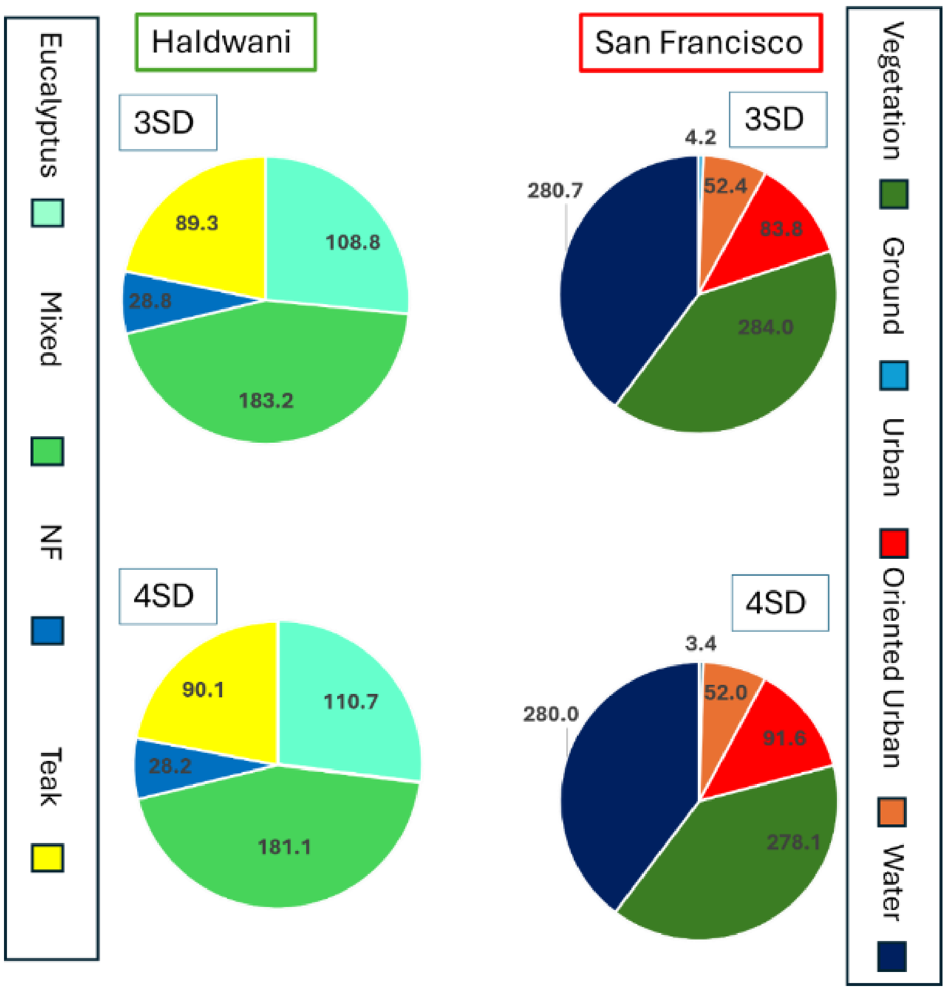

Figure 5.9 Area (km^2) covered by different LULC classes

The DP- 4SD model significantly reduced the number of unclassified samples to 0.701% in the DP- 4SD model-based classification compared with 2.88% in the classification based on the 3SD model. This marked reduction in unclassified regions ensures less presence of unclassified areas in the LULC classification.

Table 5.3 San Francisco:

Confusion matrix for (a) 3SD, (b) 4SD with User Accuracy (UA), Error of Commission (EC), Producer Accuracy (PA), Error of Omission (EO), and (c) overall accuracy.

(a) 3SD								
Ground Truth	**Predicted**							
	Ground	**OU**	**Urban**	**Vegetation**	**Water**	**Unclassified**	**UA (%)**	**EC (%)**
Ground	**2**	0	0	0	36	22	**3.33**	**96.67**
OU	0	**463**	0	11	0	5	**96.66**	**3.34**
Urban	0	13	**2765**	437	0	292	**78.84**	**21.16**
Vegetation	0	421	0	**3321**	0	116	**86.08**	**13.92**
Water	1	0	0	0	**7204**	0	**99.99**	**0.01**
PA (%)	**66.67**	**51.62**	**100.00**	**88.11**	**99.50**			
EO (%)	**33.33**	**48.38**	**0.00**	**11.89**	**0.50**			

(b) 4SD								
Ground Truth	**Predicted**							
	Ground	**OU**	**Urban**	**Vegetation**	**Water**	**Unclassified**	**UA (%)**	**EC (%)**
Ground	**5**	0	0	0	50	5	**8.33**	**91.67**
OU	0	**476**	0	2	0	1	**99.37**	**0.63**
Urban	0	20	**3188**	231	0	68	**90.90**	**9.10**
Vegetation	0	546	0	**3280**	0	32	**85.02**	**14.98**
Water	2	0	0	0	**7205**	0	**99.97**	**0.03**
PA (%)	**71.43**	**45.68**	**100.00**	**93.37**	**99.31**			
EO (%)	**28.57**	**54.32**	**0.00**	**6.63**	**0.69**			

(c) Overall Accuracy		
	3SD	**4SD**
Overall Accuracy (%)	91.04	**93.66**
Kappa Coefficient	0.86	**0.904**
Unclassified Samples (%)	2.88	**0.701**

This is important for land cover mapping, where unclassified areas can lead to gaps in the analysis and misinformed decision making. A comparison of the areas covered by different LULC classes based on the 3SD and 4SD models revealed that in the 4SD based classification there was a reduction in the vegetation class area by approximately 6 km^2, which was covered by an increase in the urban class area (Figure 5.9).

This can be explained by the fact that the oriented dipole scattering component within the 4SD model improves the characterization of the scattering behavior of urban structures and oriented branches within vegetation, decreasing the misclassification of urban areas into vegetated areas. The model DP-4SD has enhanced the detection of subtle variations in surface characteristics, vegetation structures, and building features by fully exploiting dual-polarization SAR data. Greater interpretation of polarimetric signals with enhancement in LULC classification may be helpful for better environmental monitoring and resource management, along with urban development. The implications of the DP-4SD model are multi-faceted. With the 4SD model, forest monitoring for changes in forest cover and early signs of deforestation or degradation can be detected to monitor health and structure using time-series dual-PolSAR data. This would result in a more timely and efficient approach for conservation, informed management of forests, and better understanding of shifts in forest dynamics due to climate change and human interference. The 4SD model can improve the classification of diverse urban structures and enhance the analysis and management in cities. Classification maps detailing the precise distribution of urban green spaces, buildings, and other classes of land use will be of great assistance to urban planners and policymakers. Thus, improvement in classification performance will serve to improve policies towards urban growth, development of green infrastructure, and mitigation of the urban heat island effect. Moreover, the possibility of the model DP-4SD to provide a more accurate classification with fewer unclassified samples could be particularly useful in dynamic environments, such as those with rapid urban growth or in areas prone to natural disasters.

5.4.3 Discussion

The superior performance of the DP-4SD model over the DP-3SD model in land use/land cover (LULC) classification, particularly in complex forest and urban areas, highlights the advantage of incorporating the oriented dipole scattering component to address volume scattering overestimation in the existing decomposition model (Sugimoto et al., 2023). The new model captures oriented dipole structures present in urban areas, vegetated regions, and sloped surfaces (Singh and Yamaguchi, 2018). The strong contribution of oriented scattering mechanisms in these features enhances classification accuracy compared to the DP-3SD model (Sugimoto et al., 2023), enabling clear distinction and classification of buildings, streets, vegetation, and forest species.

The reduction in volume scattering and the corresponding increase in oriented dipole scattering contributions in forested regions demonstrate the DP-4SD model’s ability to capture nuanced scattering behaviors, such as multiple interactions between radar signals and tree branches. These findings emphasize the DP-4SD model's suitability for characterizing complex ecosystems and diverse land cover types. The DP-4SD model outperformed the DP-3SD model in both forested and urban settings: Forested Areas (Haldwani Region): The DP-4SD model achieved an overall accuracy of 85.69% with a kappa coefficient of 0.81, compared to 84.90% accuracy for the DP-3SD model. The inclusion of the oriented dipole scattering component enhanced the differentiation of forest species, enabling finer demarcation of forest cover and reducing the number of unclassified samples. The model’s ability to capture complex scattering interactions among tree branches, canopy structures, and ground features is critical for biodiversity assessments, carbon stock estimation, and forest health monitoring.

The DP-4SD model achieved a significantly higher accuracy of 93.66% compared to the DP-3SD model's 91.04%. The improved classification of urban features, including buildings, streets, and small structures, highlights the model's ability to distinguish between urban and vegetated areas. The reduction in misclassification is attributed to the oriented dipole scattering component, which effectively captures compound scattering behaviors typical of urban environments. The DP-4SD model notably reduced unclassified samples to 0.701%, compared to

2.88% in the DP-3SD model. This marked reduction ensures comprehensive LULC classification, minimizing gaps that could lead to inaccurate analyses. Such improvements are particularly valuable in dynamic environments with rapid urbanization or ecological changes.

The DP-4SD model provides better representation of forest composition, aiding in the detection of changes in forest cover and early signs of deforestation or degradation. Its ability to accurately differentiate forest species enhances conservation efforts and supports informed forest management practices. The improved classification accuracy and reduction in unclassified areas are vital for monitoring forest health and understanding the impacts of climate change and human activities on forest dynamics. The DP-4SD model enhances the classification of urban features, including green spaces, buildings, and streets, offering critical insights for urban planning and development. Detailed urban classification maps can assist in designing green infrastructure, mitigating urban heat island effects, and promoting sustainable urban growth. The model's ability to handle dynamic urban environments is particularly relevant for areas experiencing rapid growth or prone to natural disasters, ensuring accurate and timely monitoring of urban changes.

While the DP-4SD model offers enhanced accuracy and comprehensive LULC classification compared to other dual-polarimetric SAR methods, full polarimetric SAR data can further improve performance for complex target structures in urban and forest environments. The absence of full polarimetric channels (VV and HV) in dual-pol data limits the model's ability to fully capture complex scattering mechanisms, such as double-bounce scattering in urban areas. Future studies could integrate full-polarimetric SAR data to further enhance urban classification accuracy. Urban areas with intricate structures and high-density developments have challenges for dual-pol decomposition techniques. Developing a time-series DP-4SD model could also enhance monitoring of dynamic forest and urban changes.

5.5 Conclusion

This study introduces a novel model-based four-component scattering power decomposition for dual-polarization synthetic aperture radar (dual-pol) data by developing an oriented dipole, a novel scattering component for DP-4SD. The inclusion of this new component not only improves the accuracy of the PolSAR decomposition compared to earlier models but also emphasizes the benefits of oriented dipole scattering power, especially in densely vegetated regions and oriented urban structures. The urban-oriented structures and structures of the vegetation that generated dipole and dihedral scattering were identified using the DP-4SD model. The DP-4SD model demonstrated significantly improved classification accuracy compared to existing methods across different LULC classes. The DP-4SD model has the potential to advance the understanding of both natural and urban environments through more accurate classification and interpretation of land-cover types.

Chapter 6 : Forest Disturbance Detection Using Multi-frequency SAR Data

6.1 Introduction

Forest disturbance can be defined as a reduction in forest volume and quality resulting from deforestation or degradation. Deforestation leads to immediate loss of forest cover, causing significant disruption of ecosystem services including carbon sequestration, biodiversity support, and hydrological functions. Forest degradation refers to the gradual deterioration of vegetation health, which compromises the forest ecosystem over time. In addition to ecological functions, degradation also negatively affects the timber quality and productivity of forest stands. Silvicultural practices have been implemented to promote sustainable forest resource management, giving rise to plantation forestry. Currently, plantation forests account for 36% of global forest cover. In these managed forests, the intentional removal of trees, designated harvesting, is categorized into three distinct types based on the techniques used for timber extraction.

Forest degradation involves quantitative and qualitative decline in vegetation cover over extended periods, causing reductions in productivity and ecosystem health. In contrast to deforestation, forest disturbance is not a discrete event; rather, it is a continuous process driven by both natural dynamics and anthropogenic pressure. Degradation poses a significant environmental challenge, as it reduces canopy cover and biomass production. This reduction in forest productivity directly affects forest-dependent communities by diminishing economic opportunities and forest-based livelihoods. The decline of vegetation undermines the capacity of forests for carbon sequestration, which contributes to global warming by increasing atmospheric carbon levels. Degraded forests experience increased physiological stress, further destabilizing their ecosystems through feedback mechanisms that exacerbate disturbances in surrounding areas. In this weakened state, forests become vulnerable to natural hazards, such as wildfires, pest outbreaks, and unfavorable edaphic or climatic conditions. Key drivers of deforestation include mining, overgrazing, unsustainable logging, fuelwood collection, and the extraction of non-timber forest products (Miettinen et al., 2014). These practices are closely linked to socio-economic factors, including population growth, urban expansion, international trade, and policy decisions. Degraded forests exhibit reduced ecosystem stability and thus are prone to further disturbance and deterioration. Additionally, degraded ecosystems are susceptible to disruptions caused by fires, pests, and changing environmental conditions, contributing to the cyclical nature of degradation.

Forest canopy density is a critical indicator of forest health and a key parameter for measuring degradation (Lausch et al., 2016). Canopy density refers to the proportion of ground area covered by the cumulative leaf area of all trees. As a vital biophysical variable, it directly influences the photosynthetic capacity and productivity of forest ecosystems. Canopy cover also reflects the phenological state of the forest under adverse environmental conditions, reflecting factors such as leaf senescence. Anthropogenic activities, including fires, fuelwood extraction, lopping, and grazing, disrupt natural forests, reducing canopy density. These disturbances can result in irreversible damage to forest ecosystems, further accelerating degradation. Monitoring canopy density is essential for elucidating the health and stability of forests as well as to develop strategies for preventing long-term degradation. Historically, forest variables have been measured through ground-based surveys conducted by foresters and extrapolated statistically to larger areas. However, these methods often carry a high degree of uncertainty and have limited accuracy due to small sample sizes and assumptions made during extrapolation. Remote sensing technologies have revolutionized forest monitoring, enabling continuous and large-scale observations with varying spatial and temporal resolutions. Since 1972, with the launch of the Landsat program, remote sensing has become a prime data source for monitoring forest ecosystems, providing synoptic coverage and repeat observations that are critical for tracking forest changes over time. Initially, forest measurements were derived primarily from airborne and spaceborne sensors (Patenaude et al., 2005). Improvements in sensor technologies, including enhanced spatial, spectral, radiometric, and temporal resolutions, have enabled the estimation of key forest variables, such as leaf area index (LAI), vegetation cover, and canopy structure, over various time periods. The integration of remote sensing data with forest health parameters is essential to clarify the impacts of biotic and abiotic stress factors, such as drought, pests, diseases, and human activities, on vegetation growth. Remote sensing offers consistent and objective measurements that complement field-based assessments, thereby improving the accuracy and scope of forest health monitoring. Advanced remote sensing techniques allow for the monitoring of forest health indicators across large areas over time, providing insights into vegetation dynamics, phenological changes, and responses to environmental stressors (Lausch et al., 2016). This approach is particularly valuable for tracking the impacts of climate change, forest degradation, and deforestation, thereby supporting informed decision-making for sustainable forest management. Combining remote sensing observations with ecophysiological metrics allows forest managers and researchers to better understand the complex interactions between vegetation and environmental factors, leading to the development of more effective conservation strategies and ecosystem management practices.

Monitoring forests using remote sensing techniques requires two key components, namely defining forest regions and establishing relationships between forest parameters and remotely sensed data (Fagan and DeFries, 2009). These parameters include canopy characteristics, such as openness, LAI, water content, and phenology; structural variables, such as tree density, basal area, height, and diameter at breast height; forest floor properties (e.g., litter abundance, soil carbon content); and ecophysiological attributes. Identification of such relationships enhances the interpretation of remotely sensed data for accurate forest monitoring. Forest parameters can be grouped into four primary metrics, referred to as the forest identity: area, volume (stock density), biomass, and carbon sequestration (Kauppi et al., 2006). Remote sensing via sensors with varying resolutions and acquisition modes can effectively integrate these metrics for assessment of forest health (Lausch et al., 2016). Miettinen et al. (2014) categorized remote sensing approaches for forest disturbance monitoring into four groups:

1. **Direct detection of degradation indicators** using single or composite images.
2. **Time-series analysis** for detection changes in direct degradation indicators.
3. **Mapping of secondary indicators**, such as roads, logging sites, or villages, and establishment of degradation buffers around these features.
4. **Direct estimation of forest parameters** including above-ground biomass (AGB) and stem volume.

Although deforestation detection has been undertaken at the global scale using Landsat time series (Hansen et al., 2013), tropical regions present challenges due to persistent cloud cover, limiting the availability of cloud-free optical imagery. Synthetic aperture radar (SAR), with its high temporal and spatial resolution and cloud-penetrating ability, offers a complementary platform for continuous forest monitoring.

Most studies using SAR for forest disturbance detection rely on polarimetric backscatter for their detection algorithms (Joshi et al., 2017; Kuplich et al., 2005; Ningthoujam et al., 2016; Olesk et al., 2015; Santoro et al., 2009). Additionally, polarimetric SAR (PolSAR) decomposition (Lavalle, 2017; Lavalle & Hensley, 2015) and interferometric SAR (InSAR) coherence (Lei et al., 2018) have been employed to monitor forest changes. Olesk et al. (2015) compared the performance of C-band Sentinel-1 and L-band ALOS-2 PALSAR data for the detection of clear-cuts and thinning operations. Their findings revealed that C-band HV polarization backscatter could detect clear-cuts > 1 hectare, while L-band VH polarization backscatter was sensitive to smaller clear-cut areas (> 0.5 hectares) and thinning operations. The complementary nature of optical and SAR data has led numerous studies to fuse these data types for deforestation detection (Lehmann et al., 2012; Reiche et al., 2015, 2018). Reiche et al. (2015) demonstrated that combining SAR-derived HH/HV backscatter with Landsat-derived normalized difference vegetation index time-series data improves detection accuracy. This method was further enhanced for near real-time deforestation monitoring through the integration of dense Sentinel-1 time-series observations (Reiche et al., 2018, 2021). L-band cross-polarized (HV) backscatter has shown potential for detecting forest changes (Mermoz & Le Toan, 2016). Similarly, co-polarized (HH) backscatter is widely used for monitoring forest regrowth. An increase in L-band HV backscatter is associated with forest growth due to multiple scattering processes within the canopy, whereas a decrease typically indicates forest loss.

However, Joshi et al. (2017) noted that backscatter changes alone are insufficient for accurate detection of forest disturbance. They highlighted the need to incorporate information about the type of activity causing the disturbance as well as the condition of understory vegetation. Their study showed that the removal of emergent trees caused measurable changes in backscatter, whereas similar changes in understory vegetation did not affect the signal. This result indicates that quad-polarization SAR data, which provide additional scattering information, are necessary for reliable detection. Despite the greater information content available from quad-polarization SAR data, its use in forest disturbance and regrowth studies has been limited (Kobayashi et al., 2012; Trisasongko, 2010). Mathematical model-based decomposition techniques were employed by Trisasongko (2010), while physical scattering-based models have been used by other researchers (Kobayashi et al., 2015; Priyanka et al., 2023; Watanabe et al., 2018).

Physical scattering-based models (Singh et al., 2013a; Sugimoto et al., 2021; Yamaguchi et al., 2006) classify land features into surface, volume, dihedral, and helix scattering components based on radar wave interactions representing known geometric structures. These models have been successfully employed in previous studies to characterize forest growth (Kobayashi et al., 2012, 2015) and detect forest disturbance. Kobayashi et al. (2015) distinguished between canopy and understory growth, while Watanabe et al. (2018) identified post-disturbance changes in scattering behavior, which caused uncertainty in early-stage deforestation detection. A key remaining challenge is the limited availability of PolSAR data. Developing a model for dual-polarization data that can accommodate such variability is crucial for effective monitoring and assessment of natural forests with heterogeneous structural characteristics.

6.2 Test Site and Data

The Haldwani forest range is located between 29° 00′ N and 29° 15′ N latitude and 79°15′ E and 79°30′ E longitude (Figure 6.1) in Uttarakhand state, India, in the foothills of the lower Shiwalik Hills.

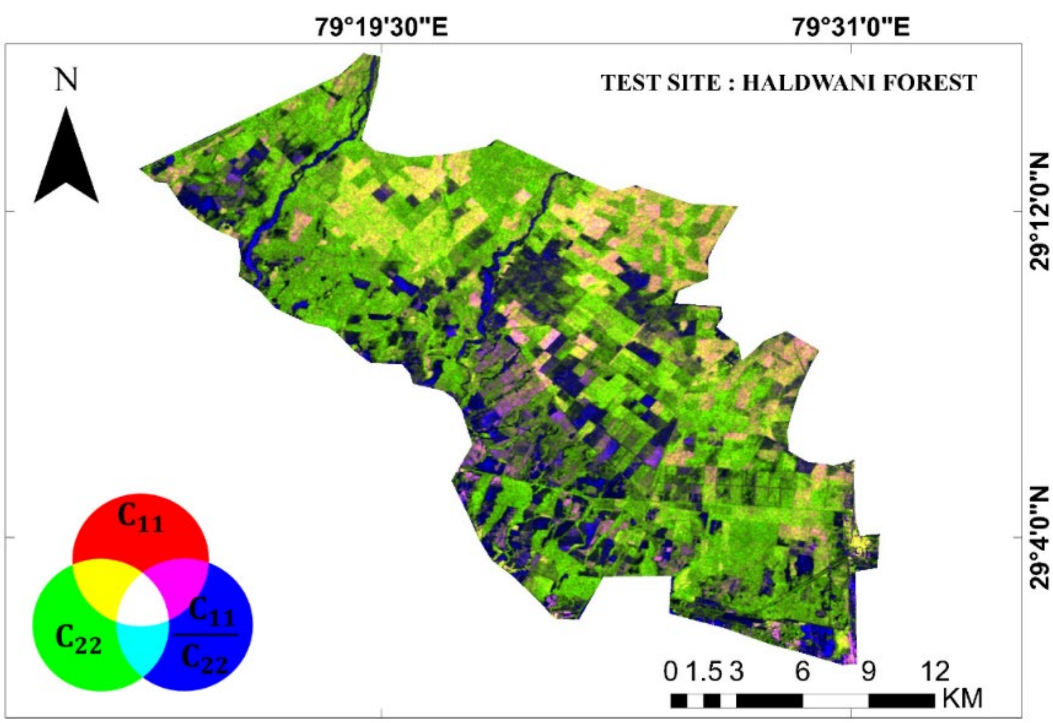

Figure 6.1 Test site: Haldwani forest

The climate of the Haldwani forest range is typically subtropical, characterized by hot summers, mild winters, and a significant monsoon season. The elevation ranges from approximately 500 m (1,640 ft) above sea level in lower areas to over 1,000 m (3,281 ft) in higher regions near the hills. It is a managed forest area with a unique species distribution in well-delineated forest compartments. In this study, I utilized datasets from the Advanced Land Observation Satellite (ALOS), equipped with the Phased Array type L-band Synthetic Aperture Radar (PALSAR), and the Advanced Land Observing Satellite-2 (ALOS-2), which features the Phased Array type L-band Synthetic Aperture Radar-2 (PALSAR-2). PALSAR's ability to operate in multiple polarization modes enables detailed surface analysis, supporting applications such as deforestation monitoring and target classification (Hayashi et al., 2019; Olesk et al., 2015; Padalia & Musthafa, 2017; Tadono et al., 2019; H. Zhang et al., 2023). Datasets were acquired for both test sites, as listed in Table 6.1.

Table 6.1 Details of the SAR datasets

Satellite/Sensor	Date of Acquisition	Polarization
ALOS-2/PALSAR-2	2018-04-15	Dual-Polarization
	2022-03-27	
Sentinel-1	2018-03-23	Dual-Polarization
	2020-03-26	

The Sentinel-1 mission, part of the European Space Agency (ESA) Copernicus program, provides C-band SAR data (~5.4 GHz) with dual-polarization capabilities (VV + VH or HH + HV), enabling all-weather, day-and-night monitoring (Potin et al., 2014; Snoeij et al., 2009; Torres et al., 2018). This instrument offers high temporal resolution (6–12-day revisit period) and 20-m spatial resolution, making it valuable for deforestation detection, land cover monitoring, soil moisture estimation, and flood mapping. C-band SAR primarily interacts with canopy surfaces and tertiary branches, limiting its ability to penetrate dense forests, and also complements longer-wavelength (e.g., L-band) SAR data by capturing surface-level vegetation changes (Nandy et al., 2021). Sentinel-1's open-access data support large-scale environmental monitoring, and its frequent acquisitions allow for dynamic tracking of forest changes, particularly when integrated with L-band SAR for improved forest biomass estimation.

6.3 Methodology:

The preprocessing of ALOS-2/PALSAR-2 dual-polarization SAR data involved several essential steps to prepare the data for quantitative analysis. First, radiometric calibration was employed to convert raw digital numbers into complex data, normalizing for sensor and environmental biases (Shimada et al., 2014). To reduce speckle noise, multi-looking was performed, averaging the image over a 3 × 7 window in the range and azimuth directions, which improved visual quality while preserving essential spatial details. Following this step, a 2 × 2 covariance matrix was generated from the VV and VH polarizations, capturing complex scattering information crucial for the analysis of target properties (Touzi, 2007). A refined Lee filter was then applied to further reduce speckle noise and smooth homogeneous areas while retaining edges for improved radiometric stability (Lee et al., 2009). Finally, terrain correction was conducted using a Shuttle Radar Topography Mission (SRTM) digital elevation model (DEM) to correct topographic distortions (Farr et al., 2007). This step re-projected the SAR data from slant-range to ground-range geometry, ensuring that each pixel accurately represented the corresponding ground location and allowing for accurate spatial analysis and comparison with in situ and other geospatial datasets.

The preprocessing of Sentinel-1 SAR data to ensure accurate and reliable analysis involves several key steps (Figure 6.2). Initially, orbit files are applied to enhance the geolocation accuracy using precise satellite positional information, which refines the image geometry for each acquisition. Radiometric calibration converts raw image values into complex data that include both phase and intensity, which standardizes data across acquisitions and improves comparability (Sentinel-1 User Handbook, 2013). Debursting is then applied to seamlessly merge the Sentinel-1 bursts along the azimuth, providing a continuous image without the interruptions that are typical in the satellite's interferometric wide mode (Filipponi, 2019). To reduce speckle noise, a multi-looking process is employed, typically using a 3 × 3 window in the range and azimuth directions; this averages pixel values, balancing noise reduction with the retention of spatial detail (J. S. Lee et al., 1994). A speckle filter, such as the refined Lee filter, is then applied to further reduce speckle effects, thereby preserving essential details within homogeneous areas while maintaining the sharpness of boundaries. Finally, terrain correction with an SRTM DEM or equivalent high-resolution DEM is used to reproject the image from slant-range to ground-range geometry, correcting for topographic distortions such as foreshortening and layover (Farr et al., 2007). This terrain correction process ensures that each pixel accurately corresponds to a ground location, making the data suitable for integration with other spatial datasets and in situ measurements.

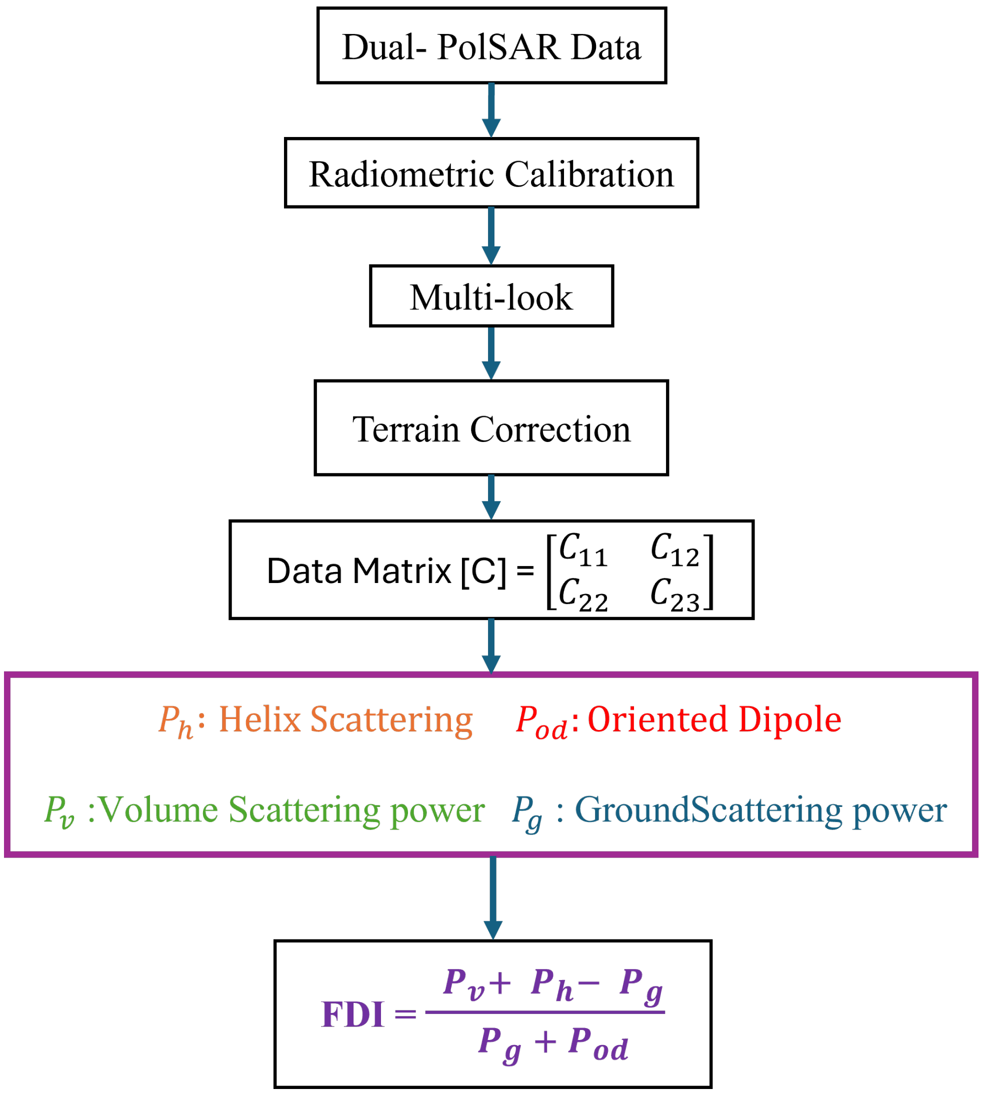

Figure 6.2 Implementation flowchart of the proposed FDI and biomass estimation.

As dual-polarization SAR measurements contain only two complex elements (S_{VV} and S_{VH} or S_{HH} and S_{HV}), the full coherency matrix and Pauli scattering vector cannot be directly generated from dual-pol data. However, the polarimetric information contained in the 2 × 2 covariance matrix $\langle[C_2]\rangle$ ($\langle[C_H]\rangle$ or $\langle[C_V]\rangle$) can be related to the full 3 × 3 scattering coherency matrix based on established relationships between dual-polarization and fully PolSAR data (Sugimoto et al., 2023):

To enhance the utilization of dual-pol data, a novel four-component scattering model (4SD-DP) developed specifically for dual-PolSAR data (discussed in detail in Chapter 5) has been employed to generate scattering powers, namely ground scattering power (P_g), helix scattering power (P_h), volume scattering power (P_v), and oriented dipole scattering power (P_{od}). The 4SD-DP model was implemented on ALOS-2/PALSAR-2 (L-band) and Sentinel-1 (C-band) data to capture diverse scattering behaviors across forested landscapes. All resulting scattering powers were normalized to ensure comparability among datasets and frequency bands. Using normalized scattering powers, I developed the FDI , which provides a quantitative measure of forest conditions based on changes in forest structure and disturbance detection. The FDI formula is:

$$\text{FDI} = \frac{P_v + P_h - P_g}{P_g + P_{od}},$$

where

- P_g and P_{od} indicate oriented dipole scattering powers, which increase in disturbed forests due to reduced canopy cover.
- P_v and P_h represent volume and helix scattering powers, which are typically higher in undisturbed or healthy forests with dense canopies and complex structures.

FDI offers a powerful tool for monitoring forest health using dual-PolSAR data with high temporal resolution. This index leverages the distinct scattering power responses that correspond to the structural components of forests. Specifically, dense forests exhibit high volume scattering due to the interaction of SAR signals with multiple canopy layers and secondary branches. In contrast, sparse vegetation and disturbed forests reflect greater ground scattering power due to the reduction in canopy cover, which allows signals to reach the ground. FDI values range from −1 to 1, with values near −1 indicating higher ground scattering, suggesting intense forest disturbance or degradation, whereas values closer to 1 reflect healthy and dense forest conditions. Additionally, FDI is capable of tracking forest growth and regeneration following disturbance, making it a useful tool for both forest monitoring and restoration efforts.

To validate the FDI results, AGB was estimated using multi-frequency SAR data from ALOS-2/PALSAR-2 (L-band) and Sentinel-1 (C-band). A random forest machine learning model was employed to model the biomass, with 75% of the data used for training and 25% for validation. The model incorporated four-component scattering powers as predictor variables, capturing surface, volume, double-bounce, and helix scattering. The performance of three models, L-band SAR, C-band SAR, and multi-frequency L- and C-band SAR, was assessed to compare their effectiveness. L-band SAR, with its longer wavelength, offers better penetration through the dense canopy and interacts with trunks and secondary branches, whereas C-band SAR primarily interacts with the canopy surface and tertiary branches, making the combination of both wavelengths most useful for biomass retrieval. Additionally, this study compared biomass between 2018 and 2022 using FDI to assess forest disturbance trends and regrowth patterns. Changes in biomass for various plantation species over this period were also analyzed to capture species-specific growth responses and recovery processes after disturbance. This approach demonstrates the utility of combining FDI with multi-frequency SAR data and machine learning models to accurately monitor forest health, biomass dynamics, and plantation growth patterns, thereby providing essential insights into sustainable forest management.

6.4 Results and Discussion

6.4.1 Forest Disturbance Detection

Initially, scattering powers based on the novel four-component scattering power decomposition for polarization (DP-4SD) model were derived independently for L-band and C-band SAR data. These scattering powers provide key insights into ground scattering, volume scattering, and specific polarimetric responses related to forest structure. To ensure alignment for multi-frequency analysis, L-band and C-band scattering data were spatially co-registered to align pixels across the two datasets. The total scattering power for both frequencies was then calculated by combining insights obtained from the distinct scattering behaviors of each frequency to strengthen the analysis.

Using this combined data, FDI was computed for 2018 and 2022, enabling a year-over-year comparison of forest health and structural changes. The FDI results (Figure 6.3) highlight that some areas experiencing degradation in 2018 showed significant regrowth by 2022, whereas other areas demonstrated new disturbance. Cross-comparison with forest plantation species classifications revealed that mixed-species plantations were the most strongly impacted, reflecting variable resilience among plantation types.

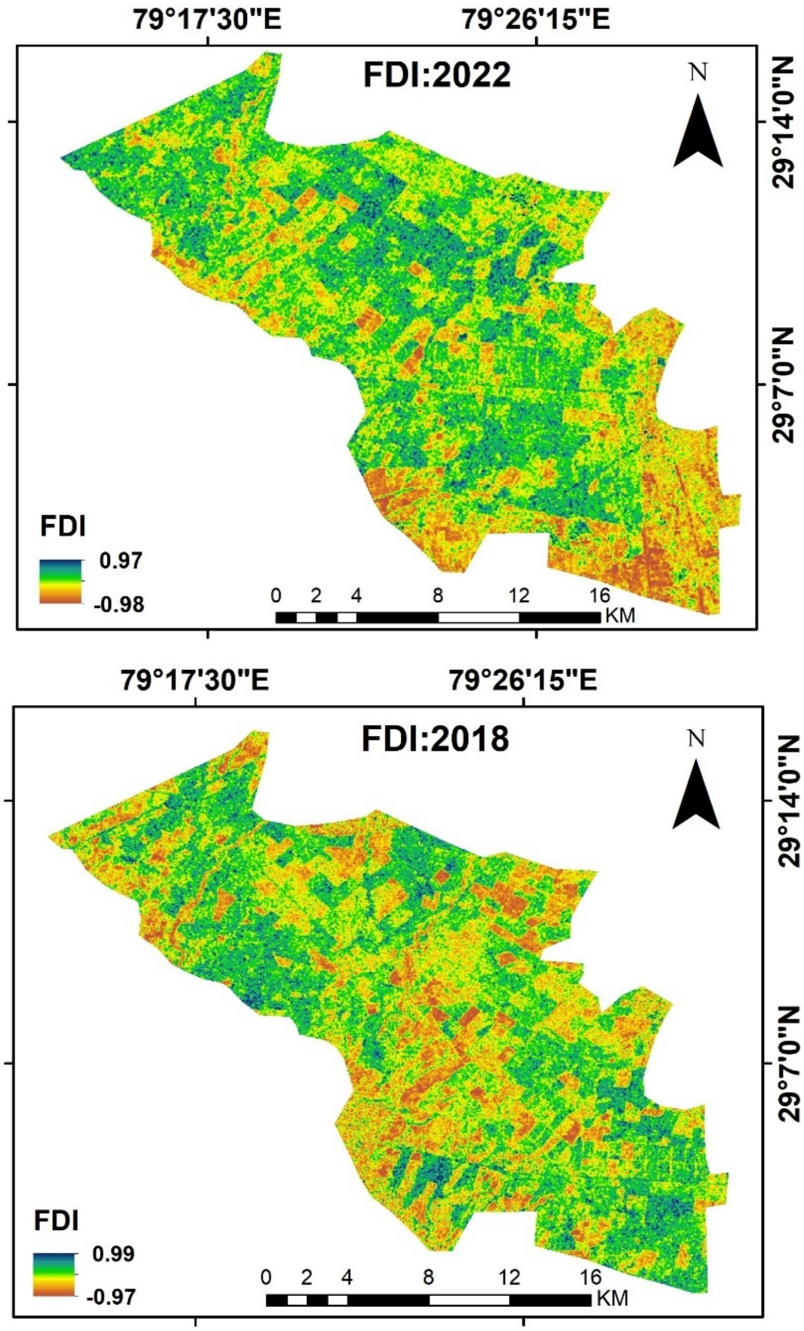

Figure 6.3 Spatial distributions of the Forest Disturbance Index (FDI) in 2022 and 2018

6.4.2 Forest Biomass Estimation

To validate the FDI results, AGB was estimated for both years using multi-frequency (L-band and C-band) SAR data. A random forest regression (RFR) model was applied to predict forest biomass, which was trained on 75% of the data and validated on the remaining 25%. The multi-frequency model, which integrated scattering information from both the L-band and C-band data, yielded the most accurate results, achieving a relative root mean squared error (%RMSE) of 21.84%. This result indicated marked improvement over single-frequency models using L-band (%RMSE of 23.11%) and C-band (%RMSE of 34.67%) data (Figure 6.4).

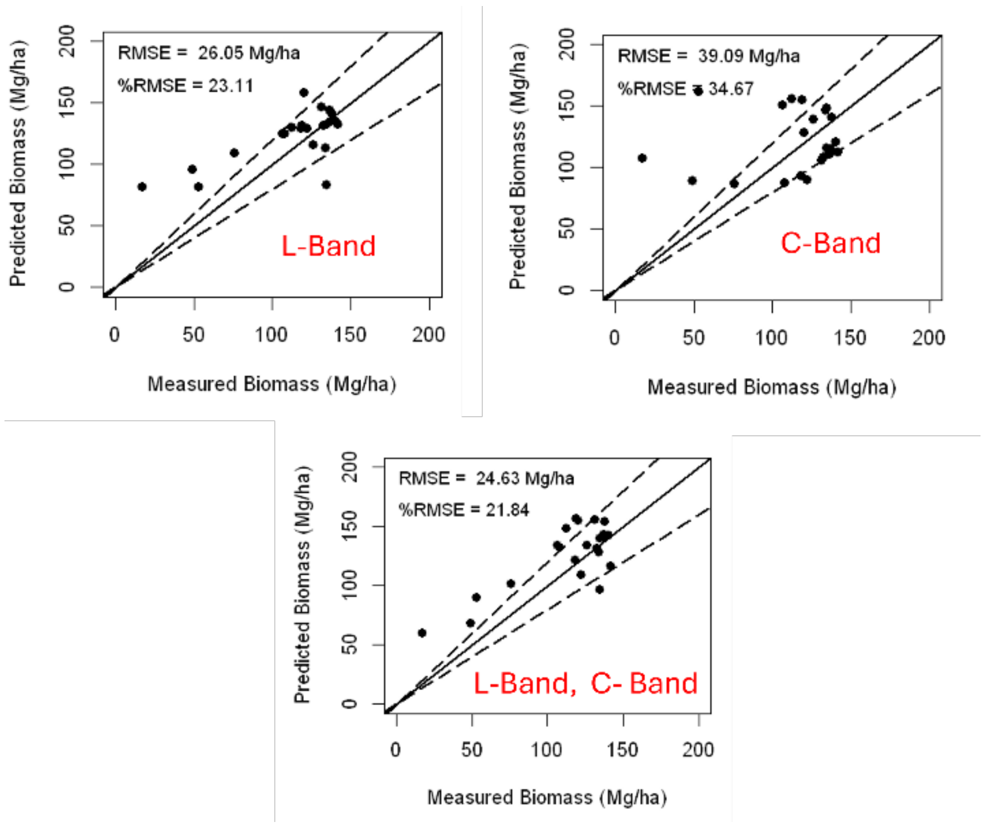

Figure 6.4 Validation of estimated forest biomass with field data.

The improved performance of the multi-frequency model confirmed that combining L-band and C-band data more comprehensively elucidates forest structure, capturing both high-density biomass components (due to the L band penetrating the trunk and branches) and canopy details (due to the sensitivity of the C band to leaves and smaller branches). This multi-frequency approach effectively improved the accuracy of biomass estimates, demonstrating the capacity of

FDI to track forest regrowth, disturbance, and structural changes over time. The spatial distribution of forest AGB, shown in Figure 6.5, provides an insightful visualization of forest health and disturbance over time. Areas of low biomass in 2022 align closely with high-disturbance zones on the FDI map, suggesting that disturbance had tangible impacts on biomass in these regions. FDI values, which range from −1 to 1, effectively capture the extent of forest degradation, with values closer to −1 indicating higher ground scattering and thus higher disturbance levels.

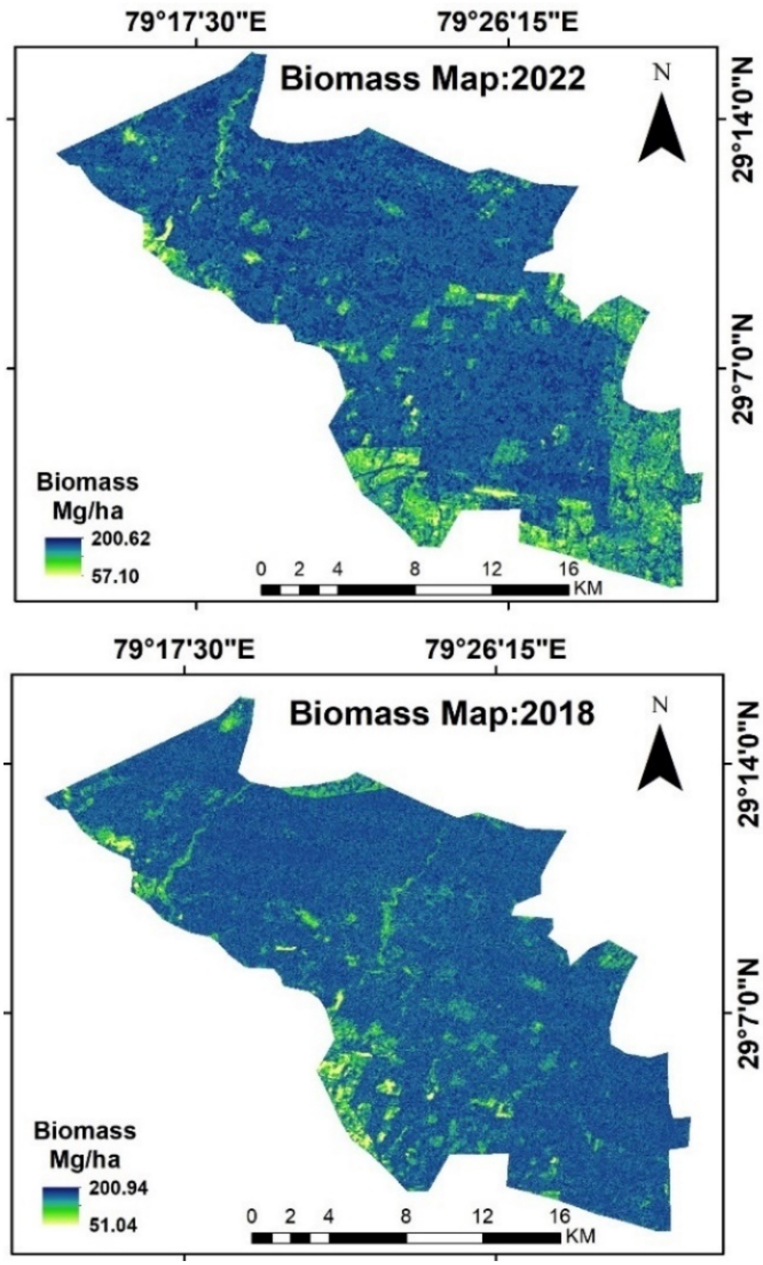

Figure 6.5 Spatial distributions of the forest AGB in 2018 and 2022

To further analyze which plantation species were most strongly affected by disturbance, biomass trends were examined for three primary forest types: mixed-species plantations, teak, and eucalyptus. Figure 6.6 illustrates the specific disturbance locations for each plantation type, marking where biomass loss occurred. Focusing on these species-specific disturbance locations enabled assessment of the resilience and vulnerability of each forest type to disturbance.

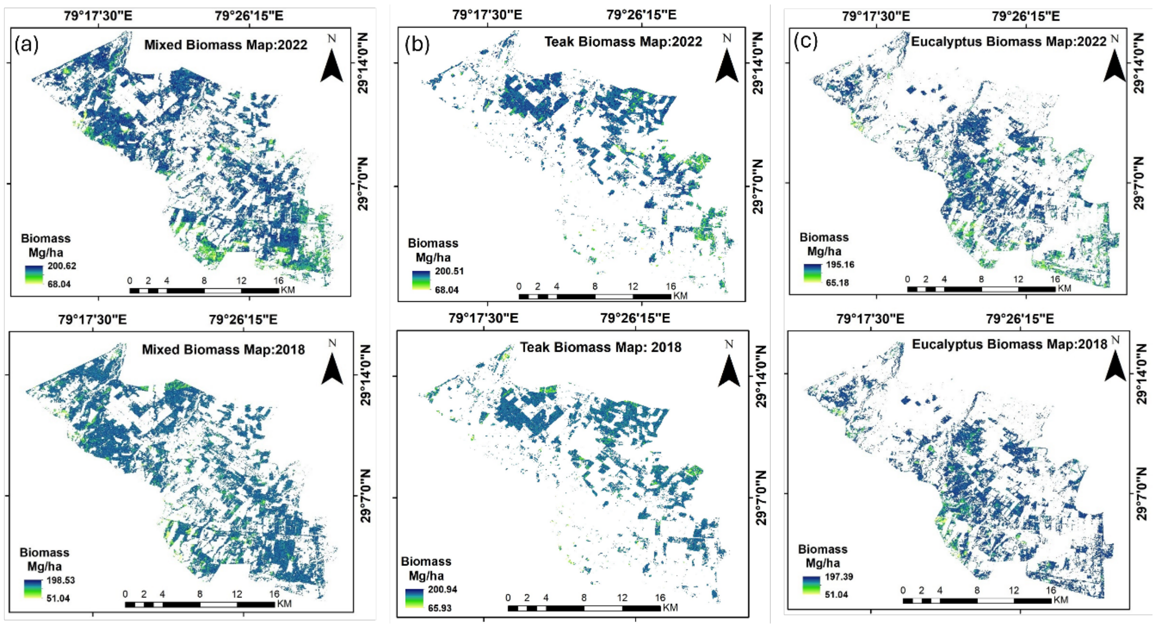

Figure 6.6 Forest Biomass of plantation species in 2018 and 2022

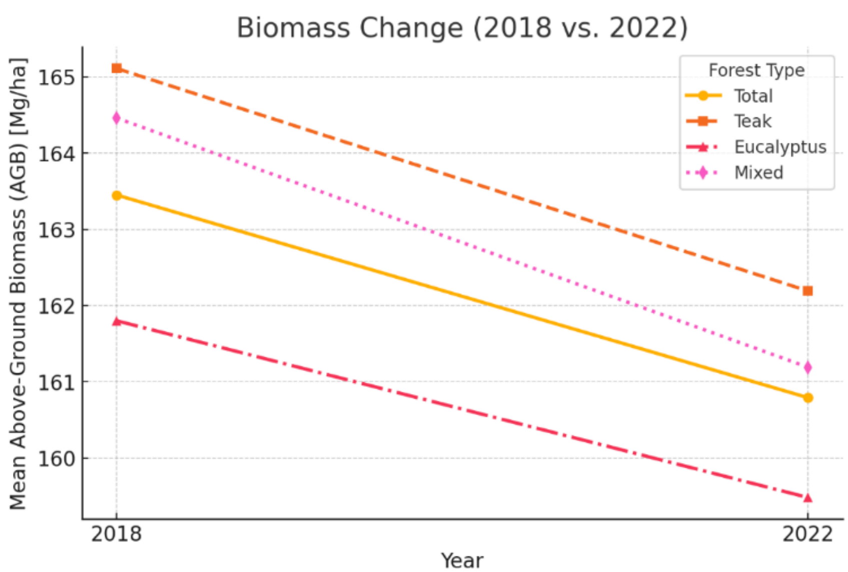

Figure 6.7 Mean AGB in 2018 and 2022

Mean biomass values decreased from 2018 to 2022 across all species types. Mean biomass for the entire forest decreased from 163.45 Mg/ha in 2018 to 160.79 Mg/ha in 2022, indicating a generalized impact across the landscape. For teak plantations, mean biomass dropped from 165.11 Mg/ha to 162.19 Mg/ha, while that for eucalyptus fell from 161.80 Mg/ha to 159.48 Mg/ha, and mixed species biomass dropped from 164.46 Mg/ha to 161.19 Mg/ha (Figure 6.7). These declines suggest that disturbance effects were widespread across various forest types, affecting overall biomass stocks and indicating reduced forest health.

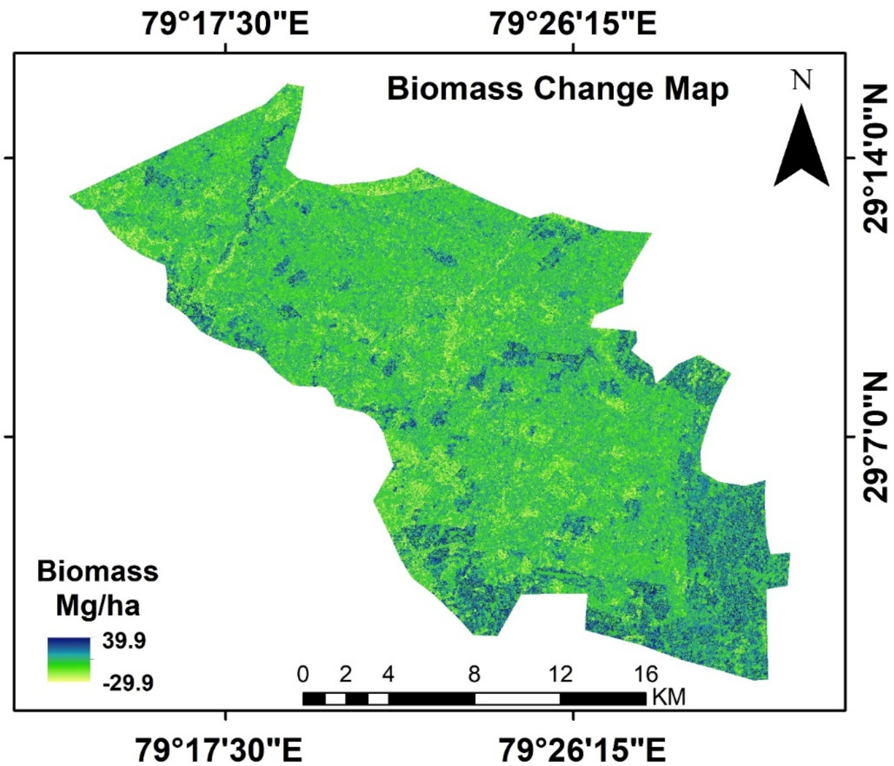

Figure 6.8 Biomass change map between 2018 and 2022

To clarify the extent of biomass changes, a biomass change map was generated by subtracting the 2018 biomass data from those for 2022 (Figure 6.8). This subtraction method highlighted areas with significant biomass loss, particularly in zones with high negative FDI values, thereby confirming that FDI can serve as a reliable indicator of disturbance-related biomass reduction. Notably, high biomass loss correlated with high negative FDI values, reinforcing the idea that such disturbance substantially impacts forest structure.

6.4.3 Forest Disturbance Detection in Pedrógão Grande Forest

FDI is also applied to the Pedrógão Grande Forest, located in the central region of Portugal within the Leiria district to detect the forest disturbance due to forest fire. This area is characterized by rugged terrain, steep slopes, and dense forest cover dominated by eucalyptus and pine plantations, which are economically significant but highly flammable. The Mediterranean climate, with hot, dry summers and mild, wet winters, contributes to its high wildfire susceptibility, exacerbated by poor forest management and the predominance of fire-prone species. The catastrophic Pedrógão Grande wildfire of June 2017, which caused significant loss of life and environmental damage, underscores the importance of this region as a focal point for studying wildfire dynamics, ecological impacts, and the role of sustainable forest management practices. The site serves as a critical example of the intersection between human activity, climatic factors, and wildfire risk, making it an ideal location for research into fire behavior, prevention strategies, and post-fire ecological recovery.

Table 6.2 Details of the SAR datasets

Satellite/Sensor	Date of Acquisition	Polarization
Before Forest Fire Sentinel-1	2015-05-14	Dual-Polarization
	2015-05-26	
	2015-06-01	
	2015-06-13	
After Forest Fire Sentinel-1	2015-06-25	Dual-Polarization
	2015-07-07	
	2015-07-19	
	2015-07-31	

The analysis leverages a multi-temporal Sentinel-1 dataset to detect and quantify forest disturbances caused by the forest fire in Pedrógão Grande, Portugal. Initially, the covariance matrix is computed for the entire dataset, encompassing both pre-fire and post-fire imagery. The developed DP-4SD (Decomposition Procedure for Scattering Diversity) technique is then applied to derive the scattering powers corresponding to various physical scattering mechanisms. Subsequently, the average scattering power for each component is calculated separately for the pre-fire and post-fire categories. Using these average powers, an FDI (Forest Disturbance Index) is generated to quantify the changes caused by the fire event. The results, as depicted in Figure 6.9, demonstrate the visible impact of the forest fire through visual interpretation, underscoring significant alterations in the scattering behavior of the forested region. This methodology highlights the efficacy of Sentinel-1 SAR data and advanced decomposition techniques in monitoring forest disturbances and evaluating post-fire recovery processes.

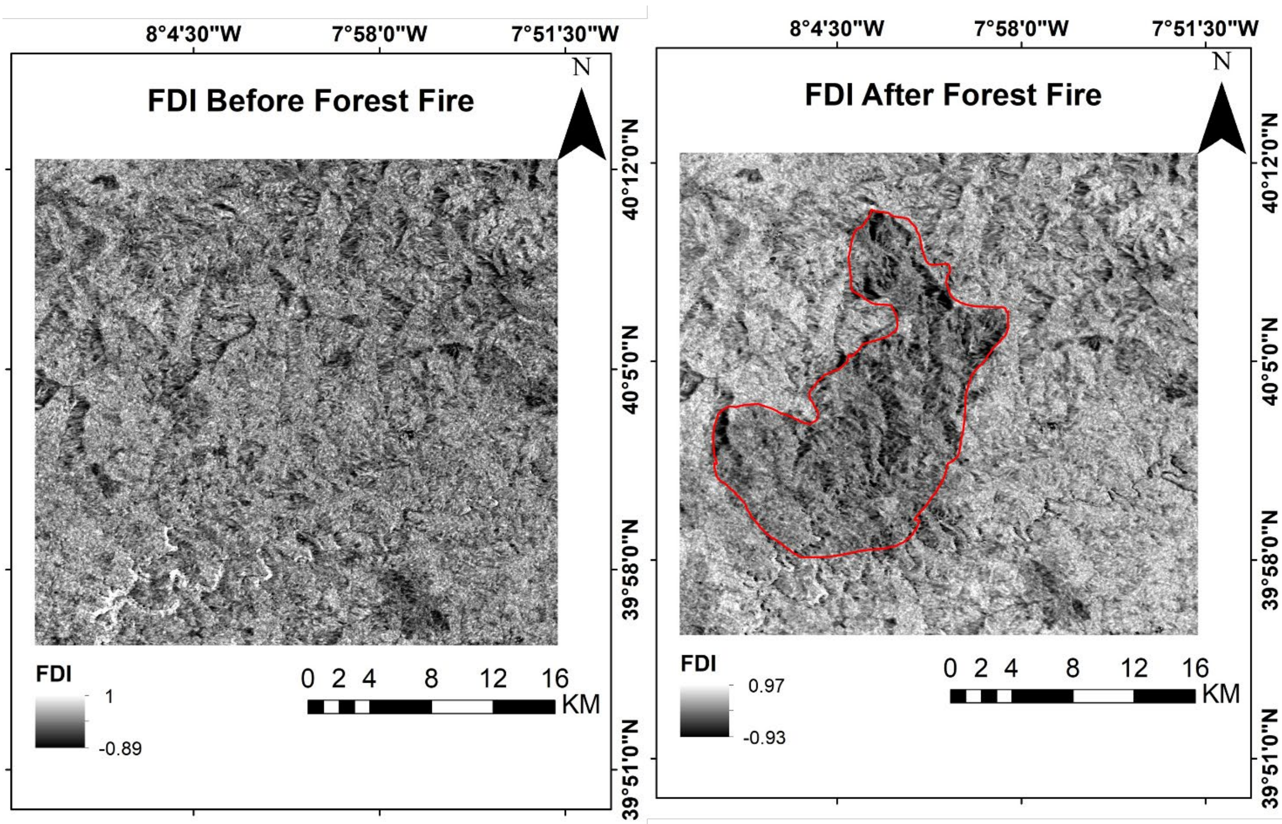

Figure 6.9 Forest disturbance index (FDI) before and after forest fire in Pedrogao Grande Portugal

The results of this analysis underscore the utility of FDI for identifying and monitoring disturbance patterns. The combination of FDI and biomass change analysis highlights specific areas of degradation while also indicating differing impacts among plantation species. This approach allows for comprehensive assessment of forest health over time, with FDI providing a valuable tool to track regrowth, ongoing disturbance, and changes in forest biomass, which are essential to forest management and conservation.

6.4.4 Discussion

This study demonstrates the effectiveness of the 4SD-DP model in combination with FDI and multi-frequency SAR data for monitoring forest disturbance, regrowth, and biomass dynamics over time. The integration of L-band and C-band SAR data better represents forest structure and health than either band alone, enabling comprehensive assessment of forest resilience and degradation. The use of FDI, computed from the combined L-band and C-band scattering powers, proved to be a robust approach for detecting and monitoring forest disturbance over a multi-year period. By aligning FDI values with biomass estimates, this study effectively linked structural changes in the forest to measured shifts in AGB. FDI's capability to distinguish between areas of regrowth and new disturbance emphasizes its utility for dynamic forest monitoring.

Most FDI studies primarily focus on dual-polarimetric backscattering coefficient analysis for forest change detection (Ban et al., 2020; Guoqing Sun et al., 2002; Hosseiny et al., 2024; W. Huang et al., 2015b; Ji et al., 2020b; Mullissa et al., 2024; Olesk et al., 2015; Pantze et al., 2010) but do not account for decomposition scattering power to develop new methods for detecting changes. Since scattering power provides effective information for characterizing targets, the developed Forest Disturbance Index (FDI), derived from the scattering power of the DP-4SD model using L- and C-band SAR data, is a useful tool for detecting forest disturbances and monitoring regrowth. By linking FDI values with biomass estimates, the study reveals patterns of recovery and disturbance from 2018 to 2022, driven by natural regeneration and human activities such as selective logging and plantation management. Mixed-species plantations experienced the highest disturbance and biomass losses, while teak and eucalyptus plantations showed greater resilience. A strong correlation between FDI values and biomass change validates FDI’s reliability. Areas with highly negative FDI values were associated with significant biomass loss, as observed in the case of the forest fire in Portugal.

The integration of FDI and biomass change analysis provides a scalable framework for forest monitoring. FDI enables early detection of disturbances, while biomass estimates quantify structural and carbon stock losses. Positive FDI values highlight areas of regrowth, which can be monitored to assess restoration success. This combined approach supports sustainable forest management, climate mitigation strategies, and carbon accounting initiatives such as REDD+.

However, certain limitations exist. L-band SAR saturation in high-biomass areas reduces sensitivity, and more frequent SAR acquisitions would improve temporal resolution. Overall, the combined use of the developed 4SD-DP model, novel FDI, and multi-frequency SAR data presents a robust tool for forest monitoring and management.

6.5 Conclusion

In conclusion, this study effectively demonstrated the potential of multi-frequency SAR data in combination with FDI for monitoring forest disturbance, regrowth, and biomass dynamics. FDI was demonstrated to be a reliable metric for detecting areas of high disturbance, as validated through biomass estimation, where low biomass values in 2022 corresponded closely with high negative FDI values in disturbed areas. By integrating L-band and C-band SAR data, the multi-frequency approach improved biomass estimation accuracy, reduced RMSE, and offered a more nuanced view of forest structure than single-frequency methods. Assessment of specific plantation species (mixed, teak, and eucalyptus) revealed that all types of biomass experienced losses from 2018 to 2022, with mixed species being the most strongly impacted, as indicated by lower biomass values in high-disturbance regions. This study underscores the effectiveness of combining SAR and FDI data for detailed forest health monitoring, particularly in regions experiencing frequent disturbance. The framework developed here provides valuable insights into forest dynamics, establishing a foundation for more effective forest management strategies and long-term conservation planning. Based on the tracking of regrowth, identification of degradation hotspots, and monitoring of biomass variations, this integrated approach will advance sustainable forest management practices and enhance resilience to environmental change.

Chapter 7 : Conclusion and Future Directions

This study integrated advanced remote sensing technologies to address challenges in monitoring forest ecosystems and urban landscapes. By combining innovative methods such as the seven-component scattering decomposition (7SD) model, the dual-polarimetric four-component scattering decomposition (DP-4SD) model, and multi-frequency synthetic aperture radar (SAR) with Global Ecosystem Dynamics Investigation (GEDI) LiDAR data, significant progress was made in the estimation of above-ground biomass (AGB), detection of forest disturbance, and land-use/land-cover (LULC) classification. The results demonstrate the potential of these techniques to enhance the accuracy and reliability of forest monitoring systems, contributing to sustainable management and conservation efforts.

7.1 Research Contributions

This study made four major contributions to algorithm development for forest monitoring and biomass estimation, as follows:

1. A novel model for forest AGB estimation using fully polarimetric L-band 7SD decomposition was developed.
2. A multi-sensor model integrating SAR and LiDAR data for enhanced forest biomass estimation was created.
3. An 4SD-DP model was introduced for dual-pol SAR data, improving land cover classification accuracy.
4. The 4SD-DP model was extended to develop the Forest Disturbance Index (FDI) and support multi-frequency SAR-based forest biomass estimation.

7.2 Forest Biomass Estimation Using SAR and LiDAR Data

The decomposition of SAR backscatter into distinct components allows for more nuanced representation of forest structure and scattering mechanisms. Two key models, the 7SD for full

PolSAR data and the proposed DP-4SD for dual-PolSAR data, were explored for application to biomass estimation and LULC classification. The 7SD model, which was applied to ALOS-2/PALSAR-2 L-band SAR data, disaggregated the radar backscatter signal into detailed components including volume scattering, double-bounce scattering, helix scattering, compound dipole scattering, and mixed dipole scattering. This level of granularity facilitated in-depth analysis of forest structure, canopy density, and biomass distribution. Volume scattering was dominant in dense forest areas with high biomass, reflecting the penetration of L-band signals into thick canopies and interactions with internal structures such as branches and trunks. Double-bounce scattering highlighted regions with sparse vegetation, where ground–trunk interactions were prevalent. This component was especially useful for the detection of degraded areas and forest margins. Compound scattering components captured forest heterogeneity, indicating variations in canopy gaps and structural anisotropy. These components were critical to identify complex scattering behaviors in mixed-species plantations. The model achieved relative root mean squared error (%RMSE) of 19.46%, outperforming traditional SAR backscatter-based methods. This improvement underscores the utility of advanced decomposition models for accurate biomass estimation in complex tropical forests.

Combining L-band (ALOS-2/PALSAR-2) and C-band (RADARSAT-2) SAR data improved the accuracy of biomass estimation. Each frequency contributed unique insights into forest structure, with the longer-wavelength L-band penetrating dense canopies to interact with trunks and primary branches, where most biomass is concentrated. This band was ideal for estimating AGB in high-density forests. The shorter-wavelength C-band was sensitive to surface-level interactions, capturing details of canopy surfaces and ground–trunk interfaces. This band complemented the deeper penetration of the L-band. The integration of L- and C-band data reduced the %RMSE of biomass estimation from 19.46% (L-band only) and 26.90% (C-band only) to 14.77%. This result highlights the complementary nature of these frequencies, with the L band capturing deeper structural features and the C band providing finer details of canopy elements. This combined approach is particularly effective in heterogeneous landscapes, where single-frequency models struggle to capture the full range of structural variability. The incorporation of GEDI LiDAR canopy height metrics further enhanced the accuracy of biomass estimation, providing critical information about vertical structure. The RH98 metric, selected to address anomalies caused by canopy gaps, was a robust predictor of biomass. When combined with multi-frequency SAR data, GEDI height metrics improved accuracy, yielding %RMSE of 14.24%.

7.3 Development of a Four-Component Scattering Power Model for Dual-PolSAR Data

The DP-4SD model introduced an oriented dipole scattering component to address the limitations of the existing three-component scattering decomposition (3SD) model. This addition significantly improved the accuracy of LULC classification, particularly in heterogeneous landscapes. The DP-4SD model reduced volume scattering across all forest types, enabling more accurate differentiation between forested and non-forested areas. Oriented dipole scattering captured the unique scattering behaviors of urban structures and vegetation, particularly in regions with complex canopy arrangements. The DP-4SD model achieved overall accuracy of 85.69% in the Haldwani Forest and 93.66% in San Francisco, surpassing the performance of the 3SD model. The reduction in unclassified areas further demonstrated the superiority of DP-4SD, demonstrating that it is a valuable tool for detailed LULC mapping and forest cover assessment.

7.4 Forest Disturbance Detection Using Dual PolSAR Data:

FDI, which is derived from multi-frequency SAR data, is an effective tool for monitoring forest health and structural changes. This index effectively captured degradation and regrowth patterns, aligning with observed biomass changes. Highly negative FDI values indicated areas of significant degradation, characterized by increased ground scattering and reduced canopy cover. Positive FDI values reflected regrowth, demonstrating the utility of this index for monitoring recovery over time. Biomass change analysis revealed a decrease in mean biomass from 163.45 Mg/ha in 2018 to 160.79 Mg/ha in 2022. This trend aligned with highly negative FDI values, confirming the reliability of the index for tracking biomass loss. The integration of FDI with biomass estimates provides a comprehensive framework for assessing forest health and resilience.

The findings of this study have wide-ranging implications for forest management, biodiversity conservation, and urban planning. Biomass maps and FDI metrics can be used to identify degraded areas, enabling targeted restoration efforts. Accurate biomass estimates will support climate change mitigation initiatives, such as REDD+ (Reducing Emissions from Deforestation and Forest

Degradation). The DP-4SD model allows for detailed differentiation among forest species, aiding in biodiversity assessment and habitat management. The DP-4SD model also enhances the classification of urban features, supporting sustainable urban development and green infrastructure planning.

7.5 Limitations

Despite the advancements achieved in this research, there are limitations of the models that have been developed due to forest type, climate, region, and less accuracy in the low biomass region of the forestIn dense tropical forests, L-band SAR often saturates at high biomass levels (>150 Mg/ha) due to strong attenuation from thick canopies, limiting sensitivity to biomass variation (Mermoz & Le Toan, 2016). This issue can be mitigated by integrating P-band SAR from ESA's upcoming BIOMASS SAR mission for deeper penetration and LiDAR for accurate vertical structure data. Conversely, in sparse forests, such as those in semi-arid regions, limited canopy cover reduces scattering sensitivity (Singh et al., 2013; Joshi et al., 2017), resulting in higher surface scattering (Mitchard et al., 2011), which can be influenced by surface parameters such as soil moisture, topography, and roughness (Lehmann et al., 2012). In tropical forests, high humidity and soil moisture alter vegetation dielectric properties, affecting SAR backscatter. In temperate forests, seasonal temperature variations impact forest growth cycles, making temperature data critical for accurate temporal biomass estimation (Santoro et al., 2011).

Combining multi-frequency SAR (L-band and C-band) with GEDI LiDAR has significantly improved biomass estimation accuracy in this research. However, these models still rely on high-quality, co-registered datasets. Differences in sensor coverage, resolution, and acquisition timing can introduce discrepancies, particularly in heterogeneous or dynamic forests. Calibration and validation also remain constrained by the limited availability of ground-truth data across diverse forest types. Additional field measurements are essential to refine models and ensure their transferability from sparse to very dense forests for global biomass estimation.

The integration of L-band and S-band SAR data from the upcoming NISAR mission will further enhance biomass estimation by capturing both canopy- and trunk-level scattering interactions. NISAR's global coverage, high temporal resolution, and reduced temporal decorrelation in PolInSAR will enable continuous monitoring of seasonal and phenological changes. This capability will be particularly beneficial in temperate and boreal forests, where dynamic seasonal conditions—such as leaf fall and snow cover—can affect SAR backscatter and reduce model accuracy. Time-series SAR data and InSAR coherence will help address these temporal variations and improve biomass estimation accuracy.

Future research should focus on incorporating environmental parameters—such as soil moisture, temperature, slope, and aspect—into biomass models. Machine learning approaches using multi-sensor data from NISAR, LiDAR, and other remote sensing sources can enhance scalability and accuracy. Integrating these parameters will improve forest monitoring, support conservation efforts, and strengthen global carbon accounting, contributing to climate change mitigation strategies.

7.6 Directions for Future Research

- **Fine-tuning of biomass models:** Biomass models developed using multi-frequency SAR and LiDAR data require further refinement with additional field data to improve their accuracy. Future studies should prioritize the development of an automated pipeline that leverages open-source multi-frequency SAR datasets, such as those expected from the NISAR mission and GEDI LiDAR data, to produce moderate-resolution forest biomass estimates.

- **Enhancing global forest resource assessment** :SAR-based biomass estimates should be incorporated into national forest inventories, particularly in tropical regions with high forest biomass where traditional optical remote sensing techniques face saturation issues. SAR-based biomass estimation techniques can enhance monitoring, reporting, and verification systems under REDD+, aiding in the accurate assessment of carbon stocks and emissions associated with deforestation and forest degradation. The sensitivity of SAR to structural changes makes it ideal for identifying and monitoring selective logging and other subtle forest disturbance events. This method will be useful in supporting the United Nations Decade on Ecosystem Restoration.

- **Below-ground biomass estimation:** There are few studies estimated below-ground biomass (BGB) using remote sensing(Y. Chen et al., 2023; Spawn et al., 2020) in comparison to AGB estimation, which is more accessible to remote sensing techniques. Using remote sensing it is difficult to estimate below-ground biomass, but several indirect methods have been developed to address this limitation. One common approach is the use of the root-to-shoot ratio (RSR) (Marziliano et al., 2015; Nielsen et al., 2021; Sleight et al., 2023), where above-ground biomass estimates from remote sensing are combined with vegetation-specific RSR values to estimate below-ground biomass carbon (BGBC). This method relies on the near-linear relationship between log-transformed AGB and BGB. Another method is applying allometric equations, where remote sensing-derived AGB is used to predict BGB based on established relationships between the two them. However, in many regions, including Indian forests, reliable allometric equations for below-ground biomass are not available, making accurate estimation challenging (Brahma et al., 2021; Chhabra, 2002; Chopra et al., 2023). Integrating multiple data sources, such as optical imagery, LiDAR, SAR, and field measurements, can improve the accuracy of BGB estimation by incorporating diverse vegetation and soil characteristics (Cao et al., 2014). Additionally, vegetation indices derived from remote sensing provide information on vegetation health, productivity, and stress, which may indirectly correlate with BGB. The lack of region-specific allometric equations in areas such as Indian forests highlight the need for further research to enhance model accuracy and reliability. An emerging direction in this field is the use of Synthetic Aperture Radar (SAR) to estimate below-ground biomass through scattering power analysis. SAR, particularly L-band and P-band, has potential for detecting subsurface and soil-root interactions by analyzing volume scattering. Future research should focus on developing models that link SAR scattering mechanisms to root structures, soil moisture, and AGB characteristics, with the aim of improving remote sensing-based estimation of below-ground biomass. Combining SAR-based scattering data with other remote sensing modalities and field observations may lead the way for more robust and scalable estimation techniques.

- **Contribution to climate strategies:** SAR-based biomass research should be integrated into strategies for achieving nationally determined contributions (NDCs) under global climate agreements.

- **Utilizing the European Space Agency (ESA) Biomass mission:** With the launch of the ESA Biomass (P-band) mission, global coverage of tropical forests with tomographic SAR data will provide an opportunity to explore the relationship between TanDEM-X tomogram backscatter and AGB using P-band data for more accurate biomass estimation. Polarimetric SAR tomography (PolTomSAR) combines polarimetry and tomographic SAR techniques, enabling the disentanglement of scattering processes at various forest elevations. This method holds promise for resolving complex forest structures and enhancing biomass estimates.

- **Large-scale applications:** The combined AGB retrieval models developed in this research can be applied to larger regions using digital elevation models and digital surface models as well as open-source Sentinel-1A/B data for cost-effective, scalable biomass estimation.

- **NISAR**: The NASA-ISRO SAR (NISAR) mission, with its dual-frequency (S-band and L-band) capabilities, presents an opportunity to develop AGB estimation models that leverage these complementary datasets. Such models could be integrated into operational systems to generate national AGB inventories. Multi-frequency (S-band and L-band) SAR data in combination with LiDAR information can be processed into operational AGB products for forest monitoring and management. The development of generic methods for biomass estimation using dual-PolSAR and spaceborne LiDAR data will enhance the applicability of these models across different regions and forest types. Incorporation of temporal data from SAR and LiDAR will enable time-series analysis of forest growth, degradation, and recovery. These developments will improve the capacity to track forest health and carbon stock changes over time.

- Future research should focus on the collection of field data across a broad range of forest types for investigation of the dynamics of scattering parameters. Such data will improve model generalizability and clarify the region-specific biomass distribution.

- **Expanding FDI**: This index, which was tested in managed forests in Haldwani, demonstrated significant potential for mapping of disturbance and regrowth. Future research should investigate scattering parameters across various plantation forest types to elucidate these dynamic processes in different forest types. With more extensive ground sample data from diverse forest regions, deep learning algorithms can improve the accuracy of forest biomass estimation and disturbance monitoring.

- **Incorporation of optical data**: As additional field data become available, the models described here can be enhanced through integration of additional variables obtained from optical data sources. At present, the limited availability of field samples constrains the models, as adding more variables may lead to overfitting. Expanded field datasets will help to prevent this issue and broaden the applicability of these models to a variety of forest environments.

Addressing these limitations and pursuing the outlined recommendations would allow the potential of SAR and LiDAR technologies to be fully realized, advancing global efforts toward forest conservation, resource management, and climate change mitigation.

References

Abugre, S., & Sackey, E. K. (2022). Diagnosis of perception of drivers of deforestation using the partial least squares path modeling approach. *Trees, Forests and People*, *8*, 100246. https://doi.org/10.1016/j.tfp.2022.100246

Ainsworth, T. L., Cloude, S. R., & Lee, J. S. (2002). Eigenvector analysis of polarimetric SAR data. *IEEE International Geoscience and Remote Sensing Symposium*, 626–628. https://doi.org/10.1109/IGARSS.2002.1025126

An, W., Cui, Y., & Yang, J. (2010). Three-component model-based decomposition for polarimetric sar data. *IEEE Transactions on Geoscience and Remote Sensing*, *48*(6), 2732–2739. https://doi.org/10.1109/TGRS.2010.2041242

Antropov, O., Rauste, Y., & Hame, T. (2011). Volume scattering modeling in PolSAR decompositions: Study of ALOS PALSAR data over boreal forest. *IEEE Transactions on Geoscience and Remote Sensing*, *49*(10 PART 2), 3838–3848. https://doi.org/10.1109/TGRS.2011.2138146

Arikawa, Y., Osawa, Y., Hatooka, Y., Suzuki, S., & Kankaku, Y. (2010). *Development status of Japanese Advanced Land Observing Satellite-2* (R. Meynart, S. P. Neeck, & H. Shimoda, Eds.; p. 78260B). https://doi.org/10.1117/12.866675

Askne, J. I. H., Dammert, P. B. G., Ulander, L. M. H., & Smith, G. (1997). C-band repeat-pass interferometric SAR observations of the forest. *IEEE Transactions on Geoscience and Remote Sensing*, *35*(1), 25–35. https://doi.org/10.1109/36.551931

Askne, J., & Santoro, M. (2012). *Experiences in Boreal Forest Stem Volume Estimation from Multitemporal C-Band InSAR*. www.intechopen.com

Asner, G. P., Powell, G. V. N., Mascaro, J., Knapp, D. E., Clark, J. K., Jacobson, J., Kennedy-Bowdoin, T., Balaji, A., Paez-Acosta, G., Victoria, E., Secada, L., Valqui, M., & Hughes, R. F. (2010). High-resolution forest carbon stocks and emissions in the Amazon. *Proceedings of the National Academy of Sciences*, *107*(38), 16738–16742. https://doi.org/10.1073/pnas.1004875107

Avtar, R., Kumar, P., Oono, A., Saraswat, C., Dorji, S., & Hlaing, Z. (2017). Potential application of remote sensing in monitoring ecosystem services of forests, mangroves and urban areas. *Geocarto International*, *32*(8), 874–885. https://doi.org/10.1080/10106049.2016.1206974

Avtar, R., Sawada, H., Takeuchi, W., & Singh, G. (2012). Characterization of forests and deforestation in Cambodia using ALOS/PALSAR observation. *Geocarto International*, *27*(2), 119–137. https://doi.org/10.1080/10106049.2011.626081

Avtar, R., Suzuki, R., & Sawada, H. (2014). Natural Forest Biomass Estimation Based on Plantation Information Using PALSAR Data. *PLoS ONE*, *9*(1), e86121. https://doi.org/10.1371/journal.pone.0086121

Avtar, R., Takeuchi, W., & Sawada, H. (2013). Full polarimetric PALSAR-based land cover monitoring in Cambodia for implementation of REDD policies. *International Journal of Digital Earth*, *6*(3), 255–275. https://doi.org/10.1080/17538947.2011.620639

Ban, Y., Zhang, P., Nascetti, A., Bevington, A. R., & Wulder, M. A. (2020). Near Real-Time Wildfire Progression Monitoring with Sentinel-1 SAR Time Series and Deep Learning. *Scientific Reports*, *10*(1), 1322. https://doi.org/10.1038/s41598-019-56967-x

BEAUDOIN, A., LE TOAN, T., GOZE, S., NEZRY, E., LOPES, A., MOUGIN, E., HSU, C. C., HAN, H. C., KONG, J. A., & SHIN, R. T. (1994). Retrieval of forest biomass from SAR data. *International Journal of Remote Sensing*, *15*(14), 2777–2796. https://doi.org/10.1080/01431169408954284

Behera, M. D., Tripathi, P., Mishra, B., Kumar, S., Chitale, V. S., & Behera, S. K. (2016). Above-ground biomass and carbon estimates of Shorea robusta and Tectona grandis forests using QuadPOL ALOS PALSAR data. *Advances in Space Research*, *57*(2), 552–561. https://doi.org/10.1016/j.asr.2015.11.010

Belgiu, M., & Drăguţ, L. (2016). Random forest in remote sensing: A review of applications and future directions. *ISPRS Journal of Photogrammetry and Remote Sensing*, *114*, 24–31. https://doi.org/10.1016/j.isprsjprs.2016.01.011

Berninger, A., Lohberger, S., Stängel, M., & Siegert, F. (2018). SAR-Based Estimation of Above-Ground Biomass and Its Changes in Tropical Forests of Kalimantan Using L- and C-Band. *Remote Sensing*, *10*(6), 831. https://doi.org/10.3390/rs10060831

Boerner, W.-M., Yan, W.-L., Xi, A.-Q., & Yamaguchi, Y. (1992). Basic Concepts of Radar Polarimetry. In *Direct and Inverse Methods in Radar Polarimetry* (pp. 155–245). Springer Netherlands. https://doi.org/10.1007/978-94-010-9243-2_8

Bouvet, A., Mermoz, S., Le Toan, T., Villard, L., Mathieu, R., Naidoo, L., & Asner, G. P. (2018). An above-ground biomass map of African savannahs and woodlands at 25 m resolution derived from ALOS PALSAR. *Remote Sensing of Environment*, *206*, 156–173. https://doi.org/10.1016/j.rse.2017.12.030

Brahma, B., Nath, A. J., Deb, C., Sileshi, G. W., Sahoo, U. K., & Kumar Das, A. (2021). A critical review of forest biomass estimation equations in India. *Trees, Forests and People*, *5*, 100098. https://doi.org/10.1016/j.tfp.2021.100098

Breiman, L. (2001a). Random Forests. *Machine Learning*, *45*(1), 5–32. https://doi.org/10.1023/A:1010933404324

Breiman, L. (2001b). Random Forests. Machine Learning . *Machine Learning*, *45*(1), 5–32. https://doi.org/10.1023/A:1010933404324

Brown, S. (2002). Measuring carbon in forests: current status and future challenges. *Environmental Pollution*, *116*(3), 363–372. https://doi.org/10.1016/S0269-7491(01)00212-3

Campbell, B. M. (2009). Beyond Copenhagen: REDD+, agriculture, adaptation strategies and poverty. In *Global Environmental Change* (Vol. 19, Issue 4, pp. 397–399). https://doi.org/10.1016/j.gloenvcha.2009.07.010

Canadell, J. G., Ciais, P., Cox, P., & Heimann, M. (2004). Quantifying, Understanding and Managing the Carbon Cycle in the Next Decades. *Climatic Change*, *67*(2–3), 147–160. https://doi.org/10.1007/s10584-004-3765-y

Cao, L., Coops, N., Innes, J., Dai, J., & She, G. (2014). Mapping Above- and Below-Ground Biomass Components in Subtropical Forests Using Small-Footprint LiDAR. *Forests*, *5*(6), 1356–1373. https://doi.org/10.3390/f5061356

Cartus, O., & Santoro, M. (2019). Exploring combinations of multi-temporal and multi-frequency radar backscatter observations to estimate above-ground biomass of tropical forest. *Remote Sensing of Environment*, *232*, 111313. https://doi.org/10.1016/j.rse.2019.111313

Cartus, O., Santoro, M., & Kellndorfer, J. (2012). Mapping forest aboveground biomass in the Northeastern United States with ALOS PALSAR dual-polarization L-band. *Remote Sensing of Environment*, *124*, 466–478. https://doi.org/10.1016/j.rse.2012.05.029

Cartus, O., Santoro, M., Wegmuller, U., & Rommen, B. (2017). Estimating total aboveground, stem and branch biomass using multi-frequency SAR. *2017 9th International Workshop on the Analysis of Multitemporal Remote Sensing Images (MultiTemp)*, 1–3. https://doi.org/10.1109/Multi-Temp.2017.8035231

Champion, H. G., & Seth, S. K. (1968). *A REVISED SURVEY OF THE FOREST TYPES OF INDIA*.

Chang, J. G., Shoshany, M., & Oh, Y. (2018). Polarimetric Radar Vegetation Index for Biomass Estimation in Desert Fringe Ecosystems. *IEEE Transactions on Geoscience and Remote Sensing*, *56*(12), 7102–7108. https://doi.org/10.1109/TGRS.2018.2848285

Chave, J., Andalo, C., Brown, S., Cairns, M. A., Chambers, J. Q., Eamus, D., Fölster, H., Fromard, F., Higuchi, N., Kira, T., Lescure, J.-P., Nelson, B. W., Ogawa, H., Puig, H., Riéra, B., & Yamakura, T. (2005). Tree allometry and improved estimation of carbon stocks and balance in tropical forests. *Oecologia*, *145*(1), 87–99. https://doi.org/10.1007/s00442-005-0100-x

Chave, J., Réjou-Méchain, M., Búrquez, A., Chidumayo, E., Colgan, M. S., Delitti, W. B. C., Duque, A., Eid, T., Fearnside, P. M., Goodman, R. C., Henry, M., Martínez-Yrízar, A., Mugasha, W. A., Muller-Landau, H. C., Mencuccini, M., Nelson, B. W., Ngomanda, A., Nogueira, E. M., Ortiz-Malavassi, E., … Vieilledent, G. (2014). Improved allometric models to estimate the aboveground biomass of tropical trees. *Global Change Biology*, *20*(10), 3177–3190. https://doi.org/10.1111/gcb.12629

Chen, S.-W., Wang, X.-S., Xiao, S.-P., & Su, Y. (2018). Urban Damage Mapping Using Fully Polarimetric SAR Data. *2018 Progress in Electromagnetics Research Symposium (PIERS-Toyama)*, 2239–2244. https://doi.org/10.23919/PIERS.2018.8597801

Chen, Y., Feng, X., Fu, B., Ma, H., Zohner, C. M., Crowther, T. W., Huang, Y., Wu, X., & Wei, F. (2023). Maps with 1 km resolution reveal increases in above- and belowground forest biomass carbon pools in China over the past 20 years. *Earth System Science Data*, *15*(2), 897–910. https://doi.org/10.5194/essd-15-897-2023

Chere, Z., Zewdie, W., & Biru, D. (2023). Machine learning for modeling forest canopy height and cover from multi-sensor data in Northwestern Ethiopia. *Environmental Monitoring and Assessment*, *195*(12), 1452. https://doi.org/10.1007/s10661-023-12066-z

Chhabra, A. (2002). Growing stock-based forest biomass estimate for India. *Biomass and Bioenergy*, *22*(3), 187–194. https://doi.org/10.1016/S0961-9534(01)00068-X

Chopra, N., Tewari, L. M., Tewari, A., Wani, Z. A., Asgher, M., Pant, S., Siddiqui, S., & Siddiqua, A. (2023). Estimation of Biomass and Carbon Sequestration Potential of Dalbergia latifolia Roxb. and Melia composita Willd. Plantations in the Tarai Region (India). *Forests*, *14*(3), 646. https://doi.org/10.3390/f14030646

Chowdhury, T. A., Thiel, C., & Schmullius, C. (2014). Growing stock volume estimation from L-band ALOS PALSAR polarimetric coherence in Siberian forest. *Remote Sensing of Environment*, *155*, 129–144. https://doi.org/10.1016/j.rse.2014.05.007

Clark, D. B., & Clark, D. A. (2000). Landscape-scale variation in forest structure and biomass in a tropical rain forest. *Forest Ecology and Management*, *137*(1–3), 185–198. https://doi.org/10.1016/S0378-1127(99)00327-8

Cloude, R., & Pottier, E. (1996). view of Target Decomposition ar Polarimetry. In *IEEE TRANSACTIONS ON GEOSCIENCE AND REMOTE SENSING* (Vol. 34, Issue 2).

Cloude, S. R. (1992). Lie Groups in Electromagnetic Wave Propagation and Scattering. *Journal of Electromagnetic Waves and Applications*, *6*(7), 947–974. https://doi.org/10.1163/156939392X01552

Cloude, S. R., & Pottier, E. (1996). A review of target decomposition theorems in radar polarimetry. *IEEE Transactions on Geoscience and Remote Sensing*, *34*(2), 498–518. https://doi.org/10.1109/36.485127

Curran, P. J., & Atkinson, P. M. (1998). Geostatistics and remote sensing. *Progress in Physical Geography: Earth and Environment*, *22*(1), 61–78. https://doi.org/10.1177/030913339802200103

Deng, J., Zhou, P., Li, M., Li, H., & Chen, S. (2023). Quad-Pol SAR Data Reconstruction from Dual-Pol SAR Mode Based on a Multiscale Feature Aggregation Network. *Remote Sensing*, *15*(17), 4182. https://doi.org/10.3390/rs15174182

Deng, S., Katoh, M., Guan, Q., Yin, N., & Li, M. (2014). Estimating forest aboveground biomass by combining ALOS PALSAR and WorldView-2 data: A case study at Purple Mountain National Park, Nanjing, China. *Remote Sensing*, *6*(9), 7878–7910. https://doi.org/10.3390/rs6097878

Dhargay, S., Lyell, C. S., Brown, T. P., Inbar, A., Sheridan, G. J., & Lane, P. N. J. (2022a). Performance of GEDI Space-Borne LiDAR for Quantifying Structural Variation in the Temperate Forests of South-Eastern Australia. *Remote Sensing*, *14*(15). https://doi.org/10.3390/rs14153615

Dhargay, S., Lyell, C. S., Brown, T. P., Inbar, A., Sheridan, G. J., & Lane, P. N. J. (2022b). Performance of GEDI Space-Borne LiDAR for Quantifying Structural Variation in the Temperate Forests of South-Eastern Australia. *Remote Sensing*, *14*(15). https://doi.org/10.3390/rs14153615

Dobson, M. C., Ulaby, F. T., LeToan, T., Beaudoin, A., Kasischke, E. S., & Christensen, N. (1992). Dependence of radar backscatter on coniferous forest biomass. *IEEE Transactions on Geoscience and Remote Sensing*, *30*(2), 412–415. https://doi.org/10.1109/36.134090

Dobson, M. C., Ulaby, F. T., Pierce, L. E., Sharik, T. L., Bergen, K. M., Kellndorfer, J., Kendra, J. R., Li, E., Lin, Y. C., Nashashibi, A., Sarabandi, K., & Siqueira, P. (1995). Estimation of forest biophysical characteristics in Northern Michigan with SIR-C/X-SAR. *IEEE Transactions on Geoscience and Remote Sensing*, *33*(4), 877–895. https://doi.org/10.1109/36.406674

Du, P., Samat, A., Waske, B., Liu, S., & Li, Z. (2015). Random Forest and Rotation Forest for fully polarized SAR image classification using polarimetric and spatial features. *ISPRS*

Journal of Photogrammetry and Remote Sensing, *105*, 38–53. https://doi.org/10.1016/j.isprsjprs.2015.03.002

Dubayah, R., Blair, J. B., Goetz, S., Fatoyinbo, L., Hansen, M., Healey, S., Hofton, M., Hurtt, G., Kellner, J., Luthcke, S., Armston, J., Tang, H., Duncanson, L., Hancock, S., Jantz, P., Marselis, S., Patterson, P. L., Qi, W., & Silva, C. (2020). The Global Ecosystem Dynamics Investigation: High-resolution laser ranging of the Earth's forests and topography. *Science of Remote Sensing*, *1*, 100002. https://doi.org/10.1016/j.srs.2020.100002

Duncanson, L., Kellner, J. R., Armston, J., Dubayah, R., Minor, D. M., Hancock, S., Healey, S. P., Patterson, P. L., Saarela, S., Marselis, S., Silva, C. E., Bruening, J., Goetz, S. J., Tang, H., Hofton, M., Blair, B., Luthcke, S., Fatoyinbo, L., Abernethy, K., … Zgraggen, C. (2022). Aboveground biomass density models for NASA's Global Ecosystem Dynamics Investigation (GEDI) lidar mission. *Remote Sensing of Environment*, *270*, 112845. https://doi.org/10.1016/j.rse.2021.112845

Duncanson, L., Neuenschwander, A., Hancock, S., Thomas, N., Fatoyinbo, T., Simard, M., Silva, C. A., Armston, J., Luthcke, S. B., Hofton, M., Kellner, J. R., & Dubayah, R. (2020). Biomass estimation from simulated GEDI, ICESat-2 and NISAR across environmental gradients in Sonoma County, California. *Remote Sensing of Environment*, *242*, 111779. https://doi.org/10.1016/j.rse.2020.111779

Ellison, D., Morris, C. E., Locatelli, B., Sheil, D., Cohen, J., Murdiyarso, D., Gutierrez, V., Noordwijk, M. van, Creed, I. F., Pokorny, J., Gaveau, D., Spracklen, D. V., Tobella, A. B., Ilstedt, U., Teuling, A. J., Gebrehiwot, S. G., Sands, D. C., Muys, B., Verbist, B., … Sullivan, C. A. (2017). Trees, forests and water: Cool insights for a hot world. *Global Environmental Change*, *43*, 51–61. https://doi.org/10.1016/j.gloenvcha.2017.01.002

Englhart, S., Keuck, V., & Siegert, F. (2011). Aboveground biomass retrieval in tropical forests — The potential of combined X- and L-band SAR data use. *Remote Sensing of Environment*, *115*(5), 1260–1271. https://doi.org/10.1016/j.rse.2011.01.008

Erdogan Erten, G., Yavuz, M., & Deutsch, C. V. (2022). Combination of Machine Learning and Kriging for Spatial Estimation of Geological Attributes. *Natural Resources Research*, *31*(1), 191–213. https://doi.org/10.1007/s11053-021-10003-w

FAO. (2020). *The State of the World's Forests 2020*. FAO and UNEP. https://doi.org/10.4060/ca8642en

FAO (Ed.). (2016). *FORESTS AND AGRICULTURE: LAND-USE CHALLENGES AND OPPORTUNITIES STATE OF THE WORLD'S FORESTS*.

Farr, T. G., Rosen, P. A., Caro, E., Crippen, R., Duren, R., Hensley, S., Kobrick, M., Paller, M., Rodriguez, E., Roth, L., Seal, D., Shaffer, S., Shimada, J., Umland, J., Werner, M., Oskin, M., Burbank, D., & Alsdorf, D. (2007). The Shuttle Radar Topography Mission. *Reviews of Geophysics*, *45*(2). https://doi.org/10.1029/2005RG000183

Fatoyinbo, T., Armston, J., Simard, M., Saatchi, S., Denbina, M., Lavalle, M., Hofton, M., Tang, H., Marselis, S., Pinto, N., Hancock, S., Hawkins, B., Duncanson, L., Blair, B., Hansen, C., Lou, Y., Dubayah, R., Hensley, S., Silva, C., … Hibbard, K. (2021). The NASA AfriSAR campaign: Airborne SAR and lidar measurements of tropical forest structure and biomass in support of current and future space missions. *Remote Sensing of Environment*, *264*. https://doi.org/10.1016/j.rse.2021.112533

Fayad, I., Ienco, D., Baghdadi, N., Gaetano, R., Alvares, C. A., Stape, J. L., Ferraço Scolforo, H., & Le Maire, G. (2021). A CNN-based approach for the estimation of canopy heights and wood volume from GEDI waveforms. *Remote Sensing of Environment*, *265*. https://doi.org/10.1016/j.rse.2021.112652

Filipponi, F. (2019). Sentinel-1 GRD Preprocessing Workflow. *3rd International Electronic Conference on Remote Sensing*, 11. https://doi.org/10.3390/ECRS-3-06201

Foody, G. M., Boyd, D. S., & Cutler, M. E. J. (2003). Predictive relations of tropical forest biomass from Landsat TM data and their transferability between regions. *Remote Sensing of Environment*, *85*(4), 463–474. https://doi.org/10.1016/S0034-4257(03)00039-7

Forest Survey of India. (1996). *Volume Equations for Forests of India, Nepal, and Bhutan*. Forest Survey of India, Ministry of Environment \& Forests, Government of India.

Freeman, A., & Durden, S. L. (1998a). A three-component scattering model for polarimetric SAR data. *IEEE Transactions on Geoscience and Remote Sensing*, *36*(3), 963–973. https://doi.org/10.1109/36.673687

Freeman, A., & Durden, S. L. (1998b). A three-component scattering model for polarimetric SAR data. *IEEE Transactions on Geoscience and Remote Sensing*, *36*(3), 963–973. https://doi.org/10.1109/36.673687

Freeman, A., Member, S., & Durden, S. L. (1998). A Three-Component Scattering Model for Polarimetric SAR Data. In *IEEE TRANSACTIONS ON GEOSCIENCE AND REMOTE SENSING* (Vol. 36, Issue 3).

Ghasemi, N., Sahebi, R., & Mohammadzadeh, A. (2011). A review on biomass estimation methods using synthetic aperture radar data. In *INTERNATIONAL JOURNAL OF GEOMATICS AND GEOSCIENCES* (Vol. 1, Issue 4).

Ghosh, S. M., & Behera, M. D. (2018). Aboveground biomass estimation using multi-sensor data synergy and machine learning algorithms in a dense tropical forest. *Applied Geography*, *96*, 29–40. https://doi.org/10.1016/j.apgeog.2018.05.011

Gibbs, H. K., Brown, S., Niles, J. O., & Foley, J. A. (2007a). Monitoring and estimating tropical forest carbon stocks: making REDD a reality. *Environmental Research Letters*, *2*(4), 045023. https://doi.org/10.1088/1748-9326/2/4/045023

Gibbs, H. K., Brown, S., Niles, J. O., & Foley, J. A. (2007b). Monitoring and estimating tropical forest carbon stocks: Making REDD a reality. *Environmental Research Letters*, *2*(4). https://doi.org/10.1088/1748-9326/2/4/045023

Gibbs, H. K., Brown, S., Niles, J. O., & Foley, J. A. (2007c). Monitoring and estimating tropical forest carbon stocks: making REDD a reality. *Environmental Research Letters*, *2*(4), 045023. https://doi.org/10.1088/1748-9326/2/4/045023

Gleason, C. J., & Im, J. (2012). Forest biomass estimation from airborne LiDAR data using machine learning approaches. *Remote Sensing of Environment*, *125*, 80–91. https://doi.org/10.1016/j.rse.2012.07.006

Global Biodiversity Outlook 5. (n.d.).

Goers, L., Lawson, J., & Garen, E. (2012). Economic Drivers of Tropical Deforestation for Agriculture. In *Managing Forest Carbon in a Changing Climate* (pp. 305–320). Springer Netherlands. https://doi.org/10.1007/978-94-007-2232-3_14

Goetz, S. J., Hansen, M., Houghton, R. A., Walker, W., Laporte, N., & Busch, J. (2015). Measurement and monitoring needs, capabilities and potential for addressing reduced emissions from deforestation and forest degradation under REDD+. *Environmental Research Letters*, *10*(12), 123001. https://doi.org/10.1088/1748-9326/10/12/123001

Guerra-Hernández, J., & Pascual, A. (2021). Using GEDI lidar data and airborne laser scanning to assess height growth dynamics in fast-growing species: a showcase in Spain. *Forest Ecosystems*, *8*(1), 14. https://doi.org/10.1186/s40663-021-00291-2

Guoqing Sun, Rocchio, L., Masek, J., Williams, D., & Ranson, K. J. (2002). Characterization of forest recovery from fire using Landsat and SAR data. *IEEE International Geoscience and Remote Sensing Symposium*, 1076–1078. https://doi.org/10.1109/IGARSS.2002.1025780

Han, W., Fu, H., Zhu, J., Wang, C., & Xie, Q. (2022). Polarimetric SAR Decomposition by Incorporating a Rotated Dihedral Scattering Model. *IEEE Geoscience and Remote Sensing Letters*, *19*. https://doi.org/10.1109/LGRS.2020.3035567

Hansen, J. N., Mitchard, E. T. A., & King, S. (2020). Assessing Forest/Non-Forest Separability Using Sentinel-1 C-Band Synthetic Aperture Radar. *Remote Sensing*, *12*(11), 1899. https://doi.org/10.3390/rs12111899

Hansen, M. C., Potapov, P. V., Moore, R., Hancher, M., Turubanova, S. A., Tyukavina, A., Thau, D., Stehman, S. V., Goetz, S. J., Loveland, T. R., Kommareddy, A., Egorov, A., Chini, L., Justice, C. O., & Townshend, J. R. G. (2013). High-Resolution Global Maps of 21st-Century Forest Cover Change. *Science*, *342*(6160), 850–853. https://doi.org/10.1126/science.1244693

Hayashi, M., Motohka, T., & Sawada, Y. (2019). Aboveground Biomass Mapping Using ALOS-2/PALSAR-2 Time-Series Images for Borneo's Forest. *IEEE Journal of Selected Topics in Applied Earth Observations and Remote Sensing*, *12*(12), 5167–5177. https://doi.org/10.1109/JSTARS.2019.2957549

Henderson, F. M. and L. A. J. (1998). Principles and Applications of Imaging Radar. Manual of Remote Sensing. *John Wiley and Sons*.

Hong, H. T. C., Avtar, R., & Fujii, M. (2019). Monitoring changes in land use and distribution of mangroves in the southeastern part of the Mekong River Delta, Vietnam. *Tropical Ecology*, *60*(4), 552–565. https://doi.org/10.1007/s42965-020-00053-1

Hosseiny, B., Zaboli, M., & Homayouni, S. (2024). Forest Change Mapping using Multi-Source Satellite SAR, Optical, and LiDAR Remote Sensing Data. *ISPRS Annals of the Photogrammetry, Remote Sensing and Spatial Information Sciences*, *X-4–2024*, 163–168. https://doi.org/10.5194/isprs-annals-X-4-2024-163-2024

Houghton, R. A., Hall, F., & Goetz, S. J. (2009). Importance of biomass in the global carbon cycle. *Journal of Geophysical Research: Biogeosciences*, *114*(G2). https://doi.org/10.1029/2009JG000935

Huang, H., Liu, C., Wang, X., Zhou, X., & Gong, P. (2019). Integration of multi-resource remotely sensed data and allometric models for forest aboveground biomass estimation in China. *Remote Sensing of Environment*, *221*, 225–234. https://doi.org/10.1016/j.rse.2018.11.017

Huang, W., Sun, G., Ni, W., Zhang, Z., & Dubayah, R. (2015a). Sensitivity of Multi-Source SAR Backscatter to Changes in Forest Aboveground Biomass. *Remote Sensing*, *7*(8), 9587–9609. https://doi.org/10.3390/rs70809587

Huang, W., Sun, G., Ni, W., Zhang, Z., & Dubayah, R. (2015b). Sensitivity of Multi-Source SAR Backscatter to Changes in Forest Aboveground Biomass. *Remote Sensing*, *7*(8), 9587–9609. https://doi.org/10.3390/rs70809587

Hurwitz, H., & Jones, R. C. (1941). A New Calculus for the Treatment of Optical SystemsII Proof of Three General Equivalence Theorems. *Journal of the Optical Society of America*, *31*(7), 493. https://doi.org/10.1364/JOSA.31.000493

Imhoff, M. L. (1995). Radar backscatter and biomass saturation: ramifications for global biomass inventory. *IEEE Transactions on Geoscience and Remote Sensing*, *33*(2), 511–518. https://doi.org/10.1109/TGRS.1995.8746034

Imhoff, M., Story, M., Vermillion, C., Khan, F., & Polcyn, F. (1986). Forest Canopy Characterization and Vegetation Penetration Assessment with Space-Borne Radar. *IEEE*

Transactions on Geoscience and Remote Sensing, *GE-24*(4), 535–542. https://doi.org/10.1109/TGRS.1986.289668

Jennings, S. (1999). Assessing forest canopies and understorey illumination: canopy closure, canopy cover and other measures. *Forestry*, *72*(1), 59–74. https://doi.org/10.1093/forestry/72.1.59

Jha, C. S., Madugundu, R., Nizalapur, V., & Jha, C. S. (2010). Estimation of above ground biomass in Indian tropical forested area using multi-frequency DLR-ESAR data Estimation of above ground biomass in Indian tropical forested area using multifrequency DLRESAR data. In *INTERNATIONAL JOURNAL OF GEOMATICS AND GEOSCIENCES* (Vol. 1, Issue 2). https://www.researchgate.net/publication/215519592

Ji, Y., Huang, J., Ju, Y., Guo, S., & Yue, C. (2020a). Forest structure dependency analysis of L-band SAR backscatter. *PeerJ*, *8*, e10055. https://doi.org/10.7717/peerj.10055

Ji, Y., Huang, J., Ju, Y., Guo, S., & Yue, C. (2020b). Forest structure dependency analysis of L-band SAR backscatter. *PeerJ*, *8*, e10055. https://doi.org/10.7717/peerj.10055

Ji, Y., Wang, L., Zhang, W., Marino, A., Wang, M., Ma, J., Shi, J., Jing, Q., Zhang, F., Zhao, H., Huang, G., Yang, F., & Wang, G. (2024). Forest above-ground biomass estimation using X, C, L, and P band SAR polarimetric observations and different inversion models. *International Journal of Digital Earth*, *17*(1). https://doi.org/10.1080/17538947.2024.2310730

Joshi, N., Mitchard, E. T. A., Brolly, M., Schumacher, J., Fernández-Landa, A., Johannsen, V. K., Marchamalo, M., & Fensholt, R. (2017). Understanding 'saturation' of radar signals over forests. *Scientific Reports*, *7*(1), 3505. https://doi.org/10.1038/s41598-017-03469-3

Joshi, N., Mitchard, E. T., Woo, N., Torres, J., Moll-Rocek, J., Ehammer, A., Collins, M., Jepsen, M. R., & Fensholt, R. (2015). Mapping dynamics of deforestation and forest degradation in tropical forests using radar satellite data. *Environmental Research Letters*, *10*(3), 034014. https://doi.org/10.1088/1748-9326/10/3/034014

Kauppi, P. E., Ausubel, J. H., Fang, J., Mather, A. S., Sedjo, R. A., & Waggoner, P. E. (2006). Returning forests analyzed with the forest identity. *Proceedings of the National Academy of Sciences*, *103*(46), 17574–17579. https://doi.org/10.1073/pnas.0608343103

Kennaugh, E. (1951). *Effects of the type of polarization on echo characteristics*. Ohio State University.

Khati, U., & Singh, G. (2022). Combining L-band Synthetic Aperture Radar backscatter and TanDEM-X canopy height for forest aboveground biomass estimation. *Frontiers in Forests and Global Change*, *5*. https://doi.org/10.3389/ffgc.2022.918408

Khati, U., Singh, G., & Ferro-Famil, L. (2017). Analysis of seasonal effects on forest parameter estimation of Indian deciduous forest using TerraSAR-X PolInSAR acquisitions. *Remote Sensing of Environment*, *199*, 265–276. https://doi.org/10.1016/j.rse.2017.07.019

Khati, U., Singh, G., & Kumar, S. (2018). Potential of space-borne polinsar for forest canopy height estimation over India - A case study using fully polarimetric L-, C-, and X-Band SAR Data. *IEEE Journal of Selected Topics in Applied Earth Observations and Remote Sensing*, *11*(7), 2406–2416. https://doi.org/10.1109/JSTARS.2018.2835388

Kobayashi, S., Omura, Y., Sanga-Ngoie, K., Widyorini, R., Kawai, S., Supriadi, B., & Yamaguchi, Y. (2012). Characteristics of Decomposition Powers of L-Band Multi-Polarimetric SAR in Assessing Tree Growth of Industrial Plantation Forests in the Tropics. *Remote Sensing*, *4*(10), 3058–3077. https://doi.org/10.3390/rs4103058

Kobayashi, S., Omura, Y., Sanga-Ngoie, K., Yamaguchi, Y., Widyorini, R., Fujita, M. S., Supriadi, B., & Kawai, S. (2015). Yearly Variation of Acacia Plantation Forests Obtained by Polarimetric Analysis of ALOS PALSAR Data. *IEEE Journal of Selected Topics in Applied Earth Observations and Remote Sensing*, *8*(11), 5294–5304. https://doi.org/10.1109/JSTARS.2015.2487503

Krogager, E. (1990). New decomposition of the radar target scattering matrix. *Electronics Letters*, *26*(18), 1525. https://doi.org/10.1049/el:19900979

Kumar, S., Pandey, U., Kushwaha, S. P., Chatterjee, R. S., & Bijker, W. (2012). Aboveground biomass estimation of tropical forest from Envisat advanced synthetic aperture radar data using modeling approach. *Journal of Applied Remote Sensing*, *6*(1), 063588. https://doi.org/10.1117/1.JRS.6.063588

Kuplich, T. M., Curran, P. J., & Atkinson, P. M. (2005). Relating SAR image texture to the biomass of regenerating tropical forests. *International Journal of Remote Sensing*, *26*(21), 4829–4854. https://doi.org/10.1080/01431160500239107

Kushwaha, S. P. S., Nandy, S., Watham, T., Kushwaha, S., Nandy, S., Patel, N. R., & Ghosh, S. (2016). Forest carbon stock assessment at Barkot Flux tower Site (BFS) using field inventory, Landsat-8 OLI data and geostatistical techniques. In *International Journal of Multidisciplinary Research and Development*. www.allsubjectjournal.com

Lausch, A., Erasmi, S., King, D., Magdon, P., & Heurich, M. (2016). Understanding Forest Health with Remote Sensing -Part I—A Review of Spectral Traits, Processes and Remote-Sensing Characteristics. *Remote Sensing*, *8*(12), 1029. https://doi.org/10.3390/rs8121029

Lausch, A., Erasmi, S., King, D., Magdon, P., & Heurich, M. (2017). Understanding Forest Health with Remote Sensing-Part II—A Review of Approaches and Data Models. *Remote Sensing*, *9*(2), 129. https://doi.org/10.3390/rs9020129

Lavalle, M. (2017). A new automated algorithm for detecting forest disturbances with the dual-polarimetric SAR alpha angle. *2017 IEEE International Geoscience and Remote Sensing Symposium (IGARSS)*, 5299–5302. https://doi.org/10.1109/IGARSS.2017.8128200

Lavalle, M., & Hensley, S. (2015). Extraction of Structural and Dynamic Properties of Forests From Polarimetric-Interferometric SAR Data Affected by Temporal Decorrelation. *IEEE Transactions on Geoscience and Remote Sensing*, *53*(9), 4752–4767. https://doi.org/10.1109/TGRS.2015.2409066

Lavalle, M., & Khun, K. (2014). Three-Baseline InSAR Estimation of Forest Height. *IEEE Geoscience and Remote Sensing Letters*, *11*(10), 1737–1741. https://doi.org/10.1109/LGRS.2014.2307583

Le Toan, T., Beaudoin, A., Riom, J., & Guyon, D. (1992). Relating forest biomass to SAR data. *IEEE Transactions on Geoscience and Remote Sensing*, *30*(2), 403–411. https://doi.org/10.1109/36.134089

Le Toan, T., Quegan, S., Davidson, M. W. J., Balzter, H., Paillou, P., Papathanassiou, K., Plummer, S., Rocca, F., Saatchi, S., Shugart, H., & Ulander, L. (2011). The BIOMASS mission:

Mapping global forest biomass to better understand the terrestrial carbon cycle. *Remote Sensing of Environment*, *115*(11), 2850–2860. https://doi.org/10.1016/j.rse.2011.03.020

Lee, Ainsworth, T. L., & Wang, Y. (2011). Recent advances in scattering model-based decompositions: an overview. *IEEE International Geoscience and Remote Sensing Symposium.*, 9–12.

Lee, J., & Pottier, E. (2017). *Polarimetric Radar Imaging: From Basics to Applications. Optical Science and Engineering.* . CRC Press.

Lee, J. S., Jurkevich, L., Dewaele, P., Wambacq, P., & Oosterlinck, A. (1994). Speckle filtering of synthetic aperture radar images: A review. *Remote Sensing Reviews*, *8*(4), 313–340. https://doi.org/10.1080/02757259409532206

Lefsky, M. A. (2010). A global forest canopy height map from the Moderate Resolution Imaging Spectroradiometer and the Geoscience Laser Altimeter System. *Geophysical Research Letters*, *37*(15). https://doi.org/10.1029/2010GL043622

Lefsky, M. A., Cohen, W. B., Harding, D. J., Parker, G. G., Acker, S. A., & Gower, S. T. (2002). Lidar remote sensing of above-ground biomass in three biomes. *Global Ecology and Biogeography*, *11*(5), 393–399. https://doi.org/10.1046/j.1466-822x.2002.00303.x

Lefsky, M. A., Cohen, W. B., Parker, G. G., & Harding, D. J. (2002). Lidar Remote Sensing for Ecosystem Studies: Lidar, an emerging remote sensing technology that directly measures the three-dimensional distribution of plant canopies, can accurately estimate vegetation structural attributes and should be of particular interest to forest, landscape, and global ecologists. *BioScience*, *52*(1), 19–30. https://doi.org/10.1641/0006-3568(2002)052[0019:LRSFES]2.0.CO;2

Lehmann, E. A., Caccetta, P. A., Zhou, Z.-S., McNeill, S. J., Wu, X., & Mitchell, A. L. (2012). Joint Processing of Landsat and ALOS-PALSAR Data for Forest Mapping and Monitoring. *IEEE Transactions on Geoscience and Remote Sensing*, *50*(1), 55–67. https://doi.org/10.1109/TGRS.2011.2171495

Lei, Y., Lucas, R., Siqueira, P., Schmidt, M., & Treuhaft, R. (2018). Detection of Forest Disturbance With Spaceborne Repeat-Pass SAR Interferometry. *IEEE Transactions on*

Geoscience and Remote Sensing, *56*(4), 2424–2439. https://doi.org/10.1109/TGRS.2017.2780158

Liu, X., Su, Y., Hu, T., Yang, Q., Liu, B., Deng, Y., Tang, H., Tang, Z., Fang, J., & Guo, Q. (2022). Neural network guided interpolation for mapping canopy height of China's forests by integrating GEDI and ICESat-2 data. *Remote Sensing of Environment*, *269*. https://doi.org/10.1016/j.rse.2021.112844

Louppe, G., Wehenkel, L., Sutera, A., & Geurts, P. (2013). *Understanding variable importances in Forests of randomized trees*. https://www.researchgate.net/publication/264046801

Lu, D. (2006). The potential and challenge of remote sensing-based biomass estimation. *International Journal of Remote Sensing*, *27*(7), 1297–1328. https://doi.org/10.1080/01431160500486732

Lucas, R., Armston, J., Fairfax, R., Fensham, R., Accad, A., Carreiras, J., Kelley, J., Bunting, P., Clewley, D., Bray, S., Metcalfe, D., Dwyer, J., Bowen, M., Eyre, T., Laidlaw, M., & Shimada, M. (2010). An Evaluation of the ALOS PALSAR L-Band Backscatter—Above Ground Biomass Relationship Queensland, Australia: Impacts of Surface Moisture Condition and Vegetation Structure. *IEEE Journal of Selected Topics in Applied Earth Observations and Remote Sensing*, *3*(4), 576–593. https://doi.org/10.1109/JSTARS.2010.2086436

Lucas, R. M., Cronin, N., Lee, A., Moghaddam, M., Witte, C., & Tickle, P. (2006). Empirical relationships between AIRSAR backscatter and LiDAR-derived forest biomass, Queensland, Australia. *Remote Sensing of Environment*, *100*(3), 407–425. https://doi.org/10.1016/j.rse.2005.10.019

Luckman, A. (1997). A study of the relationship between radar backscatter and regenerating tropical forest biomass for spaceborne SAR instruments. *Remote Sensing of Environment*, *60*(1), 1–13. https://doi.org/10.1016/S0034-4257(96)00121-6

Luo, H., Yue, C., Wang, N., Luo, G., & Chen, S. (2022). Correcting Underestimation and Overestimation in PolInSAR Forest Canopy Height Estimation Using Microwave Penetration Depth. *Remote Sensing*, *14*(23). https://doi.org/10.3390/rs14236145

Maghsoudi, Y., Collins, M. J., & Leckie, D. G. (2013). Radarsat-2 Polarimetric SAR Data for Boreal Forest Classification Using SVM and a Wrapper Feature Selector. *IEEE Journal of Selected Topics in Applied Earth Observations and Remote Sensing*, *6*(3), 1531–1538. https://doi.org/10.1109/JSTARS.2013.2259219

Maitra, S., Gartley, M. G., Faulring, J., & Kerekes, J. P. (2013). Characterization of basic scattering mechanisms using laboratory based polarimetric synthetic aperture radar imaging. *2013 IEEE International Geoscience and Remote Sensing Symposium - IGARSS*, 4479–4482. https://doi.org/10.1109/IGARSS.2013.6723830

Makhado, R. A., Saidi, A. T., Mantlana, B. K., & Mwayafu, M. D. (2011). Challenges of reducing emissions from deforestation and forest degradation (REDD+) on the African continent. *South African Journal of Science*, *107*(9/10). https://doi.org/10.4102/sajs.v107i9/10.615

Marziliano, P. A., Lafortezza, R., Medicamento, U., Lorusso, L., Giannico, V., Colangelo, G., & Sanesi, G. (2015). Estimating belowground biomass and root/shoot ratio of Phillyrea latifolia L. in the Mediterranean forest landscapes. *Annals of Forest Science*, *72*(5), 585–593. https://doi.org/10.1007/s13595-015-0486-5

Merchant, M. A., Adams, J. R., Berg, A. A., Baltzer, J. L., Quinton, W. L., & Chasmer, L. E. (2017). Contributions of C-Band SAR Data and Polarimetric Decompositions to Subarctic Boreal Peatland Mapping. *IEEE Journal of Selected Topics in Applied Earth Observations and Remote Sensing*, *10*(4), 1467–1482. https://doi.org/10.1109/JSTARS.2016.2621043

Mermoz, S., & Le Toan, T. (2016). Forest Disturbances and Regrowth Assessment Using ALOS PALSAR Data from 2007 to 2010 in Vietnam, Cambodia and Lao PDR. *Remote Sensing*, *8*(3), 217. https://doi.org/10.3390/rs8030217

Mermoz, S., Réjou-Méchain, M., Villard, L., Le Toan, T., Rossi, V., & Gourlet-Fleury, S. (2015). Decrease of L-band SAR backscatter with biomass of dense forests. *Remote Sensing of Environment*, *159*, 307–317. https://doi.org/10.1016/j.rse.2014.12.019

Metz, B., Meyer, L., & Bosch, P. (2007). Climate change 2007 mitigation of climate change. In *Climate Change 2007 Mitigation of Climate Change* (Vol. 9780521880114). Cambridge University Press. https://doi.org/10.1017/CBO9780511546013

Miettinen, J., Stibig, H.-J., & Achard, F. (2014). Remote sensing of forest degradation in Southeast Asia—Aiming for a regional view through 5–30 m satellite data. *Global Ecology and Conservation*, *2*, 24–36. https://doi.org/10.1016/j.gecco.2014.07.007

Mishra, V. N., Prasad, R., Rai, P. K., Vishwakarma, A. K., & Arora, A. (2019). Performance evaluation of textural features in improving land use/land cover classification accuracy of heterogeneous landscape using multi-sensor remote sensing data. *Earth Science Informatics*, *12*(1), 71–86. https://doi.org/10.1007/s12145-018-0369-z

Mitchard, E. T. A., Saatchi, S. S., Woodhouse, I. H., Nangendo, G., Ribeiro, N. S., Williams, M., Ryan, C. M., Lewis, S. L., Feldpausch, T. R., & Meir, P. (2009a). Using satellite radar backscatter to predict above-ground woody biomass: A consistent relationship across four different African landscapes. *Geophysical Research Letters*, *36*(23). https://doi.org/10.1029/2009GL040692

Mitchard, E. T. A., Saatchi, S. S., Woodhouse, I. H., Nangendo, G., Ribeiro, N. S., Williams, M., Ryan, C. M., Lewis, S. L., Feldpausch, T. R., & Meir, P. (2009b). Using satellite radar backscatter to predict above-ground woody biomass: A consistent relationship across four different African landscapes. *Geophysical Research Letters*, *36*(23). https://doi.org/10.1029/2009GL040692

Mitchard, E. T. A., Saatchi, S. S., Woodhouse, I. H., Nangendo, G., Ribeiro, N. S., Williams, M., Ryan, C. M., Lewis, S. L., Feldpausch, T. R., & Meir, P. (2009c). Using satellite radar backscatter to predict above-ground woody biomass: A consistent relationship across four different African landscapes. *Geophysical Research Letters*, *36*(23). https://doi.org/10.1029/2009GL040692

Mitchell, A. L., Tapley, I., Milne, A. K., Williams, M. L., Zhou, Z.-S., Lehmann, E., Caccetta, P., Lowell, K., & Held, A. (2014). C- and L-band SAR interoperability: Filling the gaps in continuous forest cover mapping in Tasmania. *Remote Sensing of Environment*, *155*, 58–68. https://doi.org/10.1016/j.rse.2014.02.020

Moreira, A., Prats-Iraola, P., Younis, M., Krieger, G., Hajnsek, I., & Papathanassiou, K. P. (2013). A tutorial on synthetic aperture radar. *IEEE Geoscience and Remote Sensing Magazine*, *1*(1), 6–43. https://doi.org/10.1109/MGRS.2013.2248301

Mullissa, A., Saatchi, S., Dalagnol, R., Erickson, T., Provost, N., Osborn, F., Ashary, A., Moon, V., & Melling, D. (2024). LUCA: A Sentinel-1 SAR-Based Global Forest Land Use Change Alert. *Remote Sensing*, *16*(12), 2151. https://doi.org/10.3390/rs16122151

Munro, P. R. T. (2011). Polarisation: Applications in Remote Sensing, by Shane Cloude. *Contemporary Physics*, *52*(4), 366–367. https://doi.org/10.1080/00107514.2011.558918

Musthafa, M., & Singh, G. (2022a). Improving Forest Above-Ground Biomass Retrieval Using Multi-Sensor L- and C- Band SAR Data and Multi-Temporal Spaceborne LiDAR Data. *Frontiers in Forests and Global Change*, *5*. https://doi.org/10.3389/ffgc.2022.822704

Musthafa, M., & Singh, G. (2022b). Improving Forest Above-Ground Biomass Retrieval Using Multi-Sensor L- and C- Band SAR Data and Multi-Temporal Spaceborne LiDAR Data. *Frontiers in Forests and Global Change*, *5*. https://doi.org/10.3389/ffgc.2022.822704

Mutanga, O. (2016). *Remote sensing of aboveground forest biomass: A review Spatial Assessment and Monitoring of Land Use/Land Cover Change and Erosion Vulnerability in Asejire, Southwest, Nigeria View project Remote sensing of water use and water stress in African savanna ecosystem from local to regional scale: Implications for land productivity View project*. www.tropecol.com

Mutanga, O., & Skidmore, A. K. (2004). Hyperspectral band depth analysis for a better estimation of grass biomass (Cenchrus ciliaris) measured under controlled laboratory conditions. *International Journal of Applied Earth Observation and Geoinformation*, *5*(2), 87–96. https://doi.org/10.1016/j.jag.2004.01.001

Naidoo, L., Mathieu, R., Main, R., Kleynhans, W., Wessels, K., Asner, G., & Leblon, B. (2015). Savannah woody structure modelling and mapping using multi-frequency (X-, C- and L-band) Synthetic Aperture Radar data. *ISPRS Journal of Photogrammetry and Remote Sensing*, *105*, 234–250. https://doi.org/10.1016/j.isprsjprs.2015.04.007

Nandy, S., Singh, R., Ghosh, S., Watham, T., Kushwaha, S. P. S., Kumar, A. S., & Dadhwal, V. K. (2017). Neural network-based modelling for forest biomass assessment. *Carbon Management*, *8*(4), 305–317. https://doi.org/10.1080/17583004.2017.1357402

Nandy, S., Srinet, R., & Padalia, H. (2021). Mapping Forest Height and Aboveground Biomass by Integrating ICESat-2, Sentinel-1 and Sentinel-2 Data Using Random Forest Algorithm in Northwest Himalayan Foothills of India. *Geophysical Research Letters*, *48*(14). https://doi.org/10.1029/2021GL093799

Neumann, M., Saatchi, S. S., Ulander, L. M. H., & Fransson, J. E. S. (2012). Assessing Performance of L- and P-Band Polarimetric Interferometric SAR Data in Estimating Boreal Forest Above-Ground Biomass. *IEEE Transactions on Geoscience and Remote Sensing*, *50*(3), 714–726. https://doi.org/10.1109/TGRS.2011.2176133

Nielsen, C. K., Jørgensen, U., & Lærke, P. E. (2021). Root-To-Shoot Ratios of Flood-Tolerant Perennial Grasses Depend on Harvest and Fertilization Management: Implications for Quantification of Soil Carbon Input. *Frontiers in Environmental Science*, *9*. https://doi.org/10.3389/fenvs.2021.785531

Ningthoujam, R., Balzter, H., Tansey, K., Morrison, K., Johnson, S., Gerard, F., George, C., Malhi, Y., Burbidge, G., Doody, S., Veck, N., Llewellyn, G., Blythe, T., Rodriguez-Veiga, P., Van Beijma, S., Spies, B., Barnes, C., Padilla-Parellada, M., Wheeler, J., … Bermejo, J. (2016). Airborne S-Band SAR for Forest Biophysical Retrieval in Temperate Mixed Forests of the UK. *Remote Sensing*, *8*(7), 609. https://doi.org/10.3390/rs8070609

Nord, M. E., Ainsworth, T. L., Jong-Sen Lee, & Stacy, N. J. S. (2009). Comparison of Compact Polarimetric Synthetic Aperture Radar Modes. *IEEE Transactions on Geoscience and Remote Sensing*, *47*(1), 174–188. https://doi.org/10.1109/TGRS.2008.2000925

Okada, Y., Nakamura, S., Iribe, K., Yokota, Y., Tsuji, M., Tsuchida, M., Hariu, K., Kankaku, Y., Suzuki, S., Osawa, Y., & Shimada, M. (2013). System design of wide swath, high resolution, full polarimietoric L-band SAR onboard ALOS-2. *2013 IEEE International Geoscience and Remote Sensing Symposium - IGARSS*, 2408–2411. https://doi.org/10.1109/IGARSS.2013.6723305

Olesk, A., Voormansik, K., Pohjala, M., & Noorma, M. (2015). Forest change detection from Sentinel-1 and ALOS-2 satellite images. *2015 IEEE 5th Asia-Pacific Conference on Synthetic Aperture Radar (APSAR)*, 522–527. https://doi.org/10.1109/APSAR.2015.7306263

Padalia, H., & Musthafa, M. (2017). Characterization and classification of freshwater marshy wetland using synthetic aperture radar polarimetry: a case study from Loktak wetland, Northeast India. *Journal of Applied Remote Sensing*, *11*(1), 016029. https://doi.org/10.1117/1.JRS.11.016029

Pan, Y., Birdsey, R. A., Fang, J., Houghton, R., Kauppi, P. E., Kurz, W. A., Phillips, O. L., Shvidenko, A., Lewis, S. L., Canadell, J. G., Ciais, P., Jackson, R. B., Pacala, S. W., McGuire, A. D., Piao, S., Rautiainen, A., Sitch, S., & Hayes, D. (2011). A Large and Persistent Carbon Sink in the World's Forests. *Science*, *333*(6045), 988–993. https://doi.org/10.1126/science.1201609

Pantze, A., Fransson, J. E. S., & Santoro, M. (2010). Forest change detection from L-band satellite SAR images using iterative histogram matching and thresholding together with data fusion. *2010 IEEE International Geoscience and Remote Sensing Symposium*, 1226–1229. https://doi.org/10.1109/IGARSS.2010.5650677

Patenaude, G., Milne, R., & Dawson, T. P. (2005). Synthesis of remote sensing approaches for forest carbon estimation: reporting to the Kyoto Protocol. *Environmental Science & Policy*, *8*(2), 161–178. https://doi.org/10.1016/j.envsci.2004.12.010

Peregon, A., & Yamagata, Y. (2013a). The use of ALOS/PALSAR backscatter to estimate above-ground forest biomass: A case study in Western Siberia. *Remote Sensing of Environment*, *137*, 139–146. https://doi.org/10.1016/j.rse.2013.06.012

Peregon, A., & Yamagata, Y. (2013b). The use of ALOS/PALSAR backscatter to estimate above-ground forest biomass: A case study in Western Siberia. *Remote Sensing of Environment*, *137*, 139–146. https://doi.org/10.1016/j.rse.2013.06.012

Persson, H., Wallerman, J., Olsson, H., & Fransson, J. E. S. (2013). Estimating forest biomass and height using optical stereo satellite data and a DTM from laser scanning data. *Canadian Journal of Remote Sensing*, *39*(3), 251–262. https://doi.org/10.5589/m13-032

Potapov, P., Li, X., Hernandez-Serna, A., Tyukavina, A., Hansen, M. C., Kommareddy, A., Pickens, A., Turubanova, S., Tang, H., Silva, C. E., Armston, J., Dubayah, R., Blair, J. B., & Hofton, M. (2021a). Mapping global forest canopy height through integration of GEDI and

Landsat data. *Remote Sensing of Environment*, *253*, 112165. https://doi.org/10.1016/j.rse.2020.112165

Potapov, P., Li, X., Hernandez-Serna, A., Tyukavina, A., Hansen, M. C., Kommareddy, A., Pickens, A., Turubanova, S., Tang, H., Silva, C. E., Armston, J., Dubayah, R., Blair, J. B., & Hofton, M. (2021b). Mapping global forest canopy height through integration of GEDI and Landsat data. *Remote Sensing of Environment*, *253*. https://doi.org/10.1016/j.rse.2020.112165

Potapov, P., Yaroshenko, A., Turubanova, S., Dubinin, M., Laestadius, L., Thies, C., Aksenov, D., Egorov, A., Yesipova, Y., Glushkov, I., Karpachevskiy, M., Kostikova, A., Manisha, A., Tsybikova, E., Zhuravleva, I., Potapov, P., Yaroshenko, A., Turubanova, S., Dubinin, M., … Zhuravleva, I. (2008). *Mapping the World's Intact Forest Landscapes by Remote Sensing*.

Potin, P., Rosich, B., Roeder, J., & Bargellini, P. (2014). Sentinel-1 Mission operations concept. *2014 IEEE Geoscience and Remote Sensing Symposium*, 1465–1468. https://doi.org/10.1109/IGARSS.2014.6946713

Pretzsch, H. (2009). *Forest Dynamics, Growth and Yield*. Springer Berlin Heidelberg. https://doi.org/10.1007/978-3-540-88307-4

Priyanka, Rajat, Avtar, R., Malik, R., Musthafa, M., Rathore, V. S., Kumar, P., & Singh, G. (2023). Forest plantation species classification using Full-Pol-Time-Averaged SAR scattering powers. *Remote Sensing Applications: Society and Environment*, *29*, 100924. https://doi.org/10.1016/j.rsase.2023.100924

Qi, W., Saarela, S., Armston, J., Ståhl, G., & Dubayah, R. (2019). Forest biomass estimation over three distinct forest types using TanDEM-X InSAR data and simulated GEDI lidar data. *Remote Sensing of Environment*, *232*, 111283. https://doi.org/10.1016/j.rse.2019.111283

Quegan, S., Le Toan, T., Chave, J., Dall, J., Exbrayat, J.-F., Minh, D. H. T., Lomas, M., D'Alessandro, M. M., Paillou, P., Papathanassiou, K., Rocca, F., Saatchi, S., Scipal, K., Shugart, H., Smallman, T. L., Soja, M. J., Tebaldini, S., Ulander, L., Villard, L., & Williams, M. (2019). The European Space Agency BIOMASS mission: Measuring forest above-ground biomass from space. *Remote Sensing of Environment*, *227*, 44–60. https://doi.org/10.1016/j.rse.2019.03.032

Rajashekar, G., Fararoda, R., Reddy, R. S., Jha, C. S., Ganeshaiah, K. N., Singh, J. S., & Dadhwal, V. K. (2018). Spatial distribution of forest biomass carbon (Above and below ground) in Indian forests. *Ecological Indicators*, *85*, 742–752. https://doi.org/10.1016/j.ecolind.2017.11.024

Rajat, Priyanka, Musthafa, M., Kumar, P., Alsulamy, S., Khedher, K., & Avtar, R. (2024). Development of L-band fully polarimetric SAR algorithm for forest biomass retrieval using 7SD and random forest regression. *Physics and Chemistry of the Earth, Parts A/B/C*, *136*, 103688. https://doi.org/10.1016/j.pce.2024.103688

Ranson, K. J., & Guoqing Sun. (1994). Mapping biomass of a northern forest using multifrequency SAR data. *IEEE Transactions on Geoscience and Remote Sensing*, *32*(2), 388–396. https://doi.org/10.1109/36.295053

Ranson, K. J., Saatchi, S., & Guoqing Sun. (1995). Boreal forest ecosystem characterization with SIR-C/XSAR. *IEEE Transactions on Geoscience and Remote Sensing*, *33*(4), 867–876. https://doi.org/10.1109/36.406673

Reiche, J., Hamunyela, E., Verbesselt, J., Hoekman, D., & Herold, M. (2018). Improving near-real time deforestation monitoring in tropical dry forests by combining dense Sentinel-1 time series with Landsat and ALOS-2 PALSAR-2. *Remote Sensing of Environment*, *204*, 147–161. https://doi.org/10.1016/j.rse.2017.10.034

Reiche, J., Mullissa, A., Slagter, B., Gou, Y., Tsendbazar, N.-E., Odongo-Braun, C., Vollrath, A., Weisse, M. J., Stolle, F., Pickens, A., Donchyts, G., Clinton, N., Gorelick, N., & Herold, M. (2021). Forest disturbance alerts for the Congo Basin using Sentinel-1. *Environmental Research Letters*, *16*(2), 024005. https://doi.org/10.1088/1748-9326/abd0a8

Reiche, J., Verbesselt, J., Hoekman, D., & Herold, M. (2015). Fusing Landsat and SAR time series to detect deforestation in the tropics. *Remote Sensing of Environment*, *156*, 276–293. https://doi.org/10.1016/j.rse.2014.10.001

Rignot, E., Echelmeyer, K., & Krabill, W. (2001). Penetration depth of interferometric synthetic-aperture radar signals in snow and ice. *Geophysical Research Letters*, *28*(18), 3501–3504. https://doi.org/10.1029/2000GL012484

Rignot, E., Salas, W. A., & Skole, D. L. (1997). Mapping deforestation and secondary growth in Rondonia, Brazil, using imaging radar and thematic mapper data. *Remote Sensing of Environment*, *59*(2), 167–179. https://doi.org/10.1016/S0034-4257(96)00150-2

Rodríguez-Veiga, P., Wheeler, J., Louis, V., Tansey, K., & Balzter, H. (2017a). Quantifying Forest Biomass Carbon Stocks From Space. In *Current Forestry Reports* (Vol. 3, Issue 1). Springer International Publishing. https://doi.org/10.1007/s40725-017-0052-5

Rodríguez-Veiga, P., Wheeler, J., Louis, V., Tansey, K., & Balzter, H. (2017b). Quantifying Forest Biomass Carbon Stocks From Space. *Current Forestry Reports*, *3*(1), 1–18. https://doi.org/10.1007/s40725-017-0052-5

Saatchi, S., Halligan, K., Despain, D. G., & Crabtree, R. L. (2007). Estimation of Forest Fuel Load From Radar Remote Sensing. *IEEE Transactions on Geoscience and Remote Sensing*, *45*(6), 1726–1740. https://doi.org/10.1109/TGRS.2006.887002

Saatchi, S., Marlier, M., Chazdon, R. L., Clark, D. B., & Russell, A. E. (2011). Impact of spatial variability of tropical forest structure on radar estimation of aboveground biomass. *Remote Sensing of Environment*, *115*(11), 2836–2849. https://doi.org/10.1016/j.rse.2010.07.015

Saatchi, S. S., Harris, N. L., Brown, S., Lefsky, M., Mitchard, E. T. A., Salas, W., Zutta, B. R., Buermann, W., Lewis, S. L., Hagen, S., Petrova, S., White, L., Silman, M., & Morel, A. (2011). Benchmark map of forest carbon stocks in tropical regions across three continents. *Proceedings of the National Academy of Sciences*, *108*(24), 9899–9904. https://doi.org/10.1073/pnas.1019576108

SAATCHI, S. S., HOUGHTON, R. A., DOS SANTOS ALVALÁ, R. C., SOARES, J. V., & YU, Y. (2007a). Distribution of aboveground live biomass in the Amazon basin. *Global Change Biology*, *13*(4), 816–837. https://doi.org/10.1111/j.1365-2486.2007.01323.x

SAATCHI, S. S., HOUGHTON, R. A., DOS SANTOS ALVALÁ, R. C., SOARES, J. V., & YU, Y. (2007b). Distribution of aboveground live biomass in the Amazon basin. *Global Change Biology*, *13*(4), 816–837. https://doi.org/10.1111/j.1365-2486.2007.01323.x

Sandberg, G., Ulander, L. M. H., Fransson, J. E. S., Holmgren, J., & Le Toan, T. (2011). L- and P-band backscatter intensity for biomass retrieval in hemiboreal forest. *Remote Sensing of Environment*, *115*(11), 2874–2886. https://doi.org/10.1016/j.rse.2010.03.018

Santi, E., Paloscia, S., Pettinato, S., Fontanelli, G., Mura, M., Zolli, C., Maselli, F., Chiesi, M., Bottai, L., & Chirici, G. (2017). The potential of multifrequency SAR images for estimating forest biomass in Mediterranean areas. *Remote Sensing of Environment*, *200*, 63–73. https://doi.org/10.1016/j.rse.2017.07.038

Santoro, M., Askne, J., Smith, G., & Fransson, J. E. S. (2002). Stem volume retrieval in boreal forests from ERS-1/2 interferometry. *Remote Sensing of Environment*, *81*(1), 19–35. https://doi.org/10.1016/S0034-4257(01)00329-7

Santoro, M., Cartus, O., & Fransson, J. E. S. (2021). Integration of allometric equations in the water cloud model towards an improved retrieval of forest stem volume with L-band SAR data in Sweden. *Remote Sensing of Environment*, *253*. https://doi.org/10.1016/j.rse.2020.112235

Santoro, M., Fransson, J. E. S., Eriksson, L. E. B., Magnusson, M., Ulander, L. M. H., & Olsson, H. (2009). Signatures of ALOS PALSAR L-Band Backscatter in Swedish Forest. *IEEE Transactions on Geoscience and Remote Sensing*, *47*(12), 4001–4019. https://doi.org/10.1109/TGRS.2009.2023906

Sassan Saatchi. (2019). *SAR Methods for Mapping and Monitoring Forest Biomass*.

Sato, A., Yamaguchi, Y., Singh, G., & Sang-Eun Park. (2012). Four-Component Scattering Power Decomposition With Extended Volume Scattering Model. *IEEE Geoscience and Remote Sensing Letters*, *9*(2), 166–170. https://doi.org/10.1109/LGRS.2011.2162935

Schlund, M., & Davidson, M. (2018). Aboveground Forest Biomass Estimation Combining L- and P-Band SAR Acquisitions. *Remote Sensing*, *10*(7), 1151. https://doi.org/10.3390/rs10071151

Schmullius, C. C., & Evans, D. L. (1997). Review article Synthetic aperture radar (SAR) frequency and polarization requirements for applications in ecology, geology, hydrology, and oceanography: A tabular status quo after SIR-C/X-SAR. *International Journal of Remote Sensing*, *18*(13), 2713–2722. https://doi.org/10.1080/014311697217297

Schneider, F. D., Ferraz, A., Hancock, S., Duncanson, L. I., Dubayah, R. O., Pavlick, R. P., & Schimel, D. S. (2020). Towards mapping the diversity of canopy structure from space with GEDI. *Environmental Research Letters*, *15*(11). https://doi.org/10.1088/1748-9326/ab9e99

Shimada, M. (2013). ALOS-2 science program. *2013 IEEE International Geoscience and Remote Sensing Symposium - IGARSS*, 2400–2403. https://doi.org/10.1109/IGARSS.2013.6723303

Shugart, H. H., Saatchi, S., & Hall, F. G. (2010). Importance of structure and its measurement in quantifying function of forest ecosystems. *Journal of Geophysical Research: Biogeosciences*, *115*(G2). https://doi.org/10.1029/2009JG000993

Sileshi, G. W. (2014). A critical review of forest biomass estimation models, common mistakes and corrective measures. In *Forest Ecology and Management* (Vol. 329, pp. 237–254). Elsevier. https://doi.org/10.1016/j.foreco.2014.06.026

Silva, C. A., Duncanson, L., Hancock, S., Neuenschwander, A., Thomas, N., Hofton, M., Fatoyinbo, L., Simard, M., Marshak, C. Z., Armston, J., Lutchke, S., & Dubayah, R. (2021). Fusing simulated GEDI, ICESat-2 and NISAR data for regional aboveground biomass mapping. *Remote Sensing of Environment*, *253*, 112234. https://doi.org/10.1016/j.rse.2020.112234

Sinclair, G. (1950). The transmission and reception of elliptically polarized waves. *Proceed- Ings of the IRE*, *38*, 148–151.

Singh, G., Malik, R., Mohanty, S., Rathore, V. S., Yamada, K., Umemura, M., & Yamaguchi, Y. (2019). Seven-Component Scattering Power Decomposition of POLSAR Coherency Matrix. *IEEE Transactions on Geoscience and Remote Sensing*, *57*(11), 8371–8382. https://doi.org/10.1109/TGRS.2019.2920762

Singh, G., & Yamaguchi, Y. (2018). Model-Based Six-Component Scattering Matrix Power Decomposition. *IEEE Transactions on Geoscience and Remote Sensing*, *56*(10), 5687–5704. https://doi.org/10.1109/TGRS.2018.2824322

Singh, G., Yamaguchi, Y., & Park, S. E. (2013a). General four-component scattering power decomposition with unitary transformation of coherency matrix. *IEEE Transactions on Geoscience and Remote Sensing*, *51*(5), 3014–3022. https://doi.org/10.1109/TGRS.2012.2212446

Singh, G., Yamaguchi, Y., & Park, S.-E. (2013b). General Four-Component Scattering Power Decomposition With Unitary Transformation of Coherency Matrix. *IEEE Transactions on Geoscience and Remote Sensing*, *51*(5), 3014–3022. https://doi.org/10.1109/TGRS.2012.2212446

Sinha, S., Jeganathan, C., Sharma, L. K., & Nathawat, M. S. (2015). A review of radar remote sensing for biomass estimation. *International Journal of Environmental Science and Technology*, *12*(5), 1779–1792. https://doi.org/10.1007/s13762-015-0750-0

Sinha, S., Santra, A., Sharma, L., Jeganathan, C., Nathawat, M. S., Das, A. K., & Mohan, S. (2018). Multi-polarized Radarsat-2 satellite sensor in assessing forest vigor from above ground biomass. *Journal of Forestry Research*, *29*(4), 1139–1145. https://doi.org/10.1007/s11676-017-0511-7

Sleight, N. J., Volk, T. A., & Eisenbies, M. (2023). Belowground Biomass and Root:Shoot Ratios of Three Willow Cultivars at Two Sites. *Forests*, *14*(3), 525. https://doi.org/10.3390/f14030525

Slik, J. W. F., Aiba, S., Brearley, F. Q., Cannon, C. H., Forshed, O., Kitayama, K., Nagamasu, H., Nilus, R., Payne, J., Paoli, G., Poulsen, A. D., Raes, N., Sheil, D., Sidiyasa, K., Suzuki, E., & van Valkenburg, J. L. C. H. (2010). Environmental correlates of tree biomass, basal area, wood specific gravity and stem density gradients in Borneo's tropical forests. *Global Ecology and Biogeography*, *19*(1), 50–60. https://doi.org/10.1111/j.1466-8238.2009.00489.x

Snoeij, P., Attema, E., Davidson, M., Levrini, G., Rommen, B., & Floury, N. (2009). *Sentinel-1 CSAR mission status* (R. Meynart, S. P. Neeck, & H. Shimoda, Eds.; p. 747403). https://doi.org/10.1117/12.829623

Soja, M. J., Sandberg, G., & Ulander, L. M. H. (2013). Regression-Based Retrieval of Boreal Forest Biomass in Sloping Terrain Using P-Band SAR Backscatter Intensity Data. *IEEE Transactions on Geoscience and Remote Sensing*, *51*(5), 2646–2665. https://doi.org/10.1109/TGRS.2012.2219538

Spawn, S. A., Sullivan, C. C., Lark, T. J., & Gibbs, H. K. (2020). Harmonized global maps of above and belowground biomass carbon density in the year 2010. *Scientific Data*, *7*(1), 112. https://doi.org/10.1038/s41597-020-0444-4

Suab, S. A., Supe, H., Louw, A. S., Avtar, R., Korom, A., & Xinyu, C. (2024). Mapping of Temporally Dynamic Tropical Forest and Plantations Canopy Height in Borneo Utilizing TanDEM-X InSAR and Multi-sensor Remote Sensing Data. *Journal of the Indian Society of Remote Sensing*. https://doi.org/10.1007/s12524-024-01820-6

Sugimoto, R., Kato, S., Nakamura, R., Tsutsumi, C., & Yamaguchi, Y. (2022). Deforestation detection using scattering power decomposition and optimal averaging of volume scattering power in tropical rainforest regions. *Remote Sensing of Environment*, *275*, 113018. https://doi.org/10.1016/j.rse.2022.113018

Sugimoto, R., Nakamura, R., Tsutsumi, C., & Yamaguchi, Y. (2021). Deforestation Detection in Tropical Forests using Scattering Power Decomposition. *2020 International Symposium on Antennas and Propagation (ISAP)*, 305–306. https://doi.org/10.23919/ISAP47053.2021.9391230

Sugimoto, R., Nakamura, R., Tsutsumi, C., & Yamaguchi, Y. (2023). Extension of Scattering Power Decomposition to Dual-Polarization Data for Tropical Forest Monitoring. *Remote Sensing*, *15*(3), 839. https://doi.org/10.3390/rs15030839

Sun, G., Ranson, K. J., & Kharuk, V. I. (2002). Radiometric slope correction for forest biomass estimation from SAR data in the Western Sayani Mountains, Siberia. *Remote Sensing of Environment*, *79*(2–3), 279–287. https://doi.org/10.1016/S0034-4257(01)00279-6

Suzuki, S., Kankaku, Y., & Osawa, Y. (2012). *ALOS-2 development status and draft acquisition strategy* (R. Meynart, S. P. Neeck, & H. Shimoda, Eds.; p. 85330A). https://doi.org/10.1117/12.973708

Tadono, T., Ohki, M., & Abe, T. (2019). SUMMARY OF NATURAL DISASTER RESPONSES BY THE ADVANCED LAND OBSERVING SATELLITE-2 (ALOS-2). *The International Archives of the Photogrammetry, Remote Sensing and Spatial Information Sciences*, *XLII-3/W7*, 69–72. https://doi.org/10.5194/isprs-archives-XLII-3-W7-69-2019

Thapa, R. B., Watanabe, M., Motohka, T., & Shimada, M. (2015). Potential of high-resolution ALOS-PALSAR mosaic texture for aboveground forest carbon tracking in tropical region. *Remote Sensing of Environment*, *160*, 122–133. https://doi.org/10.1016/j.rse.2015.01.007

Thiel, C., & Schmullius, C. (2016). The potential of ALOS PALSAR backscatter and InSAR coherence for forest growing stock volume estimation in Central Siberia. *Remote Sensing of Environment*, *173*, 258–273. https://doi.org/10.1016/j.rse.2015.10.030

Tomar, K. S., Kumar, S., & Tolpekin, V. A. (2019). Evaluation of Hybrid Polarimetric Decomposition Techniques for Forest Biomass Estimation. *IEEE Journal of Selected Topics in Applied Earth Observations and Remote Sensing*, *12*(10), 3712–3718. https://doi.org/10.1109/JSTARS.2019.2947088

Torres, R., Geudtner, D., Lokas, S., Bibby, D., Snoeij, P., Traver, I. N., Ceba Vega, F., Poupaert, J., & Osborne, S. (2018). Sentinel-1 Satellite Evolution. *IGARSS 2018 - 2018 IEEE International Geoscience and Remote Sensing Symposium*, 1555–1558. https://doi.org/10.1109/IGARSS.2018.8517899

Torre-Tojal, L., Bastarrika, A., Boyano, A., Lopez-Guede, J. M., & Graña, M. (2022). Above-ground biomass estimation from LiDAR data using random forest algorithms. *Journal of Computational Science*, *58*. https://doi.org/10.1016/j.jocs.2021.101517

Touzi, R. (2007). Target Scattering Decomposition in Terms of Roll-Invariant Target Parameters. *IEEE Transactions on Geoscience and Remote Sensing*, *45*(1), 73–84. https://doi.org/10.1109/TGRS.2006.886176

Touzi, R. (2016). Polarimetric target scattering decomposition: A review. *2016 IEEE International Geoscience and Remote Sensing Symposium (IGARSS)*, 5658–5661. https://doi.org/10.1109/IGARSS.2016.7730478

Treuhaft, R., Gonzalves, F., dos Santos, J. R., Keller, M., Palace, M., Madsen, S. N., Sullivan, F., & Graca, P. M. L. A. (2015). Tropical-Forest Biomass Estimation at X-Band From the Spaceborne TanDEM-X Interferometer. *IEEE Geoscience and Remote Sensing Letters*, *12*(2), 239–243. https://doi.org/10.1109/LGRS.2014.2334140

Treuhaft, R. N., Madsen, S. N., Moghaddam, M., & van Zyl, J. J. (1996). Vegetation characteristics and underlying topography from interferometric radar. *Radio Science*, *31*(6), 1449–1485. https://doi.org/10.1029/96RS01763

Trisasongko, B. H. (2010). The Use of Polarimetric SAR Data for Forest Disturbance Monitoring. *Sensing and Imaging: An International Journal*, *11*(1), 1–13. https://doi.org/10.1007/s11220-010-0048-8

Tsui, O. W., Coops, N. C., Wulder, M. A., & Marshall, P. L. (2013). Integrating airborne LiDAR and space-borne radar via multivariate kriging to estimate above-ground biomass. *Remote Sensing of Environment*, *139*, 340–352. https://doi.org/10.1016/j.rse.2013.08.012

Ulaby, F., & El-rayes, M. (1987). Microwave Dielectric Spectrum of Vegetation - Part II: Dual-Dispersion Model. *IEEE Transactions on Geoscience and Remote Sensing*, *GE-25*(5), 550–557. https://doi.org/10.1109/TGRS.1987.289833

UNFCCC. (2015). *Measurements for Estimation of Carbon Stocks in Aff orestation and Reforestation Project Activities under the Clean Development Mechanism A Field Manual*.

Valbuena, R., Hernando, A., Manzanera, J. A., Görgens, E. B., Almeida, D. R. A., Mauro, F., García-Abril, A., & Coomes, D. A. (2017). Enhancing of accuracy assessment for forest above-ground biomass estimates obtained from remote sensing via hypothesis testing and overfitting evaluation. *Ecological Modelling*, *366*, 15–26. https://doi.org/10.1016/j.ecolmodel.2017.10.009

Van Zyl, J. J., Arii, M., & Kim, Y. (2011). Model-based decomposition of polarimetric SAR covariance matrices constrained for nonnegative eigenvalues. *IEEE Transactions on*

Geoscience and Remote Sensing, *49*(9), 3452–3459. https://doi.org/10.1109/TGRS.2011.2128325

Varghese, A. O., Suryavanshi, A., & Joshi, A. K. (2016a). Analysis of different polarimetric target decomposition methods in forest density classification using C band SAR data. *International Journal of Remote Sensing*, *37*(3), 694–709. https://doi.org/10.1080/01431161.2015.1136448

Varghese, A. O., Suryavanshi, A., & Joshi, A. K. (2016b). Analysis of different polarimetric target decomposition methods in forest density classification using C band SAR data. *International Journal of Remote Sensing*, *37*(3), 694–709. https://doi.org/10.1080/01431161.2015.1136448

Verma, P., & Kumar Ghosh, P. (2022). REDD+ Strategy for forest carbon sequestration in India. *The Holistic Approach to Environment*, *12*(3), 117–130. https://doi.org/10.33765/thate.12.3.4

Wang, C., Elmore, A. J., Numata, I., Cochrane, M. A., Lei, S., Hakkenberg, C. R., Li, Y., Zhao, Y., & Tian, Y. (2022). A Framework for Improving Wall-to-Wall Canopy Height Mapping by Integrating GEDI LiDAR. *Remote Sensing*, *14*(15). https://doi.org/10.3390/rs14153618

Wang, H., Magagi, R., Goïta, K., Trudel, M., McNairn, H., & Powers, J. (2019). Crop phenology retrieval via polarimetric SAR decomposition and Random Forest algorithm. *Remote Sensing of Environment*, *231*. https://doi.org/10.1016/j.rse.2019.111234

Wang, Q., Ni-Meister, W., Ni, W., & Pang, Y. (2019). The Potential of Forest Biomass Inversion Based on Canopy-Independent Structure Metrics Tested by Airborne LiDAR Data. *IGARSS 2019 - 2019 IEEE International Geoscience and Remote Sensing Symposium*, 7354–7357. https://doi.org/10.1109/IGARSS.2019.8898393

Wang, X., Zhang, W., Ding, Q., Zheng, C., & Luo, J. (2019). Analysis of polarisation features of typical targets in Chengdu using GF-3 fully polarimetric synthetic aperture radar data. *The Journal of Engineering*, *2019*(20), 6923–6927. https://doi.org/10.1049/joe.2019.0548

Wang, Y., & Davis, F. W. (1997). Decomposition of polarimetric synthetic aperture radar backscatter from upland and flooded forests. *International Journal of Remote Sensing*, *18*(6), 1319–1332. https://doi.org/10.1080/014311697218449

Waqar, M. M., Sukmawati, R., Ji, Y., & Sri Sumantyo, J. T. (2020). Tropical peatland forest biomass estimation using polarimetric parameters extracted from RadarSAT-2 images. *Land*, *9*(6). https://doi.org/10.3390/LAND9060193

Waske, B., & Braun, M. (2009). Classifier ensembles for land cover mapping using multitemporal SAR imagery. *ISPRS Journal of Photogrammetry and Remote Sensing*, *64*(5), 450–457. https://doi.org/10.1016/j.isprsjprs.2009.01.003

Watanabe, M., Koyama, C. N., Hayashi, M., Nagatani, I., & Shimada, M. (2018). Early-Stage Deforestation Detection in the Tropics With *L* -band SAR. *IEEE Journal of Selected Topics in Applied Earth Observations and Remote Sensing*, *11*(6), 2127–2133. https://doi.org/10.1109/JSTARS.2018.2810857

Wei, N., Xia, J., Zhou, J., Jiang, L., Cui, E., Ping, J., & Luo, Y. (2022). Evolution of Uncertainty in Terrestrial Carbon Storage in Earth System Models from CMIP5 to CMIP6. *Journal of Climate*, *35*(17), 5483–5499. https://doi.org/10.1175/JCLI-D-21-0763.1

Wiederkehr, N. C., Gama, F. F., Castro, P. B. N., Bispo, P. da C., Balzter, H., Sano, E. E., Liesenberg, V., Santos, J. R., & Mura, J. C. (2020). Discriminating Forest Successional Stages, Forest Degradation, and Land Use in Central Amazon Using ALOS/PALSAR-2 Full-Polarimetric Data. *Remote Sensing*, *12*(21), 3512. https://doi.org/10.3390/rs12213512

Woodhouse, I. H. (2017). *Introduction to Microwave Remote Sensing*. CRC Press. https://doi.org/10.1201/9781315272573

Worku, A., & Ayalew, S. (2024). Review on drivers of deforestation and associated socio-economic and ecological impacts. *Vegetable Crops of Russia*, *3*, 112–119. https://doi.org/10.18619/2072-9146-2024-3-112-119

Wu, Z., Dye, D., Vogel, J., & Middleton, B. (2016). Estimating Forest and Woodland Aboveground Biomass Using Active and Passive Remote Sensing. *Photogrammetric Engineering & Remote Sensing*, *82*(4), 271–281. https://doi.org/10.14358/PERS.82.4.271

Wu, Z., Yao, F., Zhang, J., & Liu, H. (2024). Estimating Forest Aboveground Biomass Using a Combination of Geographical Random Forest and Empirical Bayesian Kriging Models. *Remote Sensing*, *16*(11), 1859. https://doi.org/10.3390/rs16111859

Wulder, M. A., White, J. C., Nelson, R. F., Næsset, E., Ørka, H. O., Coops, N. C., Hilker, T., Bater, C. W., & Gobakken, T. (2012). Lidar sampling for large-area forest characterization: A review. In *Remote Sensing of Environment* (Vol. 121, pp. 196–209). https://doi.org/10.1016/j.rse.2012.02.001

Xu, Y., Li, C., Sun, Z., Jiang, L., & Fang, J. (2019). Tree height explains stand volume of closed-canopy stands: Evidence from forest inventory data of China. *Forest Ecology and Management*, *438*, 51–56. https://doi.org/10.1016/j.foreco.2019.01.054

Yadav, S., Padalia, H., Sinha, S. K., Srinet, R., & Chauhan, P. (2021). Above-ground biomass estimation of Indian tropical forests using X band Pol-InSAR and Random Forest. *Remote Sensing Applications: Society and Environment*, *21*, 100462. https://doi.org/10.1016/j.rsase.2020.100462

Yadav, B. K. V., & Nandy, S. (2015). Mapping aboveground woody biomass using forest inventory, remote sensing and geostatistical techniques. *Environmental Monitoring and Assessment*, *187*(5), 308. https://doi.org/10.1007/s10661-015-4551-1

Yamaguchi, Y. (2020). *Polarimetric SAR Imaging*. CRC Press. https://doi.org/10.1201/9781003049753

Yamaguchi, Y., Moriyama, T., Ishido, M., & Yamada, H. (2005a). Four-component scattering model for polarimetric SAR image decomposition. *IEEE Transactions on Geoscience and Remote Sensing*, *43*(8), 1699–1706. https://doi.org/10.1109/TGRS.2005.852084

Yamaguchi, Y., Moriyama, T., Ishido, M., & Yamada, H. (2005b). Four-component scattering model for polarimetric SAR image decomposition. *IEEE Transactions on Geoscience and Remote Sensing*, *43*(8), 1699–1706. https://doi.org/10.1109/TGRS.2005.852084

Yamaguchi, Y., Sato, A., Boerner, W.-M., Sato, R., & Yamada, H. (2011). Four-Component Scattering Power Decomposition With Rotation of Coherency Matrix. *IEEE Transactions on Geoscience and Remote Sensing*, *49*(6), 2251–2258. https://doi.org/10.1109/TGRS.2010.2099124

Yamaguchi, Y., Yajima, Y., & Yamada, H. (2006). A four-component decomposition of POLSAR images based on the coherency matrix. *IEEE Geoscience and Remote Sensing Letters*, *3*(3), 292–296. https://doi.org/10.1109/LGRS.2006.869986

Yang, L., Meng, X., & Zhang, X. (2011). SRTM DEM and its application advances. In *International Journal of Remote Sensing* (Vol. 32, Issue 14, pp. 3875–3896). Taylor and Francis Ltd. https://doi.org/10.1080/01431161003786016

Yang, R., Dai, B., Tan, L., Liu, X., Yang, Z., & Li, H. (2021). Polarimetric Synthetic Aperture Radar. In *Polarimetric Microwave Imaging* (pp. 75–122). Springer Singapore. https://doi.org/10.1007/978-981-15-8897-6_3

Yu, Y., & Saatchi, S. (2016). Sensitivity of L-Band SAR Backscatter to Aboveground Biomass of Global Forests. *Remote Sensing*, *8*(6), 522. https://doi.org/10.3390/rs8060522

Zhang, H., Wang, C., Zhu, J., Fu, H., Han, W., & Xie, H. (2023). Forest Aboveground Biomass Estimation in Subtropical Mountain Areas Based on Improved Water Cloud Model and PolSAR Decomposition Using L-Band PolSAR Data. *Forests*, *14*(12), 2303. https://doi.org/10.3390/f14122303

Zhang, X., Dierking, W., Zhang, J., & Meng, J. (2015). A polarimetric decomposition method for ice in the bohai sea using C-band PolSAR data. *IEEE Journal of Selected Topics in Applied Earth Observations and Remote Sensing*, *8*(1), 47–66. https://doi.org/10.1109/JSTARS.2014.2356552

Zhang, X., & Ni-meister, W. (2014). *Remote Sensing of Forest Biomass* (pp. 63–98). https://doi.org/10.1007/978-3-642-25047-7_3